UNIVERSITÀ DEGLI STUDI DI TRIESTE

XXIX CICLO DEL DOTTORATO DI RICERCA IN

Biomedicina Molecolare

BIOMEDICAL GELS: STRUCTURE AND PROPERTIES

BIO/12_ING-IND/24

DOTTORANDA

MICHELA ABRAMI

COORDINATORE

PROF. GERMANA MERONI

SUPERVISORE DI TESI

PROF. GABRIELE GRASSI

CO-SUPERVISORE DI TESI

PROF. MARIO GRASSI

ANNO ACCADEMICO 2015/2016

"Do not agree with me in particular opinions but investigate the matter in the right way. To notice the interesting things...that serve as key if you use them properly"

Ludwig Wittgenstein

Table of Contents

Acknowledgements

First of all, I have to thanks my advisors Prof. Mario and Gabriele Grassi, for the continuous support of my Ph.D study and related research, for their patience, motivation, and knowledge. With special gratitude, I thank Prof. Romano Lapasin for his inexhaustible attitude to shear precious suggests, researchs and projects.

Indispensable for the high quality of this research, were the collaborations with Dr. Paolo Marizza, Prof. Domenico Larobina, Prof. Ferdinand Brandl and his PhD Susanne Kirchhof.

All the efforts to support these long three years were guaranteed from the costant and encouraging presence of Piero and my "biotech-world": Elisa, Anna, Vanessa, Ale and Zanna. A special thought is for my mother and her teaching: follow always your sensations and believe in the own *interior* voice.

Lastly, Davide, who has brought a new shining light in the third PhD year shaking up my reality for a new beginning…

Abstract

Biomedical hydrogels are defined as biocompatible solid-liquid systems in which polymeric chains (fibres) are crosslinked to form a 3D-network swollen by a huge water amount. Their use as controlled drug release systems is in continuous growth. However, a critical step in their development is the characterization of their 3D nano/micro structure and the correlation with fabrication parameters. Indeed, hydrogels structure is complex and depends on fibres diameter, concentration, mesh/pore size and degree of crosslinking. Historically, hydrogel structure has been studied using AFM, SEM, TEM and X-ray microscopy. Although these methods provide high-resolution images, they require a significant sample manipulation that can lead to shrinkage and collapse of the fibres structure. Moreover, as the analysis is restricted to very small sample portions, many pictures are necessary to have a statistically reliable evaluation of topological bulk properties. The target of this thesis is to propose the combined use of no-destructive, economic and fast technology such as rheology and low field NMR (LF-NMR) to understand the macro-, micro- and nanoscopic structural characteristic of hydrogels intended for biomedical application, and biological tissues. We aim to a) reduce the need of time-consuming and expensive measurements b) provide theoretical tools for a reliable and easy interpretation of experimental outcomes.

For what concerns hydrogels, the rheological and the LF NMR approaches were applied to:

- follow hydrogel gelation process in i) a thermo-sensitive chitosan gel ii) a sonicated nanocellulose solution. In particular, the effect of temperature on the gelation process, salt addition and sonication time were considered.
- correlate mesh size and release rate in Diels-Alder poly(ethylene glycol) based hydrogels for the controlled release of antibodies. Our estimations were in agreement with the results coming from in vitro release test about fluorescein isothiocyanate labeled Dextran and Bertuzimab.

- interpret the characteristics of cross-linked gels system relaying on polymer blends [PVP (poly-vinyl-pirrolidone) and alginate]. In particular gels mechanical strength, 3D nano/micro structure and mesh size distribution were determined. Some of these systems, suitable for liposomes delivery, were also characterized by TEM confirming our findings.

For what concerns biological tissues, the focus is on two innovative applications of LF-NMR relying on the different conditions experienced by water confined in three-dimensional structures. Indeed, from the LF-NMR point of view, we can distinguish between free water that is not affected by the solid surface, and bound water that undergoes the effect of solid surface:

- The first application considers the analysis on the expectorate of patients affected by cystic fibrosis (CF). This pulmonary disease is mainly characterized by a dehydrated mucus in airways and CF sputum differs from healthy saliva due to a bigger amount of mucin, DNA, protein and bacterial alginate. We analysed these voluntary samples to reveal mucus dehydration and pathological components, which are strictly correlated to disease severity. As this approach is less expensive, faster, non-invasive and does not require highly qualified personnel, it has the potential to become a valuable monitoring tool.
- The second application regards the evaluation of trabecular bone extracts from osteoporosis and osteoarthrosis patients who underwent hip replacement. These two pathological conditions differ for the quality of bone tissue, and both of them are typical of elders. Osteoarthrosis is a common disorder of synovial joints, whereas osteoporosis is a condition that weakens bones, making them fragile and more likely to break. Water mobility inside the trabecular network is connected to the pore size distribution characterising the bone tissue. Therefore we expected that osteoporosis samples present higher water mobility than osteoarthrosis ones. It could be a new method to rapidly and easily know the severity of osteoporosis. A comparison of our results with micro-CT analysis was undertaken.

1 Introduction to hydrogel

1.1 Hydrogel as biomaterial

Biomaterials are defined as any non-vital materials used in medical devices, intended to interact with biological systems (Widowati, 2016). They are chemical formations that have been designed for contact with blood, as replacements for soft and hard tissues, as adhesive, and as dental material (Peppas 1994, Langer 2000). An important property that differentiates a biomaterial from other materials is its biocompatibility. It is a term that is referred to as the appropriate host response to biomaterials. Traditional materials for biological application were constituted by ceramics, polymer composites and metals (Wendt., 1991) and they showed many drawbacks connected to a variety of reasons such as tissue rejection, cellular toxicity, inflammatory reaction and so on.

Over the years, research has, with huge efforts, pursued optimization of material properties and directed therapies, leading to rise of three dimensional structures of hydrophilic polymers, commonly known as hydrogel (Das et al., 2012). Hydrogels are water-swollen polymeric materials that maintain a distinct three-dimensional structure. These hydrophilic or amphiphilic polymer networks are basically formed by chemical or physical crosslinking which are capable to retain a large amount of water, or biological fluid, yet preventing dissolution of polymer chains in aqueous media (Kopčeg 2007) due to the presence of crosslinks. When swelled, they are soft and rubbery (this mechanical behaviour is called viscoelasticity) and resemble the living tissue and exhibit excellent biocompatibility (Das 2013). Indeed recently, Mazza and Ehert (Mazza and Ehreta, 2015) have shown that an appropriate capability of implants to deform at the right level, similarly to the macroscopic mechanical response of the surrounding biological materials, is essential in order to exclude short and long term health impairment. Due to the balance between elastic (due to the 3D structure) and viscous properties (due to crosslinks compliance), hydrogels can guarantee a

sufficient resistance in order to carry the loads they are exposed to without failure (rupture behaviour), and a level of compliance required to adapt to the adjacent biological tissues (deformation behaviour) (Mazza and Ehreta, 2015). Moreover, many hydrogels, due to a low interfacial free energy, provide inert surfaces that prevent nonspecific adsorption of proteins, a property known as antifouling (Ulijn, et al., 2007). All these properties are fundamental to avoid activation of a cascade of processes related to the corresponding biological response: cell damage, chronic inflammation, tissue destruction, fibrosis or necrosis (Duscher and Maan, 2014).

Hydrogels were the first biomaterials designed for use in the human body: DuPont scientists in 1936 synthesized the first synthetic hydrogel named poly (2-hydroxyethyl methacrylate) commonly known as PHEMA (Nemours, 1936). In the year 1960, Wichterle and Lim (Wichterle and Lim, 1960) established the importance of PHEMA hydrogel as an excellent candidate for contact lenses applications. This invention led to the contact lenses industry and to the modern field known as biomedical hydrogels. From this earlier clinically application as soft contact lenses, an immense number of hydrogels, tailored to biomedical gel, have been developed for a wide range of biomedical and pharmaceutical applications (Vermondem et al., 2012). All that has been feasible thanks to their, just cited, fantastic properties like high water content and soft nature, that render hydrogels similar to biological tissues and consequently minimize cell adherence and inflammation once implanted or injected in the body. Furthermore, their water absorbing capacity facilitates the accommodation of cells or hydrophilic molecules such as proteins and peptides within the polymeric network (Puppi et al., 2016).

Besides biocompatibility, biomaterials need to be biodegradables so that, after serving, it degrades into soluble and biocompatible products that can be eliminated (Das et al., 2012). Hydrogels have a wide range of biomedical applications including therapeutic compound delivery (Zang et al., 2016), wound dressing materials (Choi et al., 2016), 3D scaffold platforms for tissue engineering (Fiorentino et al., 2017), biosensors (Peppas and Van Blarcom, 2016), carriers for cell encapsulation (Mao at al., 2016), gene delivery devices and adhesives or barriers between tissue and material surface (Abrami et al., 2014).

1.2 Hydrogels classification

Hydrogel properties strongly depend on the macromolecular structure, methods of preparation and degree of crosslinking (Thiele et al., 2014). Based on their origin, there are two kinds of biodegradable polymers which have been used for preparation of hydrogels: natural polymers and synthetic polymers.

Natural hydrogel

Nature made extensive use of structured and homogeneous soft solids. Mucus, vitreous humor, cartilage, tendons and blood clots are all forms of a material known as hydrogel and playing vital roles. Hydrogels typically may contain 50 to 90 percent of water depending on preparation and degree of crosslinking. Biological hydrogel formation based on natural macromolecules like polypeptides, proteins, nucleic acid or polysaccharides are highly significant. Considerable efforts have been made to materialize the behavioural features of these natural polymer based hydrogels.

As already noted, viscoelasticity and permeability are the two very vital features of hydrogels present in human body. Viscoelasticity is the behaviour that results from being halfway between rubber and water. Crosslinked polymer architecture guarantees an elastic response to rapid deformations, and so, the maintenance of hydrogel shape over long periods. Very widely applied natural polymers are:

- polysaccharides, which include, among others, chitosan (Fan et al., 2017) alginate (Najafi-Soulari et al., 2016), hyaluronic acid (Ondeck and Engler, 2016), gellan (Bacelar et al., 2016) and guar gums (Coviello et al., 2013);
- proteins like gelatin (Kikuchi et al., 2008), heparin (Xiaochu et al., 2016), chondroitin sulfate (Hou et al., 2015).

These biopolymers allow to design hydrogel with many tailored properties, such as biological signalling and cell adhesion and, in this case, hydrogel can be degraded by cells and be remodelled. Hydrogel degradation occurs via digestion by enzymes (i.e the members of the matrix metalloproteinases) and hydrolysis which is in part regulated by physical factors such as the crosslink density (Yague at al., 2015).

Synthetic hydrogel

Natural hydrogels have been gradually replaced by synthetic types due to their higher water absorption capacity, long service life and wide varieties of raw chemical resources (Rajswary et al., 2016). Synthetically derived hydrogels may be grouped in two broad classes, chemically or physically crosslinked hydrogel.

- Chemically-crosslinked hydrogels are three dimensional polymer networks that show covalent bonds among polymeric chains. These hydrogels could also be formed directly from hydrophobic monomers, like vinyl pyrrolidone, methacrylic acid and poly-2-hydroxyethyl methacrylate (Tranoudis and Efron, 2004). Additionally, hydrogels could also be engineered by the crosslinking of hydrophilic polymer chains. Among the methods of crosslinking, radiation or hydrolysis of hydrophobic network is very popular (Ajji et al., 2005). Although extensive research is going on to provide a safe biomaterial, chemically-crosslinked systems show drawbacks such as a) the considerable heat generating upon crosslinking (exothermic reaction), b) the presence of un-reacted compounds that can be reactive and potentially toxic, and c) the formation of products that may have undesirable safety profiles.
- Hydrogels formed from physical interaction present a broad class of materials. These physical bonds could be formed by crystalline junctions, hydrogen bonding, phase-separation or other associations. Hydrogel rheological properties depend on the strength of these physical bonds and on their density.

Alternative hydrogel classification

Hydrogels can be also classified as neutral or ionic, based on the nature of polymeric chains side groups. In neutral hydrogels, the driving force for swelling is due to the water-polymer thermodynamic mixing contribution to the overall free energy, along with elastic polymer contribution. The swelling of ionic hydrogels is also affected by the ionic interactions between charged polymers and free ions (Gangji and Farahanji, 2009). Hydrogels containing ionic groups, such as carboxylic acid, imbibe larger amount of water, because of the increased hydrophilicity.

Furthermore, hydrogels can be also classified as homopolymers or copolymers, depending on the nature of the polymeric chains constituting the three-dimensional network. Another possible classification can relay on the physical structure of the network as amorphous, semicrystalline, hydrogen bonded structures, supermolecular structures and hydrocolloidal aggregates can exist (Rajswari et al., 2016). Recently, an even more interesting class of hydrogels, the stimuli responsive gels, has clearly emerged (Qui and Park, 2001). These gels show a swelling/de-swelling behaviour depending on the characteristics of the physical environment. Indeed, they can swell/de-swell in response to changes in pH, temperature, ionic strength, and electromagnetic radiation (Hoffmann, 2012). It is easy to imagine the huge potential application if this kind of biomaterial, such as separation membranes, biosensors, artificial muscles, and drug delivery devices (Xu et al., 2017)

1.3 Hydrogels for drug delivery

Typically, drugs are administered into the body via an oral or intravenous route and the drug therapeutic concentration is achieved by repeated administrations. The problem connected with such strategy consists in the fact that drug concentration in the body peaks and declines rapidly, particularly when the elimination rate of drug is very high (Nair and Laurencin, 2005). Indeed, free drugs, when introduced into bloodstream, are subjected to various metabolic processes, primarily renal/liver clearance and distribution in non-target tissues. These processes not only reduce the drug concentration at the active target site, but they also increase the likelihood of unwanted side effects (Matrigoti and Lahann, 2012). This is particularly of great concern, when using very active biotechnological drugs with narrow therapeutic windows. Finally, this approach shows low compliance by the patient.

Controlled drug delivery technology has developed into an attractive modality to solve many of the problems of traditional drug administration by regulating the rate as well as the spatial localization of therapeutic agents (Leong, 1987). In controlled drug delivery, usually, the active agent is entrapped in an insoluble

matrix from which it will be released in a controlled fashion. Furthermore, the release characteristics of the active agents can be effectively controlled by suitably engineering the matrix parameters (Nair and Laurencin, 2005). Hence, the field of drug delivery focuses on the development of technologies to deliver biomolecules to the site of the disease so as to maximize therapeutic benefits, minimize side effects and enhance patient compliance. For these reasons drug delivery systems (DDS) are of paramount importance to enhance the treatment efficacy of medications. Advanced DDS improve efficacy of different therapeutics in a dosage, spatial, and/or temporal controlled manner (Zangh, Yu et al., 2016). At the light of these requirements, an appropriate tool to control drug navigation through complex pathways before arriving at the target site could really be hydrogels.

In recent years, controlled DDS based on hydrogels have been highlighted as therapeutic carriers to deliver drug at target sites within a specific time frame (Sing and Lee, 2015). Indeed hydrogels, beyond their good biocompatibility, high water content, soft matter nature and flexibility in fabrication, present a polymeric network that works as a porous structure. This makes hydrogels extremely suitable to accommodate high-loads of water-soluble compounds. The success of hydrogels as DDS originates also from their preparation procedure that are beneficial in preserving drug stability, as very mild conditions (aqueous environment, room temperature) are normally adopted. On the contrary, other delivery systems (micro-particles, emulsions, etc..) need a preparation sometimes characterised by detrimental conditions for the hosted therapeutic agents (use of organic solvents, homogenization, shear force, temperature, and so on). Finally, hydrogels network limits drug mobility or immobilizes it in order to preserve/protect its structure. All these unique properties of hydrogel raised interest in their use as reservoir systems for therapeutic agent that are slowly released from polymeric matrix in a controlled fashion to maintain therapeutic effective concentration of the drug in the surrounding tissues or in circulation over an extended period of time (Vermonden et al., 2012). Furthermore, hydrogels can be made biodegradable by a proper selection of their building block as well as the applied cross-linking strategy (Hennink and van Nostrum, 2002). An appropriate design can ensure biodegradability and bio-resorption, that means a conversion of

material into water-soluble intermediates or end-products that can be eliminated from the body without harmful effects. In general, the elimination process can be performed via dissociation of polymer chains or by enzymatic and/or hydrolytic degradation pathways (Lenz, 1993)

1.4 Hydrogel structure characterization

As seen in the previous paragraph, increasing application of hydrogels in biological sensing has driven research to system with always more specific structural features (Ma et al., 2016). This scenario has led, simultaneously, to arouse a great interest around experimentally and theoretically studies on hydrogel properties. In order to understand and predict hydrogels characteristics, and so their suitability as a focused tools, knowledge about polymeric fibres organization is fundamental. Fibres structure often represents a complex network and usually it is quantitatively defined in terms of parameter such as mean fibre diameter, fibre density, pore size, degree of crosslinking and orientation. (Antoine et al., 2014). Among these parameters, one of the most important is represented by the mesh size distribution of polymeric network. Indeed, this characteristic heavily rules the mass exchange processes between the hydrogel and the surrounding (Grassi, et al. 2009). However, this parameter is not easily determinable and, often, only a raw estimation is available.

The main problem in hydrogels structure investigation stays in their nature: the high water content of hydrogel matrices is responsible for their desirable structural and physical properties, but it represents one of the most challenging barriers to structural characterisation (Aston et al., 2016). Ideally, the native structural arrangement of macromolecules and the distribution of other species in the aqueous system must be preserved. It is difficult to image that these hydrated materials retain their structural integrity once undergone to instrumental techniques where vacuum operating condition is applied (X-ray and electron microscopy, mercury intrusion porosimetry MIP) or samples are flash frozen in

liquid nitrogen (nitrogen adsorption NA). Despite this, these kinds of imaging tools continue to be widely diffuse in literature.

1.4.1 Typical characterization techniques.

Several methodologies devoted to the measurement of hydrogel fibres structure are available.

Historically, hydrogel fibres have been imaged using scanning electron microscopy (SEM) (Wang et al., 2016) and transmission electron microscopy (TEM) (Gulsonby et al., 2016) for qualitative/semi-quantitative analysis of polymeric chain structures. Image analysis has been used to obtain information about pore size distribution, porosity and surface area density (Ferreira et al., 2006). Although these methods provide high-resolution images and preserve relative information about fibres dimensions, they require significant sample manipulation, drying, and chemical processing. These can lead to shrinkage and collapse of the fibres structure, which prevent quantitative analysis of 3D fibres structure and SEM images (Antoine et al., 2014). Enviromental SEM allows to avoid vacuum and drying connected problems, but resolution is lower (Bogner et al., 2005). Nowadays SEM is still very often described in the literature to study morphological details of hydrogel, but such information is restricted to the location where the analysis is performed.

Another very diffusive technique is Atomic Forced microscopy (AFM), which often is dedicated for surface mechanical characterization, but it can be devoted for surface imaging. However, it is poorly suited for measurement of bulk properties due to the frequent heterogeneity of hydrogels. Furthermore, AFM measurements are too localized for an accurate estimation of total network properties (Oyen, 2014).

More advanced electron microscopy techniques, such as cryo-SEM (Aston et al., 2006), have been developed, which do not require sample dehydration, but necessitate of a delicate process of cooling rate that can easily alter internal structure of the hydrogel.

Electron microscopy remains in use for high resolution imaging of hydrogel topology where quantitative results are not necessary, but its limitations have led to the development of optical imaging techniques for fibres structure measurement of fully hydrated, unmodified hydrogels. These include two closely related techniques, two-photon fluorescence (TPF) and second-harmonic generation (SHG), and confocal fluorescence microscopy, all of which have become popular modalities for recording fibres structure as they can be used to obtain images of gels in the hydrated state (Antoine et al, 2014). TPF and SHG are both based on two-photon laser excitation and therefore have the advantages associated with near-infrared illumination that is, high penetration depth and low photo-toxicity. Further, the use of fluorescence or second-harmonic generation provides good signal-to-noise ratio due to suppression of background light. However, they require high laser power, a very expensive light source and have difficulty penetrating dense tissue (Raub et al., 2007). For these reasons, confocal microscope, although somewhat noisier than TPF or SHG, is more commonly used, most likely because of availability of necessary equipment (Tao et al., 2017). For all three optical modalities, the distance of the focal plane into the hydrogel is a critical parameter. Hydrogel fibres organization present an intrinsic heterogeneity and forms a significantly different network at the surface of the coverslip than within the gel. Therefore, images acquired too close to the coverslip produce misleading information.

As before explained, each technique offers advantages and disadvantages associated with sample preparation and resolution. To avoid artefacts and reduce the need for time-consuming, expensive measurements, a reliable solution could be the conjunction of these images with other techniques. Accordingly, the aim of this work is to consider other approaches such rheology (Halib et al., 2014), release tests (Hernandez et al., 2016), swelling equilibrium test (Pescosolido et al., 2012) and nuclear magnetic resonance spectroscopy (Abrami et al., 2014) to elucidate the topological architecture of hydrogels

Reference

Abrami M., D'Agostino I., Milcovich G., Fiorentino S., Farra R., Asaro F., Lapasin R., Grassi G., Grassi M. "Physical characterization of alginate–Pluronic F127 gel for endoluminal NABDs delivery" *Soft Matter* 2014 (10):729–37

Ajjia Z., Othmana I., Rosiakb J.M. "Production of hydrogel wound dressings using gamma radiation" *Nucl. Instrum. Methods Phys. Res. B* 2005 (229): 375-80

Antoine E.E., Vlachos P.P., Rylander M.N., "Review of collagen I hydrogels for bioengineered tissue microenvironments: characterization of mechanics, structure, and transport" *Tissue Eng. Part B.* 2014 (20) doi: 10.1089/ten.teb.2014.0086

Aston R., Sewell K., Klein T., Lawrie G., Grøndahl L. ''Evaluation of the impact of freezing preparation techniques on the characterisation of alginate hydrogels by cryo-SEM" *Eu. Polym. J.*2016 (82):1-15

Bacelar A.H., Silva-Correia J., Oliveira J.M., Reisab L.R. "Recent progress in gellan gum hydrogels provided by functionalization strategies" *J. Mat. Chem*. B. 2016 (4):6164-74

Bogner A., Thollet G., Basset B., Jouneau P.H., Gauthier C. "Wet STEM: A new development in environmental SEM for imaging nano-objects included in a liquid phase" *Ultramicroscopy* 2005 (104):290-301

Choi S.K., Park J.K., Kim J.H., Lee K.M., Kim E., Jeong K.S., Jeon W.B. "Integrin-binding elastin-like polypeptide as an in situ gelling delivery matrix enhances the therapeutic efficacy of adipose stem cells in healing full-thickness cutaneous wounds"*J Control Release.* 2016 (237):89-100

Coviello T., Margheritelli S., Matricardi P., Di Meo C., Cerreto F., Alhaique F., Abrami M., Grassi M. "Influence of borate amount on the swelling and rheological properties of the Scleroglucan/borax system" J. App. Plym. Sci 2015: doi 10.1002/app.42860

Das N., Bera T., Mukherjee A. "Biomaterial hydrogels for different biomedical applications". *Int J Pharm Bio Sci*., 2012 (3): 586-95

Das N. "A review on nature and preparation of hydrogel based on starting material" *I. J. Pharm. Pharm. Sci*. 2013 (5): 55-8

Dusher D, Maan Z.N. "Mechanotransduction and fibrosis" *J. Biomech.,* 2014 (47):1997-2005

Fan M., Ma Y., Tan H., Jia Y., Zou S., Guo S., Zhao M., Huang H., Ling Z., Chen Y., Hu X. "Covalent and injectable chitosan-chondroitin sulfate hydrogels embedded with chitosan microspheres for drug delivery and tissue engineering" *Mat. Sci. Eng. C*. 2017 (71): 67-74

Fernandez-Yague M.A., Abbah S.A., McNamara L., Zeugolis D.I., Pandit A., Biggs M.J. "Biomimetic approaches in bone tissue engineering: Integrating biological and physicomechanical strategies" *Adv Drug Deliv Rev*. 2015 (84):1-29

Ferreira L., Figueiredo M.M., Gil M.H., Ramos M.A. "Structural analysis of dextran-based hydrogels obtained chemoenzymatically" *J. Biomed. Mater. Res. B Appl. Biomater*. 2006 (77):55-64

Fiorentino S.M., Carfì Pavia F., La Carrubba V., Brucato V., Abrami M., Farra R., Turco G., Grassi G., Grassi M. "Characterization of PLLA Scaffolds for biomedical applications" *Int. J. Polym. Mat.* 2017(in press)

Ganji F. Vasheghani-Farahani E."Hydrogels in controlled drug delivery systems" *Iran. Polym. J.* 2009 (18):63-88

Grassi M, Farra R, Fiorentino S.M., Grassi G., Dapas B. "Hydrogel mesh size evaluation" chapter in *Polysaccharide hydrogels: characterization and biomedical application*s 2009 by Pan Stanford Publishing

Gulsonbi M., Parthasarathy S., Bharat Raj K., Jaisankar V. "Green synthesis, characterization and drug delivery applications of a novel silver/carboxymethylcellulose - poly(acrylamide) hydrogel nanocomposite" *Ecotoxicol. Environ. Saf.* 2016 (134):421-26

Halib N., Mohd Amin M.C,I, Ahmad I, Abrami M, Fiorentino S., Farra R., Grassi G., Musiani F. "Topological characterization of a bacterial cellulose–acrylic acid polymeric matrix" *Eu. J. Pharm. Sci*. 2014 (62):326–33

Hennink W.E., van Nostrum C.F. "Novel crosslinking methods to design hydrogels" *Adv. Drug Deliv. Rev.* 2002 (54):13–36

Hernandez C., Gawlik N., Goss M., Zhou H., Jeganathan S., Gilbert D., Exnera A.A. "Macroporous acrylamide phantoms improve prediction of in vivo performance of in situ forming implants" *J. Cont. Rel.* 2016 (243):225-31

Hoffmann A.S. “Stimuli-responsive polymers: Biomedical applications and challenges for clinical translation” *Adv. Drug Deliv. Rev*. 2013 (65):10-16

Hou R., Nie L., Du G., Xiong X., Fu J. “Natural polysaccharides promote chondrocyte adhesion and proliferation on magnetic nanoparticle/PVA composite hydrogels” *Colloids Surf. B Biointerfaces*. 2015 (132):146-54

Kikuchi T., Kubota S., Asaumi K., Kawaki H., Nishida T., Kawata K., Mitani S., Tabata Y., Ozaki T., Takigawa M. “Promotion of bone regeneration by CCN2 incorporated into gelatin hydrogel” *Tissue Eng. Part A*. 2008 (6):1089-98

Kopeček J. “Hydrogel biomaterials: A smart future?” *Biomaterials,* 2007 (28): 5185–92

Langer R. “Biomaterials: Status, challenges, and perspectives”. *A. I. Ch. E. Journal,* 2000 (46): 1286-9

Leong K.W., Langer R. “Polymeric controlled drug delivery” *Adv. Drug Deliv. Rev.* 1987 (1):199-233

Lenz, R. “Biodegradable polymers”. In R. Langer & N. Peppas (Eds.). *Biopolymers I* 1993 (107):1–40

Ma S., Yua B., Peia X., Zhoua F. “Structural hydrogels” *Polymer* 2016 (98): 516–35

Mao A.S., Shin J.W., Utech S., Wang H., Uzun O., Li W., Cooper M., Hu Y, Zhang L., Weitz D.A., Mooney D.A. “Deterministic encapsulation of single cells in thin tunable microgels for niche modelling and therapeutic delivery” *Nature Mat.* 2016 doi: 10.1038/NMAT4781

Mazza E., Ehreta A.E. “Mechanical biocompatibility of highly deformable biomedical materials” *J. Mech. Behav. Biomed. Mater*., 2015 (48):100–4

Mitragotri S., Lahann J. “Materials for Drug Delivery: Innovative Solutions to Address Complex Biological Hurdles” *Adv. Mater*. 2012 (24):3717–23

Nair. L.S., Laurencin C.T. “Polymers as Biomaterials for tissue engineering and controlled drug delivery” *Adv Biochem Engin/Biotechnol* 2006 (102): 47–90

Najafi-Soulari S., Shekarchizadeh H., Kadivar M. “Encapsulation optimization of lemon balm antioxidants in calcium alginate hydrogels” *J. Biomater. Sci. Polym.* 2016 (16):1631-44

Narendra K. S., Lee D. S., “In situ gelling pH- and temperature-sensitive biodegradable block copolymer hydrogels for drug delivery” *J. Control. Release* 2014 (193):214-27

Ondeck M.G., Engler A.J. “Mechanical Characterization of a Dynamic and Tunable Methacrylated Hyaluronic Acid Hydrogel” *J. Biomech. Eng*. 2016 (138):021003

Oyen L. “Mechanical characterisation of hydrogel materials” *Int. Mat. Rev.* 2014(59):44-59

Peppas N.A, Van Blarcom D.S. “Hydrogel-based biosensors and sensing devices for drug delivery” *J. Control. Release* 2016 (240):142-50.

Pescosolido L., Feruglio L., Farra R., Fiorentino S. M., Colombo I., Coviello T., Matricardi P., Hennink W. E., Tina Vermonden T., Grassi M. “Mesh size distribution determination of interpenetrating polymer network hydrogels” *Soft Matter* 2012 (8):7708-15

Peppas N.A., Langer R. “New challenges in biomaterials” *Science,* 1994 (263):1715-20

Puppi D., Migone C., Grassi L., Pirosa A., Maisetta G., Batoni G., Chiellini F. “Integrated three-dimensional fiber/hydrogel biphasic scaffolds for periodontal bone tissue engineering” *Polym. Int*. 2016 (65):631–40

Qiu Y., Park K. “Environment-sensitive hydrogels for drug delivery” *Adv. Drug Deliv. Rev.* 2012 (64):49-60

Rajeswary B., Sowmya C., Suryaprakash C, Priyanka P., Chandana S. “An overview on hydrogels” *Int. J. Pharm.Tech.* 2016 (8): 3978-90

Raub, C.B., Suresh, V., Krasieva, T., Lyubovitsky, J.,Mih, J.D., Putnam, A.J., et al. “Noninvasive assessment of collagen gel microstructure and mechanics using multiphotonmicroscopy”. *Biophys. J.* 2007(92):2212-22

Singh N.K., Lee D.S. “In situ gelling pH- and temperature-sensitive biodegradable block copolymer hydrogels for drug delivery” *J. Control. Rel.* 2014 (193):214–27

Tao J., Zhang J., Hu Y., Yang Y., Gou Z., Du T., Mao J., Gou M. “A conformal hydrogel nanocomposite for local delivery of paclitaxel” *J. Biomater. Sci. Polym. Ed.*. 2017 (28):107-18

Thiele J., Ma Y., Bruekers S.M.C., Ma S., Huck T.S.W.,” 25th Anniversary Article: Designer Hydrogels for Cell Cultures: A Materials Selection Guide” *Adv. Mat*. 2014 (26):125–48

Tranoudis I., Efron N. “Water properties of soft contact lens materials” *Cont Lens Anterior Eye*. 2004 (27):193-208

Ulijn R.V., Bibi N., Jayawarna V., Thornton P.D., Todd S.J., Mart R.J., Smith A.M., Gough J.E. “Bioresponsive hydrogels” *Mater. Today* 2007 (10):40-8

Vermonden T., Censi R., Hennink W.E. “Hydrogels for Protein Delivery” *Chem. Rev*. 2012 (112):2853–88

Wang T., Chen L., Shen T., Wu D. “Preparation and properties of a novel thermo-sensitive hydrogel based on chitosan/hydroxypropyl methylcellulose/glycerol” *Int J Biol Macromol.* 2016 (93):775-82. Wendt SL. “Nonprecious cast-metal alloys in dentistry” *Curr. Opinion Dent.,* 1991 (1):222

Wichterle O., Lim D. “Hydrophilic Gels for Biological Use” *Nature* 1960 (185): 117-8

Widowati S. “Biocompatibility Issues of Biomaterials” Chapter-Biomaterials and Medical Devices- *Adv. Struct. Mat* , 2016 (58): 41-65

Xiaochu D., Gao J., Awadaa H., Wang Y. “Dual physical dynamic bond-based injectable and biodegradable hydrogel for tissue regeneration” *J. Mat. Chem. B.* 2016 (4): 1175-85

Xu Y., Han J. , Lin H. “Fabrication and characterization of a self-crosslinking chitosan hydrogel under mild conditions without the use of strong bases” *Carb. Polym.* 2017 (156): 372–79

Yaguea M.A.F., Abbaha S.A., McNamarab L., Zeugolisa D.I., Pandita A., Biggsa M.J. “Biomimetic approaches in bone tissue engineering: Integrating biological and physicomechanical strategies” *Adv. Drug Deliv.* Rev. 2015 (84):1-29

Zhang Y., Yu J., Bomba H.N., Zhu Y., Gu Z. “Mechanical Force-Triggered Drug Delivery” *Chem Rev*. 2016 (116):12536-63

Zhang H., Zhai Y., Wang J., Zhai G. “New progress and prospects: The application of nanogel in drug delivery” *Mater Sci Eng C Mater Biol Appl*. 2016 (60):560-8

2 Analysis methods

As strongly stressed, an important feature of polymeric gels is that they can be designed for drug delivery purposes, releasing the therapeutic agent in a controlled manner. The correlation between drug release kinetics and mesh size of hydrogel network has been extensively elucidated (Brazel and Peppas, 2000) (Turco et al., 2011). Hence, the importance to control the crosslinking density in a polymer network is crucial for a controlled release device.

In this section, different methods for hydrogels characterization are discussed. The first group of methods investigates the nanometric structure of the material, addressed to the estimation of mesh size of the polymer network. Rotational rheology, low field nuclear magnetic resonance (LF-NMR) and release test belong to this group. The second group of techniques, comprehending Transmission Electron Microscopy (TEM) and X-ray Microcomputed Tomography (μCT), were utilized for imaging hydrogel. Hence, TEM and μCT are briefly presented in this chapter. On the contrary, a deeper theoretical background was presented for rheology and LF-NMR spectroscopy as these techniques represents the core of the experimental characterisation developed in this work.

2.1 Rheology

Rheology is the science that studies the mechanical behavior of fluids/solids and correlates it with their structural properties. In particular, rheology deals with the experimental/theoretical relation existing between the deformation (γ) / velocity of deformation ($\dot{\gamma}$) of a material (solid, liquid) and the stress (τ) that caused γ (solid) or $\dot{\gamma}$ (liquid) (Lapasin and Pricl, 1995). Rheometry refers to the experimental techniques used to determine the rheological properties of materials. From the mechanical response of the material, by means of elaborated theories and models, the structural properties of complex system, like for instance

dispersions, emulsions and gels, can be elucidated. In particular, for hydrogels, the combination of measurements and modeling might reveal the mean mesh size (ξ) of polymeric network and its size distribution.

The rheometer used in the work is a controlled stress rotational rheometer Haake Mars III (Figure 2.1A) equipped with a Peltier temperature control system and with a set of different geometry sensors to test the samples in a wide range of conditions. The magnetic induction motor applies a torque moment ($0.01\ \mu Nm < M < 200$ mNm) on the mobile (rotating) part of the sensor (stem) that transfers a stress (τ) directly to the sample put in between the rotating and the steady sensor part. The effect of τ is to provoke a deformation of the sample in the case of solid samples or a flow in the case of liquid/viscoelastic samples. The angular displacement or the angular velocity (Ω) are measured by means of a laser crossing a holed crown rigidly connected to the sensor mobile part. The angular resolution is 12 nRad (690 nano-degrees). The holed crown and the stem belong to the rheometer rotor that is maintained in a contactless condition with respect to the rheometer fixed part by means of an air pressure system (≈ 2 bar = 0.2 MPa). Plate surface can be smooth (Figure 2.1.1C) or shagreened (Figure 2.1.1B) in order to prevent wall slippage, this being typical of gels. Finally, in order to avoid possible sample alterations due to solvent (water) evaporation, a glass solvent trap covers the measuring zone, i.e. the rotating and the steady sensor parts. The available geometries are parallel plates or cone-plate characterized by different diameters ($2\ cm \leq d \leq 6\ cm$). Lower diameter sensor is devoted to highly viscous samples while low viscous samples need higher diameter sensor in order to improve measurements accuracy. In addition, cone and plate sensors are used in the case of homogeneous samples while heterogeneous samples (i.e. those composed by a secondary phase dispersed in the primary continuous phase) require the use of plate and plate sensor. Indeed, in the plate and plate configuration, it is possible adjusting at the desired value the gap between the rotating and steady sensor parts. This is of paramount importance since the gap must be at least ten times the dimension of the biggest secondary particles/clusters/aggregates contained in the continuous primary phase. If it

were not the case, the rheological measurement would damage the sample structure, this resulting in unreliable determination of sample properties.

Figure 2.1 (**A**) The controlled stress rotational rheometer Haake Mars III. (**B**) Shagreened plate-plate device with 35 mm diameter (PP35 Ti 96010). (**C**) Smooth cone-plate device with 60 mm diameter (C60/1° 99018)

Rotational measuring systems require special attention to limit systematic errors during the operative phase. The most common sources of errors are:

- *Inertial effects*: at high shear rate, toroidal secondary fluxes within the sample leads to an overestimation of the viscous properties and, as consequence, the torque moment results higher than real. This is an artifact not related to the rheological properties.
- *Geometrical effects*: when the sample is in excess, asymmetric edge effects are generated and they can give origin to other errors due to from a wrong assets resulting in an acentric rotation, misalignment and vertical oscillations of the rotor.
- *Instability effects*: when the applied torque is too high it can fracture the sample, this resulting in loss of adherence, slippage and splitting out of the sample by centrifugal forces.
- *Shear heating*: due to energy dissipation, a not uniform temperature field can take place inside the gap.

In order to minimize all these source of errors, the shagreened plate-plate configuration (PP35F; diameter 35 mm) (Figure 2.1B) was adopted for gels, while the cone-plate geometry (C60/1°; diameter 60 mm, cone angle 1°) (Figure 2.1C) was used for solutions. In all experiments, to ensure more consistent environmental conditions and to limit the evaporation, a glass bell (solvent trap) was used to cover the measuring device.

2.1.1 Stress Sweep tests

The stress sweep test (SS) consists in applying a sinusoidal deformation to sample characterized by an increasing deformation (γ_0) and a constant frequency (*f*, typically 1 Hz) or pulsation ($\omega = 2\pi f$):

$$\gamma = \gamma_0 sin(\omega t) \qquad \text{eq.2.1}$$

where *t* is time. Consequently, the deformation velocity (shear rate; $\dot{\gamma}$) is given by:

$$\dot{\gamma} = \gamma_0 \omega \cos(\omega t) = \dot{\gamma}_0 \cos(\omega t) \qquad \text{eq.2.2}$$

where $\dot{\gamma}_0$ is the deformation velocity associated to deformation γ_0. It can be demonstrated that, in order to have the sinusoidal deformation descripted by eq.2.1, it is necessary applying the following sinusoidal stress field (τ):

$$\tau = \tau_0 \sin(\omega t + \delta) = \tau_0 \cos\delta \sin(\omega t) + \tau_0 \sin\delta \cos(\omega t) \qquad \text{eq.2.3}$$

where τ_0 is the maximum stress (associated to γ_0) and δ is the loss angle between stress and deformation. The first term of the eq.2.3 ($\tau_0 \cos\delta \sin(\omega t)$) is related to the elastic component of the stress (i.e. that in phase with deformation), while the second ($\tau_0 \sin\delta \cos(\omega t)$) is referred to the viscous component of the stress (i.e. that in square phase with deformation). When δ=0 or δ=$\pi/2$, the sample reacts as a totally elastic (solid) or a totally viscous (liquid) material, respectively. Rewriting eq.2.3 as follows:

$$\tau = G'\gamma_0 \sin(\omega t) + G''\gamma_0 \cos(\omega t) \qquad \text{eq.2.4}$$

the elastic or storage modulus, *G'*, connected to the elastic energy stored in the material upon deformation, and the loss or viscous modulus, *G''*, associated to the energy dissipated due to internal friction inside the fluid (viscosity), are defined. It is clear from eq.2.4 that the stress τ can be expressed as the sum of contributes in

phase with the deformation and one in square phase with deformation, being G' and G'' the respective weights of these contributes.

While the complex modulus G^* is defined as the ratio between the stress (τ_0) and the associated deformation (γ_0):

$$|G^*| = \sqrt{(G')^2 + (G'')^2} = \sqrt{\left(\frac{\tau_0 \cos\delta}{\gamma_0}\right)^2 + \left(\frac{\tau_0 \sin\delta}{\gamma_0}\right)^2} = \frac{\tau_0}{\gamma_0} \qquad \text{eq.2.5}$$

the loss angle δ can be defined as:

$$\tan\delta = \frac{G''}{G'} \qquad \text{eq.2.6}$$

Practically, SS implies the determination of G' and G'' considering increasing values of τ_0, being ω the same (typically, 2π rad/s) as shown in Figure 2.2

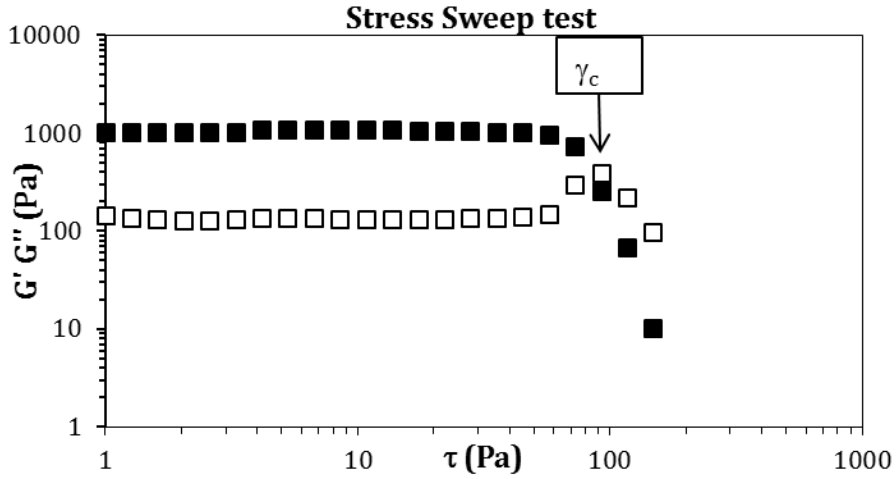

Figure 2.2 Typical stress sweep test: elastic modulus G' (black square) and loss modulus G''(open square) are no strain (τ) dependent in the viscoelastic region, after critical deformation γ_c reaching, both moduli decrease.

SS is mainly designed to determine the extension of the linear viscoelastic region (LVR), i.e. the region of small deformations/stresses where both G' and G'' do not depend on τ_0 or γ_0. When, on the contrary, deformation/stress becomes too high, both G' and G'' depends on γ_0/τ_0. Typically, while G' decreases with γ_0, G'', after an initial increase, undergoes an abrupt decrease (see Figure 2.2). The deformation/stress corresponding to the exit from the LVR is called critical (γ_c/τ_c). Above this critical threshold, the material structure collapses and this is the reason why rheologists are mainly interested in working inside the LVR, where sample structure is maintained.

2.1.2 Gap set-up: Short Stress Sweep tests (sSS)

The placement of the sample in the measurement position between the steady and the rotating part of the sensor represents a very important step. Accordingly, in the case of system that cannot be spread (as it usually happens for gels), the sample is firstly cut in a disc matching the sensor diameter, put on the steady plate, and, then, the mobile part of the sensor is moved down until it gets contact with the sample. While a weak contact often results in a false values of the moduli (typically lower than real ones), a too small gap can cause sample internal fractures, which reflects in unreliable determination of sample properties. The determination of the optimal gap is carried out by short stress sweep tests (sSS) consisting in fixing an initial gap value, measuring G', reducing the gap and measuring G' up to the occurrence of a small decrease (≈ 10% of the maximum value recorded for G') of G'. sSS is performed inside the LVR operating, usually, in the stress range 1-5 Pa and f = 1 Hz. Then, the obtained gap is kept constant for all further tests.

2.1.3 Frequency Sweep tests (FS)

Frequency sweep test (FS) consists in the application of a sinusoidal stress, with constant amplitude (τ_0) and variable frequency, usually in the range 100-0.01 Hz. The stress amplitude value is chosen within the linear viscoelastic region. The plot of G' and G'' versus pulsation ω (=$2\pi f$), is called mechanical spectrum. In figure 2.3 a typical mechanical spectrum of a gel is shown. The typical gel mechanical spectrum is characterized by a constant G' and G'' with ω. In addition, G' is about ten times higher than G'' in all the pulsation spectrum (Sarbu et al., 2000). On the contrary, solutions are characterised by $G' < G''$ with both moduli increasing with pulsation. The ideal elastic material is characterised by $G'' = 0$, while the ideal liquid material is characterised by $G' = 0$. When $G' \approx G''$ the sol-gel transition occurs.

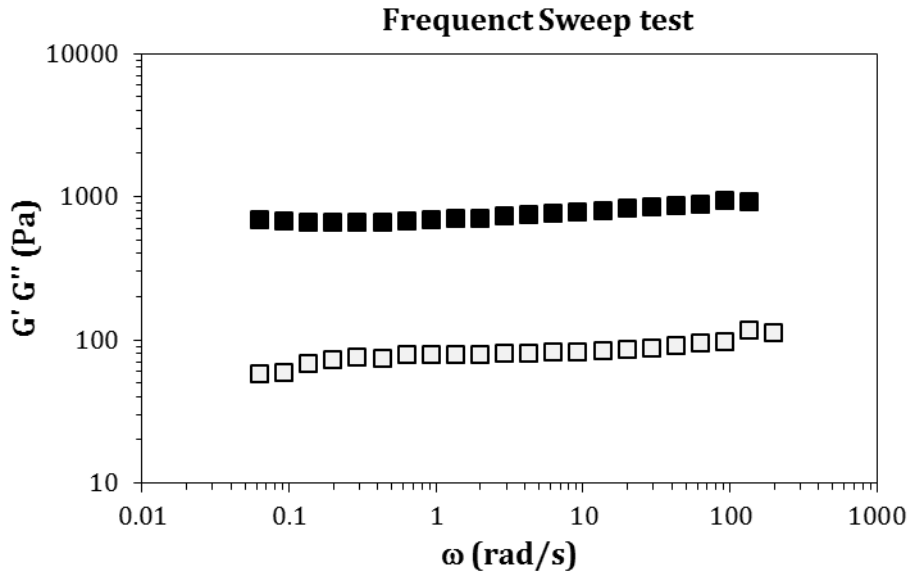

Figure 2.3 Typical hydrogel mechanical spectrum: elastic modulus *G'* (black square) and loss modulus *G''*(open square) are independent from the pulsation ω

The classification of viscoelastic behaviours is given by the value of Deborah number (*De*). This dimensionless parameter is defined by the ratio between the characteristic relaxation time, λ, representing the time required by the material structure to recover the strain after deformation, and the deformation applied time Λ: $De=\lambda/\Lambda$. As $\Lambda \propto \omega$ we have $De \propto \lambda\omega$. A pure elastic character is given by $De=\infty$, while a pure liquid one implies $De=0$. A viscoelastic behaviour is described by $0 < De < \infty$ (usually $De \approx 1$ or 10). In a FS test, to a low value of *De*, corresponds physically a deformation process longer than the test time necessary to the structure to relax. In this situation, the time frame is long enough for the material to respond as a viscous-like system to the applied stress. On the opposite site, with a deformation time shorter than λ, (for high *De*) the elastic reaction is more pronounced.

2.1.4 Steady Value test (SV)

Steady Value test (SV) is aimed at the determination of fluid shear viscosity (η) and relies on Newton law, $\tau = -\eta(\dot{\gamma})\dot{\gamma}$. Beside flow conditions (shear rate), η depends also on temperature and pressure.

In SV analysis, the fluid sample undergoes an increasing stress that reflects into increasing shear rate ($\dot{\gamma}$). Relaying on the ratio between the imposed stress (τ) and the measured shear rate ($\dot{\gamma}$), the dependence of the fluid shear viscosity on the stress can be determined (flow curve). In the case of polymer solutions, the η dependence on τ or $\dot{\gamma}$ shows a constant value for small τ (η_0, zero-shear viscosity) followed by a more or less pronounced decrease (shear thinning behavior) that ends in the second lower plateau where viscosity is independent on shear stress/rate and assumes a constant value called infinite viscosity (η_∞). This behavior is depicted in figure 2.4 in the case of a polymer solution made up by nanocellulose.

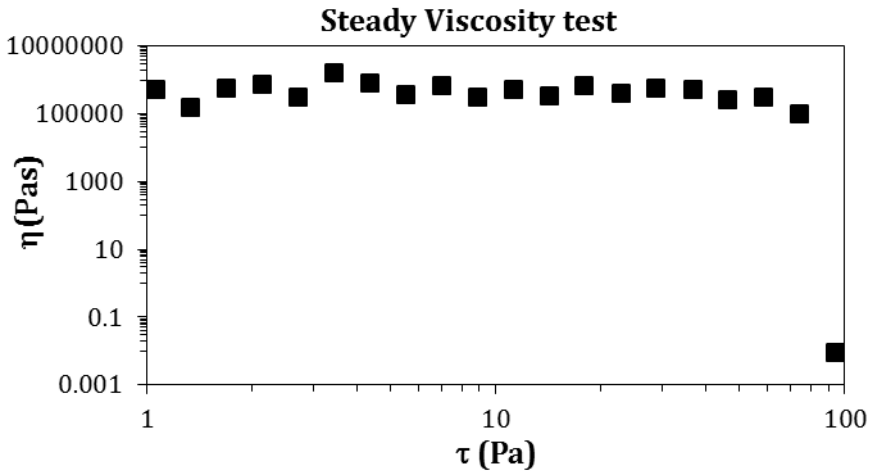

Figure 2.4 Characteristic flow curve for a shear-thinning material, increasing strain (τ) lead viscosity (black square) from an initial η_0, to a dramatically down fall, simultaneously deformation (γ) loses linear dependence from τ and grows up.

2.1.5 Temperature Sweep test (TS)

Temperature sweep curves (TS) represent the dependence of G' and G'' on temperature. Significant variations in sample mechanical properties are monitored, whereas temperature increase provokes a variation in the sample nano/micro structure. The typical situation is that of a polymeric solution undergoing a crosslinking process due to a temperature increase. In this case, the frequency is fixed at 1 Hz and the maximum value of the applied sinusoidal stress

is held constant (τ_0). As, initially, in the solution state, $G' < G''$, the condition $G' > G''$ indicates the beginning of the formation of a three-dimensional network.

2.1.6 Correlation models

Several models are used in theoretical rheology to describe the viscoelastic behaviour of fluids. Regarding interpretations of mechanical spectra, the most popular theory is the Maxwell's model. According to this theory, the reaction of viscoelastic materials to stress can be schematised by a dashpot and spring (Fig 2.5A). This physical approximation, is described by following equation (eq. 2.7)

$$\tau + \frac{\eta}{G}\frac{\partial \tau}{\partial t} = -\eta\dot{\gamma} \qquad \text{eq. 2.7}$$

where τ is the stress, $\dot{\gamma}$ the deformation (shear) rate, t the time, η the dashpot viscosity, G the spring constant and $\lambda=\eta/G$ is the Maxwell element relaxation time. The solution of eq.2.7, in the case of sinusoidal deformation $\gamma = \gamma_0 \sin(\omega t)$, leads to a stress defined by eq.2.4, where:

$$G'(\omega) = \frac{G(\lambda\omega)^2}{1+(\lambda\omega)^2} \qquad \text{eq.2.8}$$

$$G''(\omega) = \frac{G\lambda\omega}{1+(\lambda\omega)^2} \qquad \text{eq.2.9}$$

When $\omega=1/\lambda$, $G' = G''$ and this condition corresponds to the maximum value of G'' and De=1.

Generally, a viscoelastic material mechanical response needs a more complex model than the simple Maxwell element. For this purpose, n Maxwell elements can be combined in series (Figure 2.5B) building the so called "generalized" Maxwell model. Each element is characterized by a relaxation time λ_i and a viscosity η_i (or alternatively, the storage moduli $G_i=\eta_i/\lambda_i$). The G' and G'' expressions read:

$$G'(\omega) = \sum_{i=1}^{n} G_i \frac{(\lambda_i\omega)^2}{1+(\lambda_i\omega)^2} \qquad \text{eq.2.10}$$

$$G''(\omega) = \sum_{i=1}^{n} G_i \frac{\lambda_i\omega}{1+(\lambda_i\omega)^2} \qquad \text{eq.2.11}$$

The simultaneous fitting of eqs. 2.10 and 2.11 to the experimental G' and G'' vs ω data allows the determination of the unknown fitting parameters, and the function $G_i(\lambda_i)$, the so called "relaxation spectrum". As, usually (Lapasin and Pricl, 1995), the

relaxation times (λ_i) are scaled by a factor 10, model parameters are 1 + n (i.e. λ_1 plus G_i). The choice of the proper number, n, of Maxwell elements to be considered relies on a statistical procedure (Draper and Smith, 1966) according to which the optimal n is that minimizing the product $\chi^2(1+n)$. χ^2 is the sum of the squared errors deriving from the simultaneous eq.2.8 and eq.2.9 fitting to the experimental G' and G'' trend. In this model, besides the Maxwell elements, a pure elastic element (a spring), G_E, can be added. This element is characterised by an infinite relaxation time.

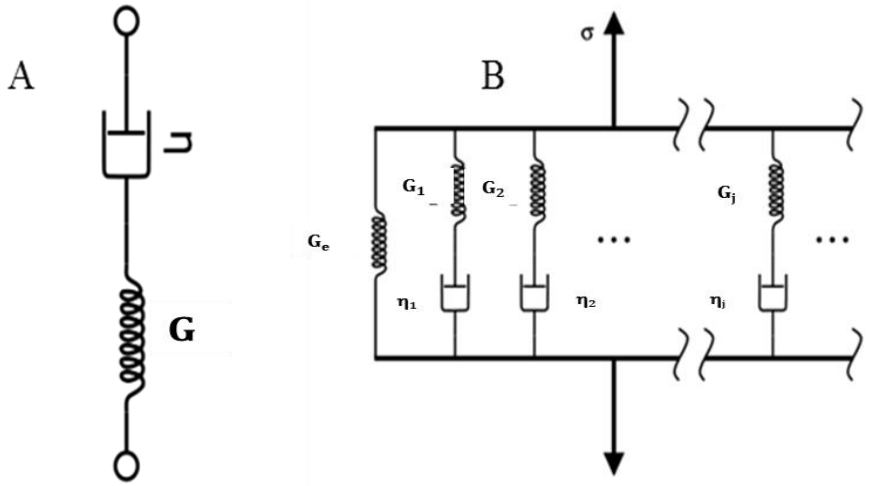

Figure 2.5(**A**) Maxwell element; (**B**) more Maxwell elements put in series with a pure elastic element.

2.1.6.1 Estimation of average mesh size from rheological studies

As mentioned in section 1.4, an important feature of a polymeric gel networks, is the density of crosslinks, ρ_x, defined as the moles of polymeric inter-chains junctions per gel unit volume. In this sense, the rheological characterization reveals to be an important tool, as it allows an estimation of sample shear modulus G. Indeed, from the Flory's theory (Flory, 1953), for a non-compressible crosslinked gel subjected to deformation in the linear viscoelastic region, the shear modulus G is equal to one third of the Youg modulus E (Lapasin and Pricl, 1995). G can be estimated from the sum of the Maxwell elastic elements g_k and G_E:

$$G = \sum_{k=1}^{N} g_k + G_E \qquad \text{eq.2.12}$$

In turn, always relaying on the Flory theory (Flory, 1953), ρ_x can be estimated according to:

$$\rho_x = \frac{G}{RT}\left(\frac{\phi_p}{\phi_{p0}}\right)^{2/3} \qquad \text{eq.2.13}$$

where R is the ideal gas constant , T is the absolute temperature, while ϕ_{p0} and ϕ_p are, respectively, the polymer volumetric fraction in the crosslinked conditions (reference conditions) and in the rheological measurement conditions (this means that the gel could undergo swelling or de-swelling before the analysis). ϕ_{p0} can be evaluated on the basis of the polymer mass fraction, c_0 in the crosslinking solution. Indeed, we have:

$$c_0 = \frac{m_p}{m_p + m_{H_2O}} = \frac{\rho_p V_p}{\rho_p V_p + \rho_{H_2O} V_{H_2O}} \qquad \text{eq.2.14}$$

where m_p and m_{H2O} are, respectively, polymer and solvent mass, while ρ_p and ρ_{H2O} are polymer and solvent density. At the same time, the following relation holds:

$$\phi_{p0} = \frac{V_p}{V_p + V_{H_2O}} = \frac{m_p/\rho_p}{m_p/\rho_p + m_p/\rho_{H2O}} \qquad \text{eq.2.15}$$

From eq.2.14 we can find a relationship for V_p (polymer volume) as a function of c_0:

$$V_p = \frac{\rho_{H2O}}{\rho_p} * \frac{c_0}{1-c_0} V_{H2O} \qquad \text{eq.2.16}$$

Inserting eq.2.16 into eq.2.13, we obtain another equation for ϕ_{p0}:

$$\phi_{p0} = \frac{1}{1+\frac{1-c_0}{c_0} * \frac{\rho_p}{\rho_{H2O}}} \qquad \text{eq.2.17}$$

Upon gel swelling/de-swelling, the polymer volume fraction ϕ_p will differ from its initial value ϕ_{p0}. This difference can be evaluated measuring the gel relative weight change (Δw) due to water absorption/de-absorption.

$$\Delta w = \frac{\Delta M_{H2O}}{M_0} = \frac{M - M_0}{M_0} \qquad \text{eq.2.18}$$

where M_0 is the gel mass in the reference state and M the gel mass after swelling/de-swelling. Thus, the correspondent volume change (ΔV_{H2O}) is given by:

$$\Delta V_{H2O} = \frac{\Delta M_{H2O}}{\rho_{H2O}} = \frac{\Delta W}{\rho_{H2O}} M_0 = \frac{\Delta W}{\rho_{H2O}}\left(\frac{\rho_p}{\rho_{H2O}} V_p + \rho_{H2O} V_{H2O}\right) \qquad \text{eq.2.19}$$

ϕ_p is by definition:

$$\phi_p = \frac{V_p}{V_p + V_{H2O} + \Delta V_{H2O}} \qquad \text{eq.2.20}$$

Substituting eq.2.19 and eq.2.16 in last equation 2.20, we obtain an expression for ϕ_p which depends only on density values (knowns) and ϕ_{p0} (acquired from c_0 that is still known)

$$\phi_p = \frac{\phi_{p0} * \rho_{H2O} * c_0}{\rho_{H2O} * c_0 + \Delta w * \rho_{H2O} * v_{p0}} \qquad \text{eq.2.21}$$

Coming back to the density of crosslinks, the link between ρ_x and the average mesh size, ξ_{rheo}, is established by the "equivalent network theory" (Schurz, 1991). Starting from the evidence that, in most cases a detailed description of a real polymeric network is rather complicated, if not impossible, this theory suggests replacing the real network topology by an idealized one, sharing the same ρ_x. (Fig.2.6). In addition, the idealized network is made up by a collection of identical spheres centered on each cross-link. Hence, the product of crosslink density and the Avogadro's number ($\rho_x * N_A$), gives the number of crosslinks per unit volume, and therefore the inverse is the mean, spherical, volume referred to each crosslink:

$$\frac{1}{\rho_x N_A} = \frac{4}{3}\pi\left(\frac{\xi_{rheo}}{2}\right)^3 \xrightarrow{that\ gives} \xi_{rheo} = \sqrt[3]{\frac{6}{\pi \rho_x N_A}} \qquad \text{eq.2.22}$$

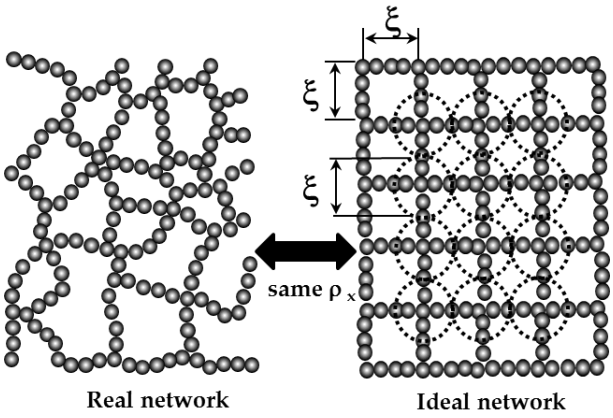

Figure 2.6 Schematic representation of a real polymeric network (grey spheres indicate rigid chain segments) and the ideal one according to the equivalent network theory. ρ_x and ξ indicate, respectively, network crosslink density and ideal network mesh size.

It is important to point out that ξ_{rheo} is the average mesh size in the network. Obviously, as the real network is not homogeneous, the knowledge of the mesh size distribution would be much more interesting. LF-NMR spectroscopy can be used to provide this kind of network characterization.

2.1.6.2 Alternative estimation method for average mesh size

As alternative way for the estimation of the average mesh size, ξ_{avg}, was shown in an interesting work about polymeric networks like gels (Scherer, 1994). Scherer

proposed an equation to correlate the hydraulic radius of the network mesh (R_h) with polymeric fibres radius (R_f), ξ_{avg}, depending on the cubic, octahedral or tetrahedral shape of the meshes. This model turned to be especially appropriate for LF-NMR data interpretation, since this technique is essentially affected by R_h. The model key-equation reads:

$$\frac{R_h}{R_f} = \frac{2c_0(1-\phi_p)}{2c_1\left(\frac{R_f}{\xi_{avg}}\right)^2 - 3c_2\left(\frac{R_f}{\xi_{avg}}\right)^3} \qquad \text{eq.2.23}$$

where c_0, c_1 and c_2 are constants relative to the cell (mesh) geometry (for cubic mesh, the three constants are 1, 3π and $8\sqrt{2}$, respectively (Scherer, 1994)). The model is valid for ϕ_p<0.942 (as previous reported, ϕ_p is the polymer volume fraction), corresponding to a ratio R_f/ξ<0.5, that means for very small mesh size. It can be demonstrated (Grassi, 2015) that for ϕ_p <0.4, eq. 2.21 can be reliably approximated by the following relations among ξ, R_f, R_h and ϕ_p:

$$\frac{\xi}{R_f} = \sqrt{\frac{1-\phi}{\phi}\frac{c_1}{c_0}} \qquad \text{eq.2.24}$$

$$\frac{R_h}{R_f} \approx \frac{(1-0.58\phi)}{\phi} \qquad \text{eq.2.25}$$

Combining eqs. 2.24 and 2.23 we obtain the ratio R_h/ξ and ξ:

$$\frac{R_h}{\xi} = \frac{(1-0.58\phi)}{\phi}\sqrt{\frac{\phi}{1-\phi}\frac{c_0}{c_1}} = f(\phi) \qquad \text{eq.2.26}$$

When $\phi_p \leq 0.4$, eq.2.26 detaches from the Sherer theory of less than 10%.

It is worth nothing that, the value of ξ_{avg} coming from this theory is purely theoretical, as it derived by the assumption that the network is a lattice composed by regular cells. Nonetheless, Sherer's theory was successfully used for the interpretation of LF-NMR data by many works in this field (Dalmoro et al., 2017).

2.2 Low Field Nuclear Magnetic Resonance (LF-NMR)

2.2.1 NMR spectroscopy

In the case of hydrogels, NMR spectroscopy allows quantifying the interaction between water hydrogen atoms (protons) and polymer chains constituting the three-dimensional network. Concretely, it provides an estimation of the response

of water protons spins upon a magnetic excitation, which is strictly connected to protons degree of interaction with the polymer chains. This information, combined with the estimation of average mesh size (obtained from the theoretical approach shown in section 2.1.6.2), allows the determination of the mesh size distribution.
Before focusing the attention on the LF-NMR experiments performed in this thesis, it is useful describing the physical principles and the basic theoretical background behind NMR.

2.2.1.1 Quantum mechanics models for isolated nucleus

The physical principles of NMR spectroscopy, are based on the magnetic behaviour of atomic nuclei (Günther, 1992). According to quantum mechanics, the excitation of an atomic nucleus by external magnetic fields produces a transition of nucleus energy in the quantized energetic levels. This energy absorption could be detected by the instrument and registered as a signal on a spectrum. Detections examine only compounds that contains atoms with nuclear magnetic moment (μ) different from zero, such as protons (^{1}H), fluorine (^{19}F) and the isotope ^{13}C of carbon (Günther, 1992). Many atomic nuclei present an angular moment, P, being responsible for the exhibition of μ. Indeed, a direct relation exists between P and μ: $\mu = \gamma P$, where γ is the gyromagnetic ratio depending on the nucleus composition. According to the quantum theory, P and μ are quantized, and the allowed autovalues for P maximum components in z direction, in a cartesian system (P_z), are connected to magnetic quantum number (m_I), in turn related to nuclear spin quantum number (I). For protons (^{1}H) I = ½, and they exist only in two quantum states characterized by m_I = +½ and m_I = -½; therefore if P_z is given by:

$$P_z = \frac{h}{2\pi} m_I \xrightarrow[for\ protons]{} = \frac{h}{2\pi} I \qquad \text{eq.2.27}$$

(where h is the Plank constant), then angular moment z (μ_z) will be:

$$\mu_z = \pm\gamma \frac{h}{4\pi} \qquad \text{eq.2.28}$$

Protons could be identified as a magnetic dipole, where μ_z can be parallel or antiparallel to the positive direction of z axis (as represented in figure 2.7). Without the external filed (situation A), the two states have the same energy and

the probability of being parallel or antiparallel is the same. On the contrary, in presence of an external magnetic field B_0 (situation B), the interaction with μ causes an energetic splitting of the two states.

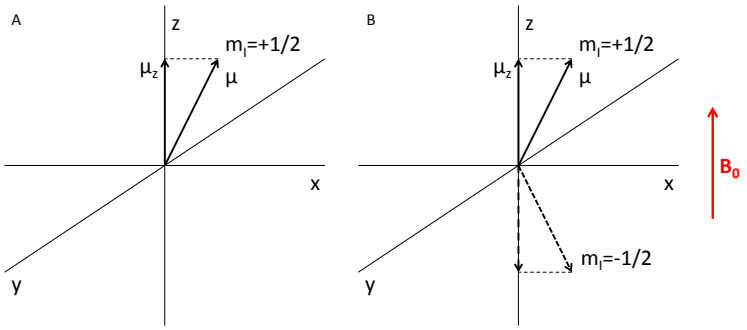

Figure 2.7 Vectorial representation of the magnetic moment μ in absence (**A**) or in presence (**B**) of an external magnetic field B_0**.**

If B_0 is parallel to z axis, the magnetic dipole assumes an energy equal to $+\mu_z B_0$ (dipole is oriented in the same direction of B_0), or $-\mu_z B_0$ (with the opposite direction). The energetic difference between the two spin states is proportional to the intensity of B_0:

$$\Delta E = 2\mu_z B_0 \qquad \text{eq.2.29}$$

The state at lower energy (m_I = +½) is more stable and to induce the transition to the higher energy level (m_I = -½) a quantum of energy corresponding to ΔE is required. This energy has to be administered by a radiation with a frequency ($\omega_0=2\pi\nu_0$) given by:

$$\nu_0 = \frac{\Delta E}{h} = \frac{\gamma B_0}{2\pi} \rightarrow \omega_0 = \gamma B_0 \qquad \text{eq.2.30}$$

where ν_0 is the so called "Larmor frequency" that depends linearly on the intensity of B_0. For example, in the case of ^1H (gyromagnetic ratio $\gamma_H = 2.676*10^8$ rad $T^{-1}s^{-1}$), when B_0 = 1.41 T, the Larmor frequency ν_0 is 60 MHz, this corresponding to a radiation lying in the radio waves field (λ=5 m).

2.2.1.2 Energy absorption mechanism: the "Resonance"

Usually, protons are represented as magnetic bars but, because of nuclei spin rotation, their behaviour is a bit different. Inside a static magnetic field B_0, rotating nuclei do not align their magnetic moments to the direction of the field, but their

spin axis assumes a precession movement around B_0 direction (Fig.2.8A). The precession frequency corresponds to the Larmor frequency ν_0 (eq.2.30) (Günther, 1992; Atta-ur-Rahman, 1986).

A rise in intensity of the magnetic field produces a faster precession. Moreover, in presence of a rotating magnetic field (B_1) perpendicular to B_0, it is also possible modify μ orientation. When B_1 rotation frequency (ν_{RF}) equals ν_0, a "resonance" condition is established: nucleus absorbs energy resulting in a variation of θ angle between vector μ and B_0 (Fig 2.8B). This energy transfer does not change precession frequency.

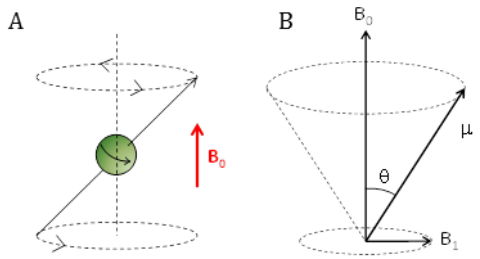

Figure 2.8(**A**) the nuclear magnetic moment assumes a precession in a magnetic field B_0. (**B**) The application of a rotating magnetic field B_1, perpendicular to B_0, moves the nuclear magnetic moment μ by an angle θ.

2.2.1.3 Macroscopic magnetization

While a sample is analysed by NMR, a huge number of nuclei are subjected to the magnetic field. The "nuclear magnetization" (defined as magnetic moment per unit volume), M is a vector divided into three components: conventionally, M_z aligned to B_0, while M_x and M_y lying in the xy plane perpendicular to B_0. For a nucleus with I=1/2, all magnetic moments follow a precession to the same frequency and the magnetization vectors are randomly oriented on x and y axes. Hence, they cancel themselves and the overall M_{xy} =0 (no phase coherence). Contrarily, in z direction, there is a small excess of nuclei parallel to B_0 (Boltzmann distribution favours the lowest energy state). The difference between parallel and antiparallel magnetized nuclei population (N_1 and N_2), generates a macroscopic magnetization M_z (Fig.2.9A):

$$M_z = \gamma h(N_1 - N_2) \qquad \text{eq.2.31}$$

The application of a radiofrequency (*RF*) field B_1 rotating at the resonance frequency ($\omega_0=\gamma B_0$; eq. 2.30), allows the spin resonance with a modification of the casual orientation in the *xy* plane and the appearing of a magnetization component $M_{xy}\neq 0$. Spin systems originating net component of the magnetization in the *xy* plane (M_{xy}) are in phase coherence (Fig.2.9B).

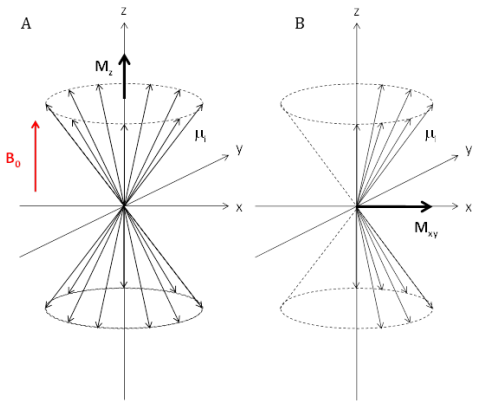

Figure 2.9(**A**) Vectorial representation of magnetic moments of I=1/2 nuclei, following a precession around z axis with no magnetization on xy plane, but an overall magnetization M_z. (**B**) Spin system in phace coherence, $M_{xy}\neq 0$.

2.2.2 The NMR experiment: relaxation time measurement

A schematic representation of NMR equipment is shown below (Fig.2.10). The sample is inserted in a glass cylindrical vial put in the middle of the coil which creates a highly homogeneous static magnetic field B_0.

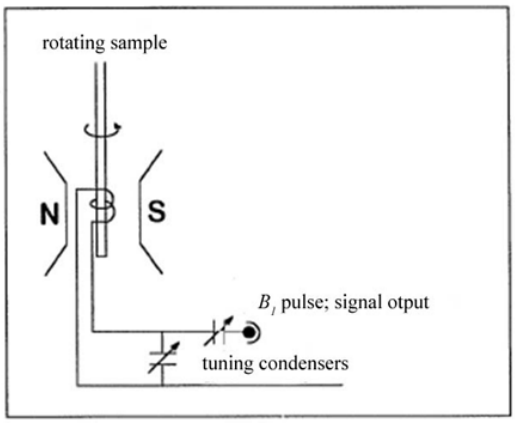

Figure 2.10 Schematic representation of the NMR spectroscope. The sample is positioned within the magnetic field B_0 generated by a magnet (N-S) and surrounded by a spire, tuned on the resonance frequency, that produce the B_1 pulse

As explained before, the phase coherence within spins, is induced by a rotating filed B_1 perpendicular to B_0, following by a generation of M_{xy} magnetization component with a ω_0 precession. When B_1 is removed, magnetization undergoes a relaxation process, which causes the loss of phase coherence ($M_{xy}\neq 0$) and the return to initial equilibrium situation ($M_{xy}=0$). The relaxation follows an exponential decay of M_{xy} characterized by a constant time T_2 ("spin-spin-" or "transversal-" relaxation time), while T_1 is the characteristic time of M_z increase, also called "spin-lattice", or "longitudinal-"relaxation time.

The result of the relaxation is a transient signal, captured by a sensor on x axes, with ω_0 frequency and decay speed of $1/T_2$ called Free Induction Decay (FID) (Atta-ur-Rahman, 1996). NMR spectral signals are produced by the small displacement of ω_0, caused by the physic-chemical environment, in nuclei population under analysis. When different ω_0, that means different $1/T_2$, are present, the resulting FID is a superimposition of all signals. The complex FID originated by multiple signals is solved using a Fourier transformation that changes the transient signal in normal spectrum. Whereas NMR spectrum is a diagram where intensity is a function of frequency, in FID the intensity is a function of time. Fourier transformation connects time and frequency domains (Atta-ur-Rahman, 1996).

Similarly to what happens in B_0 field, the precession concept can be extended to B_1 using a conceptual artefact of a rotating reference system. With respect to this new rotating axis system, B_1 becomes a static field. When B_1 is applied (aligned to rotating axes x) the equilibrium magnetization M_0, aligned to z axis, follow a precession around B_1. The M_0 precession frequency is $\omega_1 = \gamma \mathrm{B}_1$, where ω_1 is the angular frequency (rad/s). M_0 rotates with an angle given by $\theta = \gamma B_1 t_\mathrm{p}$, where t_p is the pulsation time for B_1 and γB_1 is the pulse amplitude. After a pulse of 90° ($\pi/2$), $M_{xy}=M_0$; while after a 180° pulse (π), $M_z=-M_0$. Figure 2.11 illustrates in details the change of magnetization during a pulsed NMR experiment in a rotating coordinate system. At the beginning, the overall magnetization M_0 is aligned to the magnetic field B_0 (axis z direction) (Fig.2.11A). After the application of a rotating field, B_1, the magnetization deflects of $\pi/2$, moving magnetization vector (Fig.2.11B) and, for a pulse of sufficient duration, reaches the final position on the $x'y'$ plane, generating

M_{xy} magnetization component (Fig.2.11C). At the end, when B_1 is removed, the relaxation process starts and the phase coherency is lost, causing exponentially decay of M_{xy} component (Fig2.11D and E) with the time constant T_2. This FID signal is detected on a receiving spire z axis (Atta-ur-Rahman, 1996).

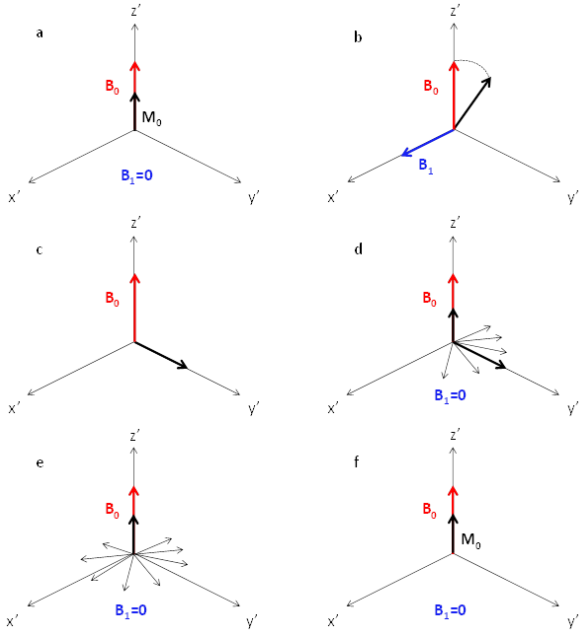

Figure 2.11 Diagrams in the rotating coordinate system x'y'z' showing the magnetization during an NMR experiment. (**A**) the overall magnetization M_0 is aligned to B_0. (**B**) and (**C**) a rotating field B_1 is applied perpendicular to B_0; the pulse length is sufficient to rotate the magnetization by 90°. (**D**) and (**E**) after B_1 ceasing, the spins start to relax by a spin-spin mechanism on the $x'y'$ plane (time constant T_2) and by a spin-lattice mechanism on the z' direction (time constant T_1). (**F**) After sufficient time, the starting equilibrium magnetization M_0 is re-established.

Together with M_{xy}, also the longitudinal component of magnetization M_z during relaxation comes back to the initial equilibrium magnetization M_0 (Fig2.11F). The relaxation of M_{xy} and M_z is given by:

$$\frac{dM_{xy}}{dt} = -\frac{M_{xy}}{T_2} \qquad \frac{dM_z}{dt} = -\frac{M_0 - M_z}{T_1} \qquad \text{eq.2.32}$$

whose solution is:

$$M_{xy} = M_0 e^{-\frac{t}{T_2}} \qquad M_z = M_0\left(1 - e^{-\frac{t}{T_1}}\right) \qquad \text{eq.2.33}$$

Although, in principle, M_{xy} extinction in the xy plane and the simultaneous M_z growth in the z direction could be studied by the application of the orthogonal field B_1, this is not practically possible due to the presence of unavoidable magnetic field

inhomogeneity provoking the fanning out of the magnetization vector (*M*) just after the 90° rotation (see Figure 2.12)

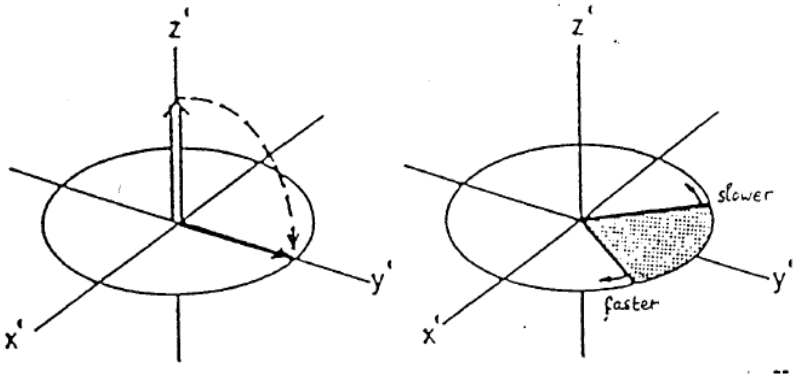

Figure 2.12 Magnetization rotation on the y axis (left) and fanning-out phenomenon (right) where the nuclear magnetic moments characterized by lower precession speed rotate anti-clockwise while those characterized by higher precession speed rotate clockwise.

Fanning out is due to the fact that inhomogeneity implies the existence of nuclear magnetic moment (μ) of different precession velocities (signal de-phasing) (Hore, 1995). This would turn out in a too weak signal (FID, echo) to be detected. In order to solve this problem, the Hahn Spin Echo sequence was designed in 1950 (Hahn, 1950) (see Figure 2.13). This approach implies the use of a pulse sequence consisting in the first 90° pulse followed, after a time τ, by a second pulse implying a further magnetisation rotation of 180° around the x axis. The second pulse causes the 180° rotation, around the x axis, of all the signals that, maintaining their rotation sense around the z axis, will momentary meet after a time τ after the 180° pulse.

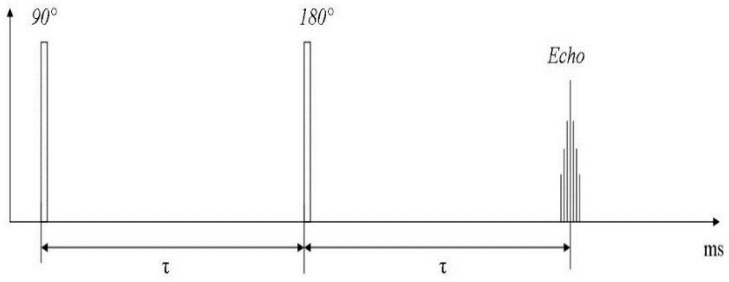

Figure 2.13 Hahn Spin-echo sequence. τ is the time elapsed between the 90° and 180° pulses.

In so doing, the fan closes and the signal re-phasing occurs (see Figure 2.14). Thus, after a time 2τ, signal re-phasing will make the signal (FID, echo) maximal.

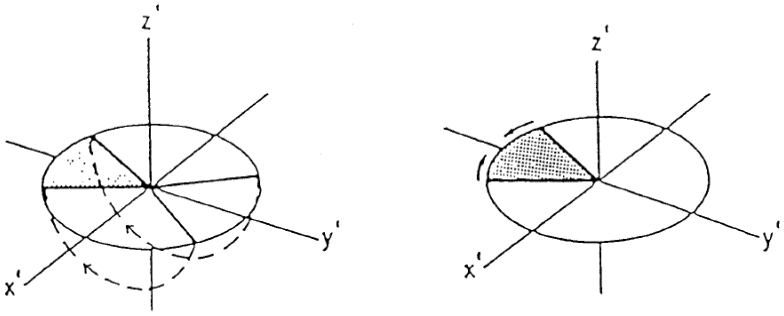

Figure 2.14 Hahn Spin-echo sequence. τ is the time elapsed between the 90° and 180° pulses.

2.2.2.1 Data analysis of LF-NMR

Low field NMR indirectly provides information on sample structure resorting to the relaxation behavior of ^{1}H contained in the sample. NMR can be applied to both solid and liquid samples, suspensions, gels and emulsions. It is nondestructive method. LF-NMR equipment used in this investigation is a Bruker Minispec mq20™, which operates at a frequency of 20 MHz, the ^{1}H Larmor precession frequency corresponding to B_0~0.47 T. The system is provided by thermostatic bath for the temperature control. The measurement consists of a sequence of magnetic excitations that can be considered an extension of the Hahn Spin-echo sequence and is known as the Carr-Purcell-Meiboom-Gill (CPMG) pulse sequence (Carr et al., 1954) (see Figure 2.15).

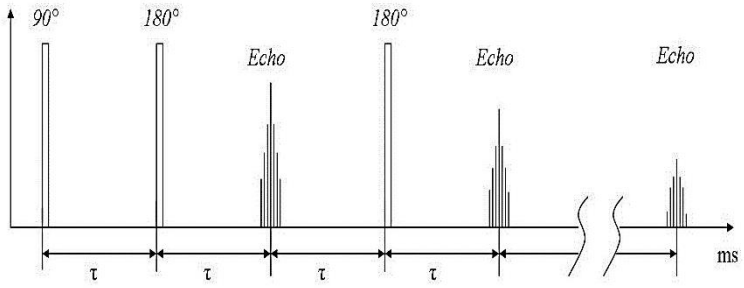

Figure 2.15 Carr-Purcell-Meiboom-Gill (CPMG) pulse sequence.

This sequence is equal to the Hahn spin-echo sequence except for the presence of following 180° pulses separated by a time 2τ each other. In so doing, it is possible following the time evolution of the magnetization re-orientation. Each 180° pulse servers to get signals re-phasing. The final time relaxation trend of the magnetization is averaged on 4 repetitions, separated by 5 seconds each other.

In a simplest situation, the relaxation process of M_{xy} and M_z is mono-exponential (see figure 2.16, an example of intensity exponential decay) and only one value of T_2 and T_1 fully characterize the entire process.

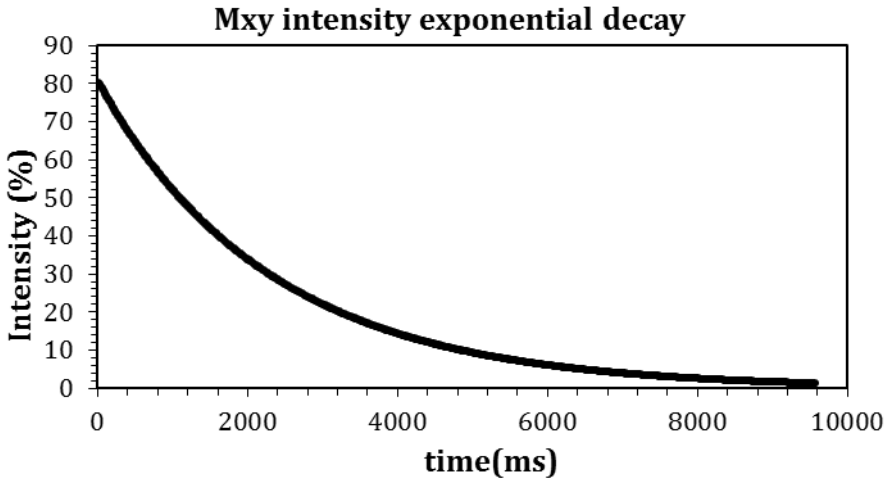

Figure 2.16 FID (echo) decay after B_1 removal.

However, in general, more than one relaxation time is required to describe the relaxation process. Indeed, T_2 and T_1 not only depend on atoms type, temperature and on magnetic field strength, but also on the environment surrounding the ^1H of the fluid contained in the sample. In particular, I refer to the effect of solid surface on the ^1H relaxation as it happens in the case of water protons trapped in a porous material. The relaxation time of protons near the solid surface is faster than that of protons not directly faced to the solid surface (Gallegos et al., 1987), owing to the interactions between protons and the solid surface (Chui et al., 1995). Thus, the relaxation of water protons, trapped in a hole, is the sum of two contributes: that of protons near the surface and that of protons far from the surface. A similar situation occurs in hydrogel, where the solid surface is represented by polymeric chains. Hence, for hydrogel structural analysis, LF-NMR analysis allows to distinguish different states of water, i.e. water trapped in meshes of different size or water outside the polymeric meshes (Vanhamme et al., 2001). It is important to

point out that it was always impossible measuring the relaxation of the protons belonging to the polymer backbone, since their relaxation resulted too fast to be detected by the equipment in use.

Summarizing, in general, the M_{xy} relaxation process can be represented by a sum of exponential decays (Chui et al., 1995)

$$\frac{M_{xy}(t>0)}{M_{xy}(t=0)} = I(t) = \sum_{i=1}^{m} A_i e^{-t/T_{2i}} \qquad \text{eq.2.34}$$

where t is time and A_i is the pre-exponential factors (dimensionless) proportional to the number of protons relaxing with T_{2i} relaxation time. This equation holds also in case of a mixture composed by n different liquids, each one characterized by its own T_{2i}. The determination of A_i, T_{2i} and m is achieved by fitting eq.2.34 to experimental $I(t)$ (FID) values. The statistically most probable value of m is that minimizing the product $\chi^{2*}(2m)$, where χ^2 is the sum of squared errors and $2m$ represent the number of fitting parameters of eq.2.34 (Draper and Smith, 1966). The $m(A_i\text{-}T_{2i})$ couples represent the so called discrete relaxation times spectrum. In order to get the continuum relaxation time spectrum (m⟶∞), eq.2.34 has to be written in integral form:

$$I(t) = \int_{T_2^{min}}^{T_2^{max}} a(T_2) e^{-t/T_2} dT_2 \qquad \text{eq.2.35}$$

where T_{2min} and T_{2max} indicate the range of T_2 distribution and $a(T_2)$ is the unknown amplitude of the spectral component at relaxation time T_2. $a(T_2)$ determination requires eq.2.35 fitting to the experimental $I(t)$ values. At this purpose, eq.2.35 can be discretized according to the criterion of Whittal and MacKey (Whittal and MacKay, 1989)

$$I(t) = \int_{T_2^{min}}^{T_2^{max}} a(T_2) e^{-t/T_2} dT_2 \approx \sum_{i=1}^{N} a_i\left(T_2^i\right) e^{-t/T_2}\left(T_2^{i+1} - T_2^i\right) = \sum_{i=1}^{N} A_i\left(T_2^i\right) e^{-t/T_{2i}} \qquad \text{eq.2.36}$$

where the range of the T_2 distribution is logarithmically subdivided into N parts (≈200). Because of the noise disturbing the $I(t)$ experimental data, fitting procedure must not minimize the χ^2 statistic, but a smoothed version χ_s^2:

$$\chi_s^2 = \sum_{i=1}^{N}\left(\frac{I_s(t_i) - I(t_i)}{\sigma_i}\right)^2 + k\sum_{i=1}^{N-2}|A_{i+2} - 2A_{i+1} + A_i|^2 \qquad \text{eq.2.37}$$

where σ_i is i^{th} datum standard deviation, k is the smoothing term weight proposed by Provencher (Provencher, 1982). Although different criteria can be followed for k determination, the strategy adopted by Wang (Wang and Ni, 2003) can be

considered. According to this approach, eq.2.37 has to be repeatedly fitted to experimental data assuming increasing k value. As the function $Ln(\chi_s)$ vs $Ln(k)$ is linearly increasing up to a clear slope increase (curve heel), Wang suggest taking as optimal k value that occurring just after the heel. Figure 2.17 shows an example of the Wang approach. The chosen smoothing factor was k=261. Alternatively, Whittal (Whittal and MacKay, 1989) suggests, lacking further information, to choose k value ensuring that $\chi^2 \approx N$, where χ^2 is expressed by eq.2.37 with k=0. Indeed, in this case, each datum is misfit, on average, by about one standard deviation.

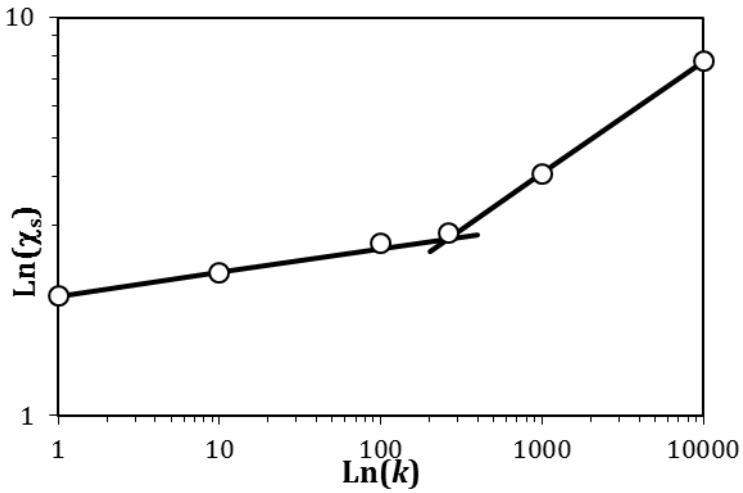

Figure 2.17: Bi-logarithmic plot of χ_s as a function of the smoothing term k. According to the criterion of Wang, k is chosen where the plot shown a change of slope.

2.2.2.2 Relation between relaxation time and the diameter

As anticipated in the previous paragraph, the interactions with polymeric chain surface render the relaxation time of protons belonging to water molecules, near the polymeric surface, faster than that of bulk water protons (Chui et al., 1995). Accordingly, in heterogeneous systems, the average relaxation time of protons will depend on the ratio between system volume and system solid surface, as demonstrated by Brownstein and Tarr (Brownstein and Tarr, 1979) in the case of solid porous system. These authors studied the problem assuming that the time (t) evolution of magnetization density $\rho(t)$, can be described by the following diffusion equation:

$$\frac{\partial \rho}{\partial t} = D\nabla^2\rho - \theta\rho \;\; M(t) = \int_V \; \rho(r,t) \qquad \text{eq.2.38}$$

where D is the self-diffusion coefficient of water molecules, θ is the parameter accounting for loss in magnetization density occurring in the bulk, M is the total magnetization of the sample (proportional to the NMR signal), r is the position vector, and V is the system volume. Eq2.38 is solved assuming that, initially the magnetization density ρ(r,0) is uniform and equal to $M(0)/V$ and, on the solid surfaces of the system (pores wall), the following boundary condition holds:

$$(Dn \cdot \nabla\rho + \mathcal{M}\rho)|_S = 0 \qquad \text{eq.2.39}$$

where n is the surface normal vector, S is the solid surface (pores wall) and $\mathcal{M}$(legth/time) is an empirical parameter (relaxivity) accounting for the effect of surface on proton relaxations. Chui (Chui et al., 1995) adapted this theoretical approach for gels, building up the so called "Fiber-Cell" model (Fig.2.18). In this theory, the polymeric network is considered as a unique long fiber, of radius R_f, surrounded by an annular region (defined the "pore", in the terminology of Brownstein and Tarr (Brownstein and Tarr, 1979)) of internal radius R_f and external radius R_c. R_c is defined as the distance from the fiber symmetry axis to the cylindrical surface where the gradient of the magnetization density zeroes ($\nabla\rho = 0$) (the cylinder of radius R_c is termed "Cell").

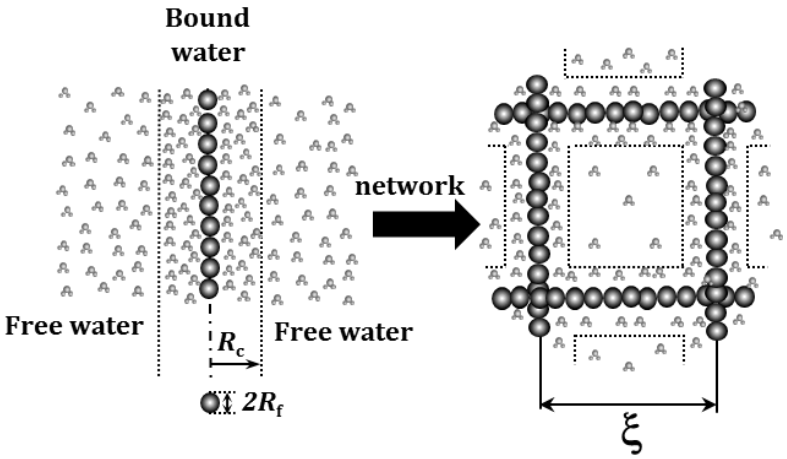

Figure 2.18"Fiber-Cell" model. The relaxation time of protons belonging to water molecules (light grey ensembles) near the polymeric chain surface (bound water) is lower than that competing to free water protons. R_f is the polymeric chain radius (dark grey spheres indicate rigid chain segments), ξ is mesh size while R_c indicates the radial position where the magnetization gradient zeroes.

Accordingly, eq.2.38 is solved applying the condition $\nabla\rho = 0$ in R_c, and the condition expressed by eq.2.39 on the fiber surface, that means in R_f. As polymer gels are diluted systems (polymer volume fraction ϕ ≤ 0.1, it is supposed that the fiber (polymeric chains) content in the "Cell" coincides with ϕ. Accordingly, R_c can be expressed by:

$$\phi = \frac{\pi R_f^2 L}{\pi R_c^2 L} = \left(\frac{R_f}{R_c}\right)^2 \Rightarrow \frac{R_c}{R_f} = \frac{1}{\sqrt{\phi}} \qquad \text{eq.2.40}$$

where L is the total fiber length. On the basis of this frame, the pore hydraulic radius (R_h) can be deduced:

$$R_h = \frac{2V_p}{S} = 2\frac{\pi\left(R_c^2 - R_f^2\right)L}{L2\pi R_f} = R_f\left(\frac{1-\phi}{\phi}\right) \qquad \text{eq.2.41}$$

where V_p is pore volume. The relation between Rh and the polymeric network mesh size (ξ) can be found recalling the Scherer theory (Scherer, 1994), already explained in section 2.1.3.3, eq.2.26. Eqs 2.27 and 2.41 are fundamental for the practical application of the "Fiber-Cell" model. Indeed, Chui (Chui et al., 1995) demonstrated that when the mobility of water molecules, identifiable with D, is high compared to the rate of magnetization loss (identifiable with $\mathcal{M}R_c$; fast-diffusion regime:$\mathcal{M}R_c/D \ll 1$), the following relayion holds:

$$\left\langle\frac{1}{T_2}\right\rangle = \frac{1}{T_{2H2O}} + 2\left\langle\frac{\mathcal{M}}{R_h}\right\rangle = \frac{1}{T_{2H2O}} + 2\frac{\langle\mathcal{M}\rangle}{R_h} \qquad \text{eq.2.42}$$

where $<1/T_2>$ is the average value of the inverse of the relaxation time of the protons belonging to the water molecules trapped within the polymeric network of gel, T_{2H2O} is the relaxation time of the protons of bulk water (i.e. protons of free water, whose relaxation is not affected by the presence of the polymeric chains) and $\langle\mathcal{M}\rangle$ is the $\mathcal{M}$ value averaged on the whole gel volume. In the case of a real polymeric network made up by cubic cells (polymeric mesh) of different dimensions (ξ_i), i.e. of different hydraulic radius R_{hi}, eq.2.42 becomes:

$$\frac{1}{T_{2i}} = \frac{1}{T_{2H2O}} + 2\frac{\mathcal{M}}{R_{hi}} = \frac{1}{T_{2H2O}} + 2\frac{\langle\mathcal{M}\rangle}{R_{hi}} \qquad \text{eq.2.43}$$

where T_{2i} and $\mathcal{M}_i$are, respectively, the relaxation time and the $\mathcal{M}$ value of water protons trapped in cubic cells (polymeric meshes) of size ξ_i (or hydraulic radius R_{hi}). Eq.2.43 is based on the assumption that $\mathcal{M}_i$does not depend on mesh size T_2 and $\mathcal{M}_i = \langle\mathcal{M}\rangle$ for every "i". Thus, knowing R_h (eq.2.41), $<1/T_2>$ (determinable by

eqs.2.34 and 2.35 data fitting) and T_{2H2O}, eq.2.42 allows the determination of $\langle\mathcal{M}\rangle$. In addition, knowing $\langle\mathcal{M}\rangle$ and T_{2i} (see eq.2.34), together with eq.2.43, it is possible evaluating ξ_i for each class of cubic cells. Finally, relying on $\langle\mathcal{M}\rangle$ and $a(T_2)$ (eq.2.34) knowledge, it is possible determining the continuous ξ distribution $a(\xi)$. Indeed, the combination of eqs2.42 and 2.43 allows finding the relation between $d\xi$ and dT_2:

$$\xi = \frac{2\mathcal{M}}{f(\phi)}\Big/\left(\frac{1}{T_2} - \frac{1}{T_{2H2O}}\right) \ldots d\xi = \frac{2\mathcal{M}}{f(\phi)}\left(\frac{T_{2H2O}}{T_{2H2O}-T_2}\right)^2 dT_2 \qquad \text{eq.2.44}$$

Consequently, $a(\xi)$ will be:

$$a(\xi) = \frac{dT_2}{d\xi}a(T_2) \qquad \text{eq.2.45}$$

Thus, the probability $P(\xi)$ of finding a mesh of size ξ inside the polymeric network, is:

$$P(\xi) = \frac{a(\xi)d\xi}{\int_{\xi min}^{\xi max} a(\xi)d\xi} \qquad \text{eq.2.46}$$

2.2.3 The NMR experiment: water self-diffusion coefficient measurement

A second non-invasive application of Low field NMR is the determination of the water self-diffusion coefficient of protonated liquid. The measurable values of the self-diffusion coefficient (D_{H2O}) span, approximately, between $10^{-7}m^2/s^2$ and 10^{-14} m^2/s^2 (Stait-Gardner et al., 2009). In order to perform the measurement of D_{H2O} the "Pulse Gradient Spin Echo" sequence, PGSE, is used. This sequence was developed by Stejskal and Tanner (Stejskal and Tanner, 1965) and, as it can be seen in Fig.2.19, it comprehends two magnetic field gradient of δ duration, spaced by a Δ time length. The gradients allow generating a space-dependent magnetization that "labels" the molecules of protonated liquid and the observation of the magnetization and its evaluation over time lead calculating the liquid molecules self-diffusion coefficient.

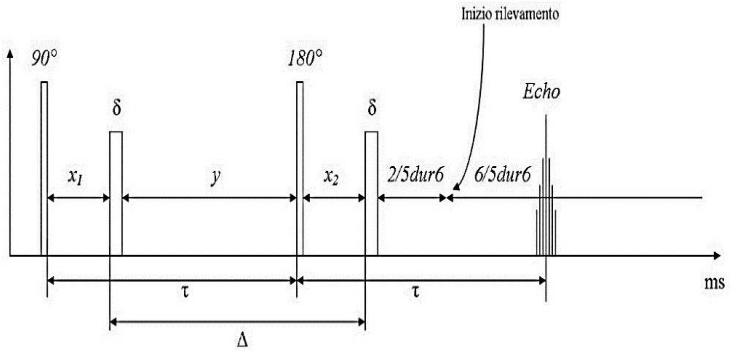

Figure 2.19 PGSE sequence. It is a Hahn Spin-echo sequence where two magnetic field gradient have been added. δ is the gradient duration, while Δ is the lag time between the two

As intensity of a magnetic field is expressed in Tesla (T) and the gradient is measured in Tesla on meter (T/m), the magnetization has no spatial dependence and can be considered only dependent on *z* (Fig 2.20A).

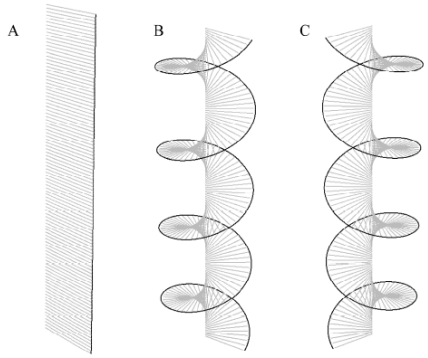

Figure 2.20(**A**): Magnetization after 90° pulse. (**B**): a spatial variation in the magnetization is impressed by the application of a gradient. (C): the impulse to 180° reverses the pitch of the helix.

First gradient operates around *z* axis; therefore its application imparts a specific rotation to signals that are on *xy* plane. If we consider three signals, they share, just before the gradient, the same angle with respect to *y* axis, but occupy different position within the sample. Consequently, they experience a gradient of varying intensity which rotates them of a different amount, and the magnetization will change (Fig 2.20B). The application of 180° pulse induces another rotation and it reverses the magnetization helix pitch (Fig.2.20C). The second gradient reduces helix pitch and it rotates the signals of the same amount imposed by the first gradient. In this way, all signals are realigned with the same angle from *y* axis (as if

there was no gradient), and generate a signal as it happens in the Hahn Spin-echo sequence. Actually, this would be the fate of signal in the case of molecules which cannot move inside the sample. On the contrary, in case of moving (diffusing) molecules, the situation is different: in the time length Δ, molecules spread and so, signals re-alignment is no longer possible. Accordingly, the final echo is attenuated. The knowledge of the attenuation of echoes between a sequence without gradient (Hans Spin-echo) and the one with gradients, allows calculating the self-diffusion coefficient according to the following relation (Antalek, 2002):

$$\ln \frac{A_{G(t)}}{A_{G(0)}} = -\gamma^2 D \delta^2 (t_d) G^2 \qquad \text{eq.2.47}$$

Where $A_{G(t)}$ and $A_{G(0)}$ are the amplitudes of the echoes, respectively, with and without gradient, γ is the gyromagnetic ratio of atoms studied, t_d is the diffusion time (defined as Δ-1/3δ) and G (T/m) is the intensity of the gradient. Since, in eq.2.47, all parameters are known except D, it will be possible to obtain value of the self-diffusion coefficient.

Water self-diffusion measurement is useful to characterize the mobility of water within hydrogel sample. If molecules could freely diffuse the detected D coincide with D_0 (self-diffusion coefficient of free water) and $t_d << a^2/D_0$ (where a is the pore dimension). On the contrary, if $t_d \approx a^2/D_0$, part of water molecules begin to suffer the effect (constraint) of pore walls and D is reduced according to (Stait-Gardner et al., 2009):

$$D_{app}(t_d) = D_0 \left(1 - \frac{4}{9\sqrt{\pi}} \frac{S}{V}\right) (D_0 t_d)^{1/2} \qquad \text{eq.2.48}$$

where $D_{app}(t_d)$ is the apparent self-diffusion coefficient and S/V is the ratio of surface to volume reported to the pore size. If the diffusion time t_d increases up to $t_d >> a^2/D_0$, the maximum distance that molecules travel by diffusion is limited by geometric boundaries of the system and the validity of the equation 2.48 decays. In this situation, the measured value of D is t_d independent and it attains a constant value $D_{app\infty}$ (Latour et al., 1993) equal to D_0/α where α is the tortuosity of network (Stait-Gardner et al., 2009). Interestingly, when pores are not interconnected, $D_{app\infty}$ approaches to zero (this condition corresponds to an infinite tortuosity).

We conclude this long section dedicate to NMR spectroscopy, remembering that we speak about low field NMR for magnetic field comprised in between 0.37 and

2.43 T, while the more traditional high field NMR lying in the interval 7.5T and 37T.

2.3 Release tests

This approach relies on the reduced mobility of a probe molecule inside a polymeric network due to the hindering effect exerted by the chains (Amsden, 1998). Indeed, in the case of negligible convection, network swelling, erosion and probe molecule interaction with polymeric chains (Grassi et al., 2007), probe molecule diffusion is essentially ruled by the chains presence. In particular, in the case of a polymeric network, mesh diameter plays the key role in ruling probe movements. Probe mobility is represented by its diffusion coefficient D_p (dimensionally an areal velocity) that is sometimes referred to as Fickian diffusion coefficient as it is related to movements induced by the presence of probe concentration gradient (Fierro et al., 2011). The relation between D and the mean mesh diameter is given by Peppas and Merryl model (Peppas, and Merrill, 1977):

$$\frac{D_p}{D_0} = \left(1 - \frac{2r_s}{\xi}\right) e^{\left(-y_p \frac{\phi}{1-\phi}\right)} \qquad \text{eq.2.49}$$

that combines the free volume theory (Vrentas et al., 1982) with the assumption that the probably that a solute of radius r_s has to pass through an opening diameter ξ is linearly dependent on the ratio $2*r_s/\xi$. In eq.2.49 D_0 indicates the probe (Fickian) diffusion coefficient in the pure solvent, ϕ is also here the polymer volume fraction in the gel and y_p represents the ratio of critical volume required for a successful translational movement of the probe molecule and the average free volume per molecule of the swelling medium. Although y_p depends on many factors, the authors suggest that, when r_s is expected to be much smaller than ξ, it can be approximately assumed as equal to one. Thus, known D_0, r_s and ϕ, the experimental measurement of D_p allows the determination of ξ according to eq.2.49. The most common way to measure D_p is to experimentally record the release of a probe molecule from a gel matrix. The release curve is then fitted by a mathematical model relying on Fick'law (Grassi et al., 2007):

$$\frac{\partial C}{\partial t} = \nabla\left(D_p \nabla C\right) \qquad \text{eq.2.50}$$

$$V_r C_r(t) = V C_0 - \iiint_V C(X,Y,Z,t)dV \qquad \text{eq.2.51}$$

where t is the time, C is probe concentration in the generic position (X,Y,Z) of the releasing gel matrix of volume V, V_r and C_r are, respectively, the volume and the probe concentration of the release environment, ∇ is the nabla operator and C_0 is the initial and uniform probe concentration in gel matrix. While eq. 2.50 expresses a mass balance on the probe in the micro-scale, eq.2.51 represents a mass balance on macro-scale. Indeed, it states that at each time, the amount of probe in the release environment ($V_\mathrm{r}C_\mathrm{r}$) is equal to the difference between the initial amounts of probe in the gel matrix (VC_0) less the amount still present in gel matrix. Eq.2.50 has to be solved with the following initial boundary conditions:

$$initial\ condition: C(\mathrm{X},\mathrm{Y},\mathrm{Z}) = C_0 \qquad \text{eq.2.52}$$

$$boundary\ conditions: C(gel\ surface) = k_\mathrm{p} C_\mathrm{r} \qquad \text{eq.2.53}$$

where k_p is the probe partition coefficient between the gel and the environmental release fluid. Eq.2.52 sets a uniform concentration in the gel at the beginning (t=0), while eq.2.53 assumes that at the gel release environment interface, the equilibrium condition for what concerns probe concentration holds. In order to determine D_p, eq.2.50 and 2.51 have to be simultaneously solved according to a numerical method (Patankar, 1990) and fitted to the experimental C_r trend, usually assuming k_p=1.

2.4 Transmission Electron Microscope (TEM)

Transmission electron microscopy is a powerful imaging and analysis tool that has been widely used over the world for many decades. TEM operates on the same basic principles as the light microscope but uses electrons (e^-) instead of photons: an electron beam transmits through an ultrathin specimen, interacting with it to form highly magnified images. The high energy electron beam (commonly 80-300 kV, or even up to 1200 kV) creates very short electron wave (below 1 pm) which allows sub-nanometre scale structure to be resolved using magnetic lenses (Ngo and Kuhn, 2016). Indeed, resolution l (the smallest distance between two points

that we can resolve) is defined by the Rayleigh criterion (Spence, 1999): $= \frac{0.61\lambda}{\mu \sin \beta}$, where λ is the wavelength of radiations, μ is the refractive index of the view medium and β is the semi angle of collection of the magnifying lens. As μ and β do not usually vary heavily from sample to sample, the resolution is mainly determined by the wavelength of radiation source. The use of λe^- makes possible to get a resolution a thousand times better than with a light microscope, and the visualization of object in the order of few angstrom (10^{-10}m). The possibility of high magnification has made TEM a valuable tool in medical, biological and material research.

In TEM, (Figure 2.21), a "light source" at the top of the microscope emits the electrons that travel through vacuum in the column of the microscope. Electromagnetic lenses focused electrons into a very thin beam that travels through the specimen. Depending on the density of material, some electrons are scattered and disappear from the beam. At the bottom of microscope, the scattered electrons hit a fluorescent screen, which gives rise to a "shadow image" of the specimen with its different parts displayed in varied darkness according to their density. Obtained image can be studied directly by the operator or photographed with a camera. As it emerges from this description, TEM needs vacuum conditions and ultrathin material. Sample preparation represents major drawbacks of electron microscope analysis method.

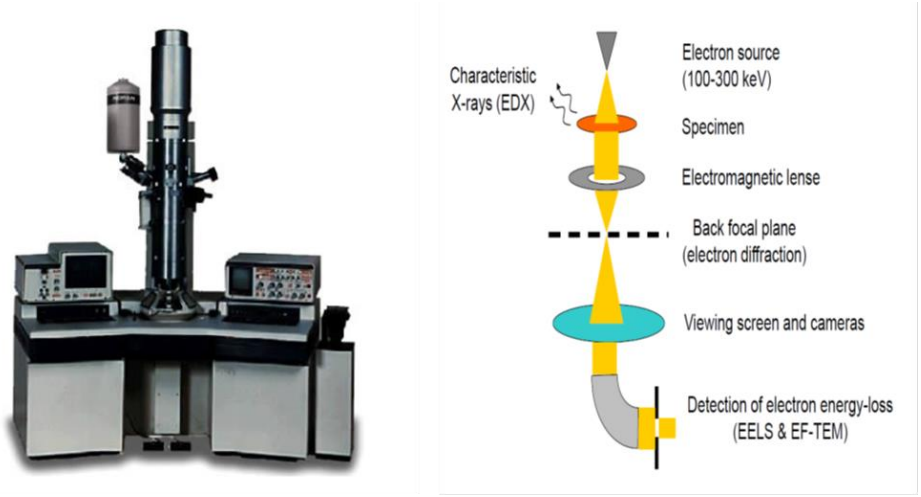

Figure 2.21 TEM (left), schematic structure of microscope (right)

In this thesis, we analyzed hydrogels which contain large quantities of water. Since TEM works in vacuum, the water must be removed. To avoid the gel damaging due to liquid loss, it is possible to preserve polymeric texture with a fixative step in glutaraldehyde (GTA). GTA is a crosslink fixative, which acts through covalent bond with polymeric chains, stabilizing and stiffening hydrogel structure. Than sample is dehydrated and embedded in an epoxy resin that polymerizes into a solid hard plastic block. The block is cut into thin sections by a ultra-microtome. Thin sections are placed on a copper grid and stained with heavy metal. For our gels we used acetate uranyl that produces the highest electron density and image contrast as well as imparting a fine grain to the image due to the atomic weight of 238 of uranium. After staining, the sample slice can be studied under the electron beam. Images were recorded on a Philips EM 208 (100 kV) Transmission Electron Microscope.

2.5 Micro-Computed Tomography (μ-CT)

Feldkamp et al. pioneered μ-CT when they developed an X-ray based micro tomographic system to analyze trabecular samples at a spatial resolution of 50 μm (Feldkamp et al., 2006). Since then, μ-CT has been used extensively in the study of trabecular architecture (Ruegsegger et al., 1996) and there are increasing applications of it in other areas. Its popularity can be attributed to its ability to provide precise quantitative and qualitative information on 3D morphology of the specimen: the interior can be studied in great detail without resorting to physical sectioning and using toxic chemicals. Moreover, after scanning, the intact sample can be subjected to other tests. In this tomography, sample is computed as a series of 2D slice, the X-rays are attenuated and the emergent X-rays with reduced intensities are captured by a detector array. A 2D pixel map is created and its quality depends on the scanning resolution that ranges from 1 to 50 μm (Weiss et al., 2003). Then, data are processed to obtain a 3D reconstruction of the sample. Obviously, the selection of software and hardware influences the efficiency and effectiveness of this radiographically assessment.

In this work, we use μ-CT resorting to the custom made cone-beam system called TOMOLAB. Samples (bones) were positioned on the turn-table of the instrument and acquisitions were performed with the following parameters: distance source-sample (FOD), 80 mm; distance source-detector (FDD), 250 mm; magnification, 3.1×; binning, 2 × 2; resolution, 8 μm; tomography dimensions (pixels), 2004 × 1335; slices dimensions (pixels), 1984 × 1984; number of topographies, 1440; number of slices, 1332; E = 40 kV, I = 200 μA; spot size = 5μm; exposure time, 1.9 s. The slices reconstruction process was achieved by means of commercial software (Cobra Exxim). Input projections and output slices are represented by files (one file per projection and one file per slice) using arrays of 16-bit integers. ImageJ software has been used get a proper segmentation of the slices using Otsu's method (Otsu et al. 1979) and to obtain numerical values of structural features like porosity, interconnection, pore, and trabecular size by means of parallel plate model. (Parfitt et al. 1983). Alternatively, Pore3D software (Brun et al. 2010) has been used on the segmented slices in order to compute the skeleton of the 3D binary image, and to obtain the dimensions of pores and trabeculae as the mean of the maximum spheres centered on the skeleton.

Reference

Amsden B. “Solute diffusion within hydrogels. Mechanisms and models” *Macromol.* 1998 (31):8382-95

Atta-ur-Rahman T. “Nuclear magnetic resonance: basic principles” *Springer-Verlag*, New York, 1986

Atta-ur-Rahman, Choudhary M.I., Atia-tul- Wahab “Solving problems with NMR spectroscopy”, *Academic Press*, Elsevier, 1996

Antalek B. “Using Pulsed Gradient Spin Echo NMR for chemical mixture analysis: how to obtain optimum results” *Concept Magn. Reson.* 2002 (14):225–8

Brazel C.S., Peppas N.A. “Modeling of drug release from swellable polymers”, *Eur. J. Pharm. Biopharm.* 2000 (49):47-58

Brownstein K.R., Tarr C.E. “Importance of classical diffusion in NMR studies of water in biological cells” *Phys. Rew. A* 1979 (19):2446-53

Brun F., Mancini L., Kasae P., Favretto S., Dreossi D., Tromba G. “Pore3D: A software library for quantitative analysis of porous media” *Nucl. Instrum. Methods Phys. A* 2010 (615):326–32

Carr H.Y., Purcell E.M. “Effects of diffusion on free precession in nuclear magnetic resonance experiments” *Phys. Rev.* 1954 (94):630–8

Chui M.M., Phillips R.J., McCarthy M.J. “Measurement of the porous microstructure of hydrogels by nuclear magnetic resonance”. *J. Coll. Inter. Sci.* 1995 (174):336-44

Dalmoro A., Abrami M., Galzerano B., Bochicchio S., Barba AA., Grassi M., Larobina D. “Injectable chitosan/β-glycerophosphate system for sustained release: gelation study, structural investigation, and erosion tests” *Curr. Drug Deliv.* 2017 (14)

Draper N.R., Smith H. “Applied Regression Analysis” *John Wiley & Sons*, New York, USA, 1966

Feldkamp L.A., Goldstein S.A., Parfitt A.M., Jesion G., Kleerekoper M. “The direct examination of three dimensional bone architecture in vitro by computed tomography” *J Bone Miner. Res.* 1989 (4):3-11

Fierro D., Scharnagl N., Emmler T., Boschetti-de-Fierro A., Abetz V. “Experimental determination of self-diffusivities through a polymer network for single components in a mixture” *J. Membr. Sci.* 2011 (384):63-71

Flory P. J. “Principles of polymer chemistry” *Cornell University Press*, 1953

Gallegos D.P., Munn K., Smith D.M., Stermer D.L. “A NMR technique for the analysis of pore structure: application on to materials with well-defined pore structure” *J. Coll. Inter. Sci*. 1987 (119):127-40

Grassi M., “Hydrogels mesh size evaluation” in: Polysaccharide hydrogels: characterization and biomedical applications. *Pan Stanford Publishing*, Singapore, 2015

Grassi M., Grassi G., Lapasin R., Colombo I. “Understanding drug release and absorption mechanisms: a physical and mathematical approach” *CRC Press*, Boca Raton, USA, 2007

Günther H. “NMR spectroscopy: basic principles, concepts, and applications in chemistry” *Wiley*, 1992

Hahn E.L. “Spin echoes” *Phys. Rev.* 1950 (80):580–94

Hore P.J. “Nuclear Magnetic Resonance” *Oxford University Press*, New York, USA, 1995

Ho S.T., Hutmacher D.W. “A comparison of micro CT with other techniques used in the characterization of scaffolds” *Biomat.* 2006 (27):1362-76

Lapasin R., Pricl S. “Rheology of industrial polysaccharides: theory and applications” *Blackie Academic & Professional*, London, GB, 1995

Lapasin R., Pricl S. “Rheology of industrial polysaccharides, theory and applications” *Chapman & Hall*, London, GB, 1995

Latour L.L., P.P. Mitra, Kleinberg R.L.,. Sotak C.H. “Time-dependent diffusion coefficient of fluids in porous media as a probe of surface-to-volume ratio” J. Magn. Res. A 1993 (101):342-6

“Mq Series Manuals” *Bruker Optik GmbH* 2001 Version 1

Ngo D.-T, Kuhn L.T. “In situ transmission electron microscopy for magnetic nanostructures” *Adv. Nat. Sci.: Nanosci. Nanotechnol.* 2016 (7):1-16

Otsu N. “A threshold selection method from gray-level histograms” *IEE Trans. Syst. Man Cybern.* 1979 (9):62-6

Parfitt A.M., Mathews C.H., Villanueva A.R., Kleerekoper M. Frame B, Rao D.S. “Relationships between surface, volume, and thickness of iliac trabecular bone in aging and in osteoporosis. Implications for the microanatomic and cellular mechanisms of bone loss” *J. Clin. Invest.* 1983 (4):1396-409

Patankar S.V. “Numerical heat transfer and fluid flow”*Hemisphere Publishing*, New York, USA, 1990

Peppas N.A., Merrill E.W. “Crosslinked poly(vinyl alcohol) hydrogels as swollen elastic networks” *J. Appl. Polym. Sci.* 1977(21):1763-770

Provencher S.W. “A constrained regularization method for inverting data represented by linear algebraic or integral equations” *Comput. Phys. Comm.* 1982 (27):213-27

Ruegsegger P., Koller B., Muller R. “A microtomographic system for the nondestructive evaluation of bone architecture” *Calcif. Tissue Int.* 1996 (58):24-29

Sarbu T., Styranec T., Beckman E.J. “Non-fluorous polymers with very high solubility in supercritical CO_2 down to low pressures” *Nature* 2000 (405):165-8

Scherer G.W. “Hydraulic radius and mesh size of gels” *J. SolGel Sci. Technol.*, 1994 (1):285-91

Schurz J. “Rheology of polymer solutions of the network type” *Prog. Polym. Sci.*, 1991 (16):1-53

Spence J.C.H “The future of atomic resolution electron microscopy for materials science” *Mat. Sci. Eng. R*. 1999 (26):1-49

Stait-Gardner T., Willis S.A., Yadav N.N, Zheng G., Price W.S “NMR diffusion measurements of complex systems” in diffusion fundamentals III *Leipzig University Press*. (2009):183-204

Stejskal E.O., Tanner J.E. “Spin diffusion measurements: Spin Echoes in the presence of a time-dependent field gradient” *J. Chem. Phys.* 1965 (42): 288-92

Turco G., Donati I., Grassi M., Marchioli G., Lapasin R., Paoletti S. “Mechanical spectroscopy and relaxometry on alginate hydrogels: a comparative analysis for structural characterization and network mesh size determination” *Biomacromol.* 2011 (12):1272-82

Vanhamme L., Sundin T., Hecke P.V., Huffel S.V. “MR spectroscopy quantitation: a review of time-domain methods” *NMR Biomed*. 2001(14):233-46

Vrentas J.S., Duda J.L., Ju S.T., Liu H.T. “Prediction of diffusion coefficients for polymer-solvent systems”. *AIChe J.* 1982 (28):279-85

Wang X., Ni Q.J. “Determination of cortical bone porosity and pore size distribution using low field pulsed NMR approach”. *J. Orthop. Res.* 2003 (21):312-19

Weiss P., Obadia L., Magne D., Bourges X., Rau C., Weikamp T., Khairoun I., Bouler J.M., Chappard D., Gauthier O., and Daculsi G. “Synchrotron X-ray microtomography (on a micron scale) provides three dimensional imaging representation of bone ingrowth in calcium phosphate biomaterials” *Biomat.* 2003 (24):4591-601

Whittal K.P., MacKay A.L. “Quantitative interpretation of NMR relaxation data” *J. Magn. Reson*. 1989 (84):134-52

3 Biomedical Hydrogel characterization

This chapter is dedicated to four different hydrogels with potential application in the biomedical field. All of them are studied by different techniques in order to understand the complex structure of their polymeric networks. In particular, rheology and LF-NMR techniques will be considered while other techniques will be used to confirm our findings and data interpretation.

This chapter is divided in two main sections: the first considers the study of sol-gel transition of two hydrogels made up of, respectively, chitosan and nano-cellulose, while the second part is mainly focalized on the mesh size evaluation of two hydrogels (one consisting of PEG and the other of PVP) designed for drug delivery.

The experimental data interpretation of both sections will be performed in the light of the theories developed in chapter 2. Indeed, my aim is to stress the great potentiality of LF-NMR and Rheology in the characterization of hydrogels structure.

3.1 Investigation on sol-gel transition

3.1.1 Temperature effect on the structuration of a thermo-sensitive hydrogel based on chitosan/β-glycerolphosphate.

3.1.1.1 Introduction: injectable hydrogel

In recent years, controlled drug delivery systems based on hydrogel have been highlighted as therapeutic carriers to deliver drugs at targeted sites within a specific time frame (Singh and Lee, 2014). Certainly, the possibility of controlling the release rate, the site of action and the duration of drug release is very

important as it minimizes possible side effects. Obviously, also the choice of the administration route (oral, ocular, transdermal and subcutaneous, for instance) entails not negligible consequences. For this reason, in hydrogel-based technology, one of the major goals is the development of injectable hydrogels, also called *in-situ* forming hydrogels (Li et al., 2011). Accordingly, before administration, the future hydrogel (gel precursor) resembles a clear polymer solution that turns into a viscoelastic system (gel) in response to change in external stimuli. Gel precursors can gel under mild conditions, due to physical changes like pH value, temperature, ionic concentration (Huynh et al., 2011) and/or chemical reactions, like Michael addition (Jin et al., 2010), Schiff base (Tan et al., 2009), enzymes and so on. Generally, temperature is the easiest stimulus to manipulate in these environmentally responsive hydrogels. The advantages of using injectable hydrogels rely on their high moldability, possibility of in vivo delivery in a minimally invasive way (resulting in a faster recovery, smaller scar size and less pain for patients), and capacity of easily and effectively cells and/or drugs encapsulating. For instance, drugs, bioactive molecules or cells can be encapsulated with aqueous polymer solutions at low temperature, and the resulting solutions/dispersions can rapidly form hydrogels after injection into the body (Li et al., 2011).

In this field, chitosan-based hydrogels have gained increasing interest as novel and safe delivery systems. Injectable chitosan-based gels have been already employed for drug delivery, tissue bone engineering and cartilages repair (Ruel-Gariépy et al., 2004). Chitosan, (CS) structurally similar to glycosaminoglycans, is produced by de-acetylation of chitin, a derivative of glucose, and is comprised of glucosamine and acetyl-glucosamine units (Figure 3.1). Chitosan has excellent biocompatibility, low toxicity and immunostimulatory activities (Souza et al., 2009).

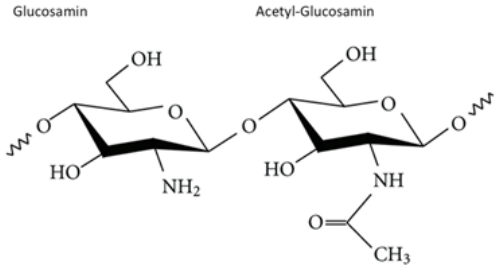

Figure 3.1 Schematic representation of the two different chitosan repeating units.

Beyond this quality, it is a cationic biopolymer and, thus, soluble only in aqueous acid media (at pH ≤ 6.5) where the free amino groups of the chitosan are protonated. This drawback is overcome, neutralizing chitosan charges with addition of salt β-glycerolphosphate (β-GP). This salt (β-GP) allows maintaining chitosan soluble near neutral pH and allows the sol-gel transition upon heating. Probably, heating induces proton transfer from chitosan to glycerol phosphate, thereby neutralizing chitosan and allowing attractive inter-chain forces to form a physical gel (Lavertu et al., 2007). Accordingly, CS/β-GP represents a very intriguing thermosensitive hydrogel. The literature on CS/β-GP is quite broad and it diversifies into two branches: the first aims to unveil the mechanisms of sol-gel transition (Filion et al., 2007), while the second, regardless of the underlying mechanism, analyses the effect of the initial variables (Dalmoro et al., 2017) on the gelation temperature. On the contrary, this work is mainly focused on a less discussed topic, i.e., the effect of temperature on the system final structural properties. Depending on the final aim of the CS/β-GP system, the considered temperature can be different and, consequently, also gel mechanical characteristics can be different. The combined use of NMR and rheology offers an innovative approach for studying the thermo-gelation process.
In the light of biomedical applications of CS/β-GP as drug delivery system, one of the studied temperature is 37°C. Moreover, release test about vitamin B12 will be considered.

3.1.1.2 Materials

Chitosan (medium molecular weight, 76% deacetylated, viscosity 428 cPs, CAS n. 9012-76-4), β-glycerolphosphate disodium salt hydrate (≤1.0 mol % L-α-isomer, ≤0.1% inorganic phosphorus, molecular weight 216.04, CAS n. 154804-51-0) and acetic acid (CAS n. 64-19-7) were purchased from Sigma-Aldrich s.r.l. (Milan, Italy) and used without further purification. B12 vitamin (CAS n. 68-19-9) was used as model drug while hydrochloric acid, sodium hydroxide (CAS n. 1310-73-2) and potassium di-hydrogen phosphate (CAS n. 7778-77-0) were used to prepare the

buffer solution (pH 7.4) used in erosion and dissolution tests. All these listed products were purchased from Sigma Aldrich s.r.l., Milano Italy.

3.1.1.3 Preparation of thermo-sensitive chitosan hydrogel

For thermosensitive chitosan hydrogel formation, chitosan and β-GP aqueous solutions were separately prepared and then mixed together. Based on previously experimental results (Dalmoro et al., 2017), the optimized composition present a molar ratio βGP/CS=2.11 and molar ratio AcOH/CS=0.48 and a molar concentration [CS]=0.087 M.

For LF-NMR and rheological experiments, CS solution was prepared dissolving 2 g of polymer in 100 ml of an acetic acid solution at 0.48 molar ratio AcOH/CS. The solution was mixed over night at ambient temperature and then filtered under vacuum. Due to CS lost during filtration, the actual CS weight percentage was determined by weighing a portion of the filtered solution before and after drying. β-GP solution was prepared dissolving a given amount of β-GP into a volume of water such that when the two solutions were mixed together I had: i) the final β-GP/CS mole ratio equal to 2.11; ii) the final molar concentration of CS monomer equal to 0.087 M (about 1.5%w/w). The β-GP solution was then added drop wise to the chitosan solution under rapid stirring, maintaining the temperature at 4°C. The final solution was stored at 4°C for 24 h before testing.

For drug release test, vitamin B12 was added on the CS solution just before mixing with β-GP solution. The molar ratio of B12/CS was always set to 0.0126 (i.e., B12/CS mass ratio of 10%w/w). The final solution was stored at 4°C for 24 h before producing gelled thin films by controlled heating.

3.1.1.4 Results and discussion: I part

Preventively, the effect of the β-GP (fundamental player for the gelation process) was evaluated. At this purpose, a rheological temperature sweep (1Hz, τ = 1 Pa, heating speed = 0.02 °C/s) test were performed on the simple chitosan solution and on the CS/β-GP solution. The temperature range considered spanned from 15 to 47°C (figure 3.2).

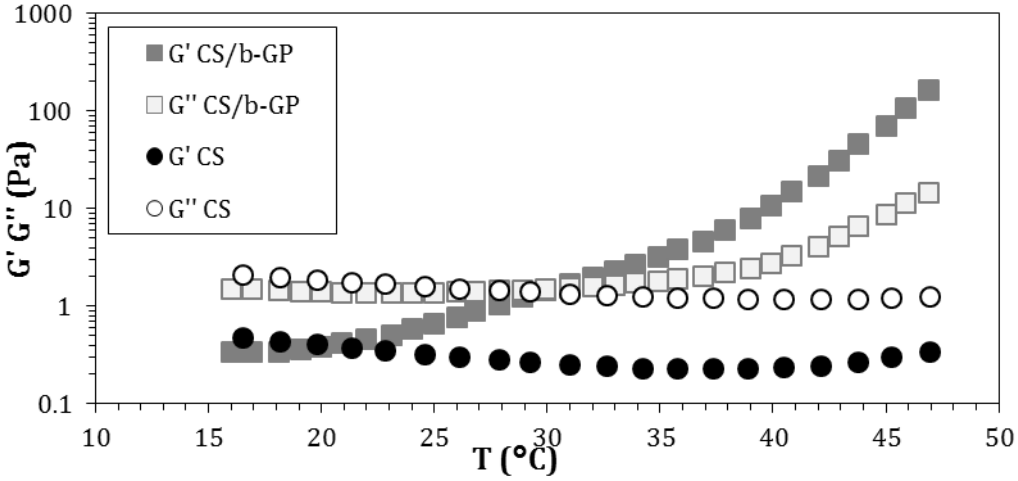

Figure 3.2 Temperature Sweep on sample CS/β-GP (squares) and plain solution CS (circles).

Results clearly indicate how only the presence of β-GP allows the transition from solution to gel. Indeed for the CS solution, along all temperature range, G'' are bigger than G' with almost constant values, this being the typical behavior of solution. On the contrary, in the CS/β-GP system the temperature increase leads to a crossover of G' and G'' around 30°C. From now on, the sample starts exhibiting marked elastic properties this witnessing the formation of a three-dimensional polymeric network. The crossover was confirmed by successive time sweep tests where the temperature is immediately raised from 10°C to a higher constant value. The evolution of the rheological properties of CS/β-GP was monitored for 1 hour at several temperature: 20, 25, 27, 30, 37, 45 and 47 (1Hz, τ = 1 Pa). For the sake of clarity, only G' values were reported in Figure 3.3.

It is interesting to notice that while the G'-G'' crossover occurred at every temperature, the gelation process kinetic was improved by temperature increase. In particular, T = 30°C represents a sort of threshold for the gelation process. Indeed the G' time evolutions can be grouped in two classes, i.e. below and above 30°C (Figure 3.3).

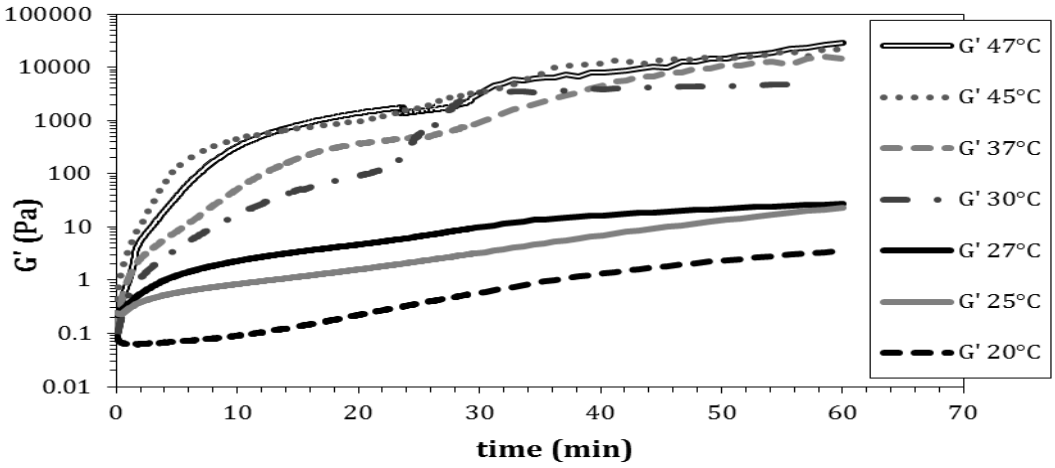

Figure 3.3 Time Sweep: evolution of G' in CS/β-GP at different temperatures.

This behavior is confirmed by the frequency sweep tests (τ = 1 Pa) performed immediately after the time sweep test (Figures 3.4and 3.5).

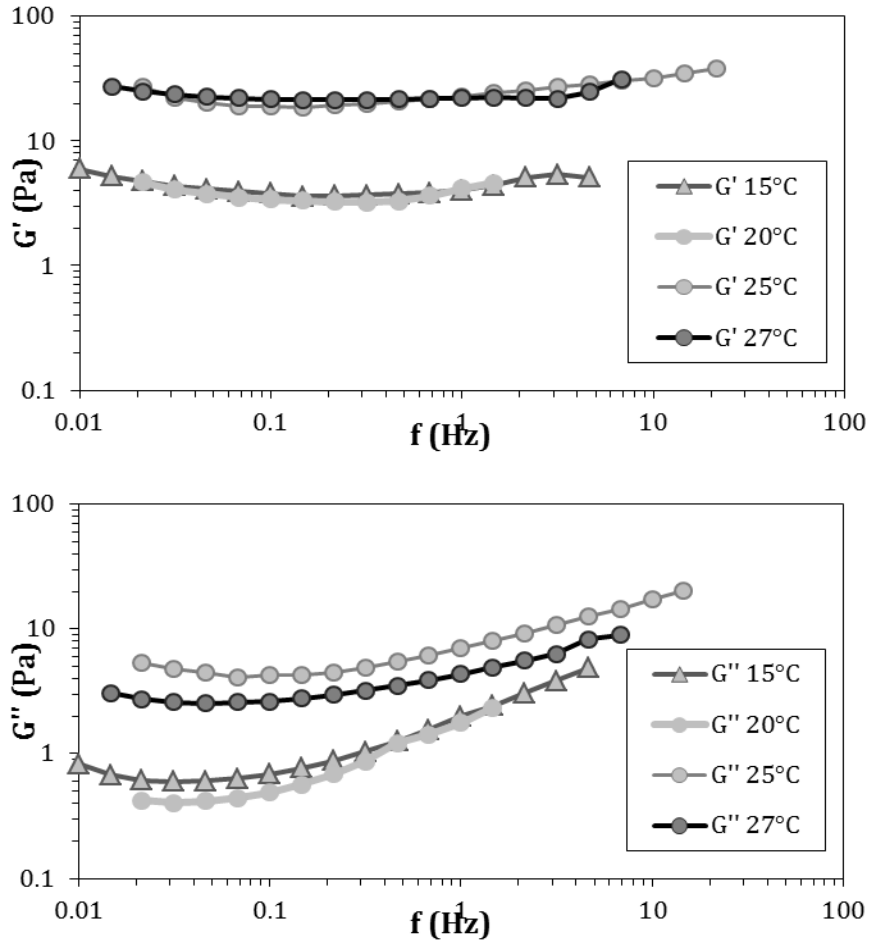

Figure 3.4 Mechanical spectra for CS/β-GP at different temperature below 30°C; elastic and loss moduli (*G'* and *G''*) are reported, respectively, at the top and at the bottom.

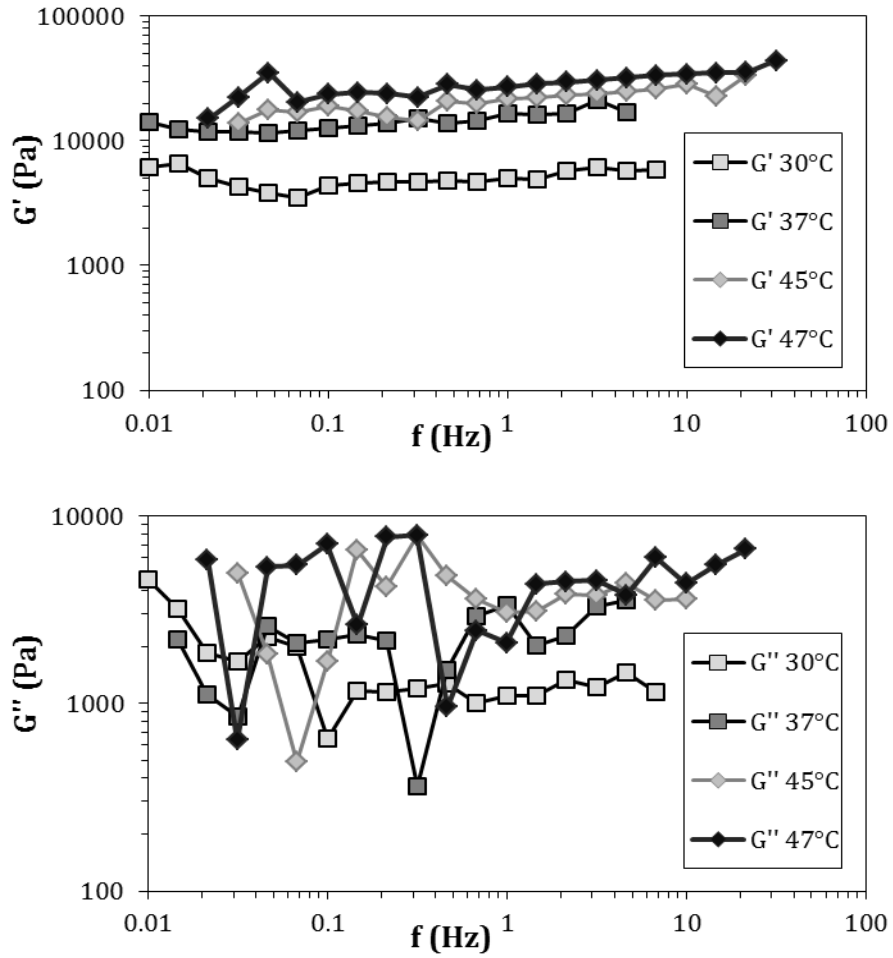

Figure 3.5 Mechanical spectra for CS/β-GP at different temperature ≥ 30°. Elastic and loss moduli (*G'* and *G''*) are reported, respectively, at the top and at the bottom.

Similarly to what performed for the rheological characterization, also for LF-NMR, time sweep tests were conducted to record the time dependence of the average relaxation time, T_{2m}, of CS/β-GP systems. This implied measuring, for each temperature, sample relaxation at different times (about 50 time points). Then, eq.2.34 was fitted to each relaxation curve in order to get the temporal trend of T_{2m} and of the relaxation spectrum (A_i, T_{2i}).

In order to evaluate the effect of the crosslinking agent (β–GP), the first test consisted in comparing the T_{2m} temporal trend heating to 37°C one system with β–GP and an identical system differing only for the absence of βGP as shown in Figure 3.6.

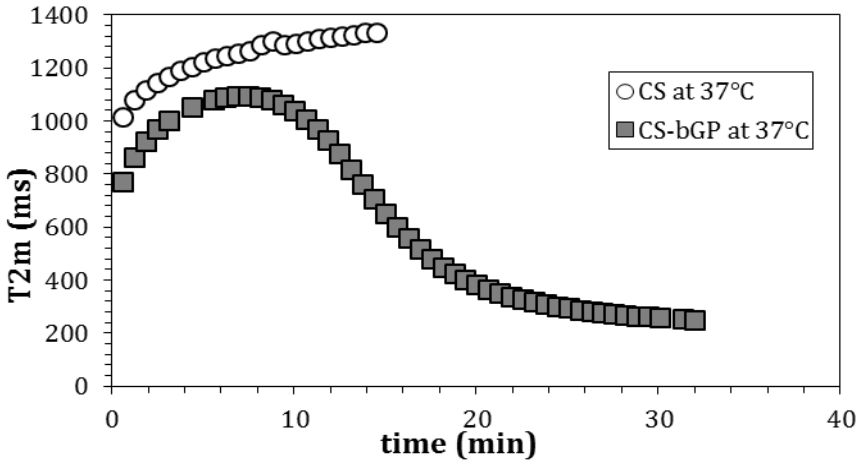

Figure 3.6 Temporal trend of the average relaxation time (T_{2m}) referring to a system containing the crosslinking agent (β-GP) (black squares) and an identical system lacking β-GP (oper circles). Heating temperature is 37°C.

It is clear that when the crosslinking reaction does not occur (open symbols), T_{2m} increases simply because of system heating from 4°C to 37°C (notoriously, heating implies the increase of the water ^{1}H relaxation time (Brownstein and Tarr, 1979)). On the contrary, when β-GP is present and induces the crosslinking reactions, a completely different T_{2m} behavior takes place (closed symbols). Indeed, after an initial increase, a following decrease takes place. The initial increase indicates that heating is the predominant mechanism affecting T_{2m} even if the small effect of the crosslinking reactions is witnessed by lower T_{2m} values in comparison to those of the system lacking β-GP. The following T_{2m} decrease is the clear evidence of the predominant role played by polymeric chains crosslinking on the T_{2m} trend. Thus, the T_{2m} time evolution is the result of two counteracting phenomena: one is connected to system heating that induces T_{2m} increase, while the second is due to the formation of a three-dimensional network that entraps water molecules in nano-sized meshes. As a matter of fact, the formation of a three-dimensional network implies the T_{2m} reduction as polymeric chains are obliged to rearrange in a different topological organization with respect to that of the starting solution. This, in turn, reflects in an increase of the area of the water-polymer chains interface that is the real reason for T_{2m} decrease as discussed in chapter 2. Thus, while, at the beginning, water heating dominates water ^{1}H relaxation behavior,

then, the formation of a three-dimensional network becomes the most important phenomenon for what concerns the water protons relaxation characteristics.

In order to evaluate the effect of the heating temperature on these counteracting phenomenas, different temperatures were considered. In particular, the following temperatures were considered: 15, 20, 25, 27, 30, 33, 37, 40, 45, 47°C (see Figure 3.7). Every temperature entails an initial increase of T_{2m}, due to sample heating, as the effect of the crosslinking process is still negligible. From 22°C on, this initial growth is followed by a differently pronounced decrease of T_{2m}, as the effects of crosslinking process is no longer negligible.

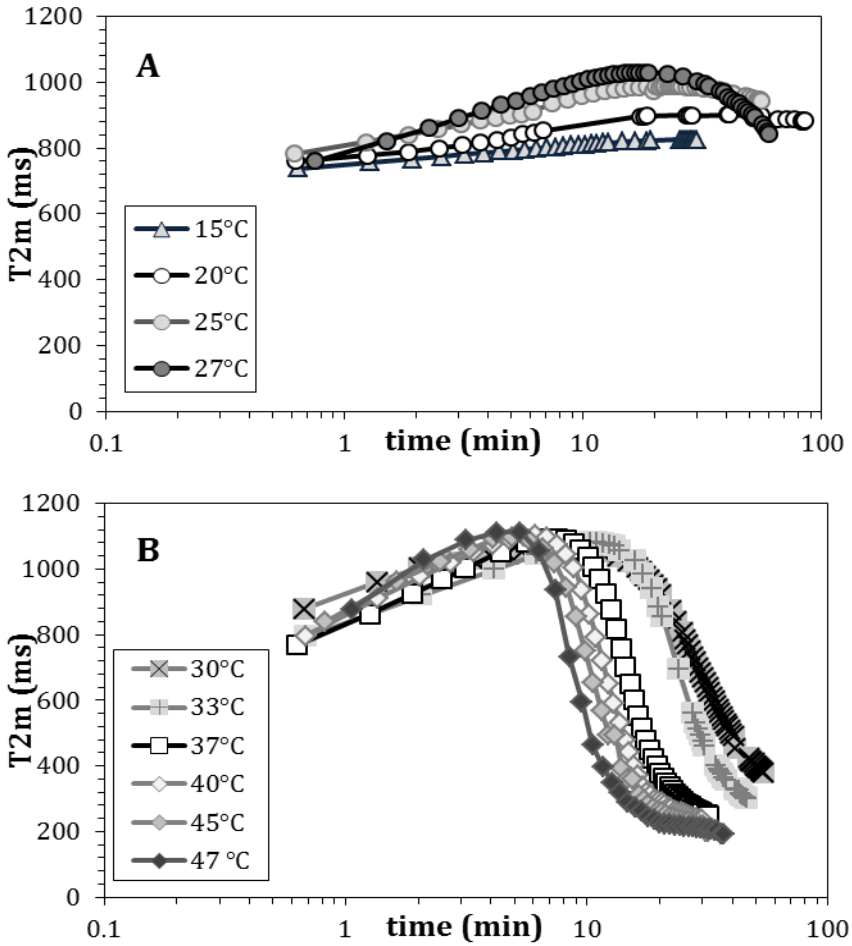

Figure 3.7 (**A**)Temporal evolution of relaxation time, T_{2m}, for CS/β-GP systems at different temperature below 30°C. (**B**) Temporal evolution of relaxation time, T_{2m}, for CS/β-GP systems at different temperature ≥30°C.

In particular, the kinetic of T_{2m} reduction is improved by temperature increase as clearly shown in figure 3.7A-B. At 15°C and 20°C, T_{2m} reduction is not detectable as

the effect of the crosslinking reactions is always negligible in comparison to system heating.

As also seen in the rheological characterization, T_{2m} trends can be split in two different groups: below and above 30°C. Up to 27°C T_{2m} decrease is slow, while it becomes much more pronounced from 30°C on and the sharpness of T_{2m} drop increases with temperature rising. Interestingly, above 30°C, the final value reached by T_{2m} is similar for all systems and this witnesses the existence of similar three-dimensional structures. This result confirms the rheological findings about G' temporal evolution. Indeed, not only similar final G' values were detected for T≥30°C, but these values were higher than those pertaining to lower temperature (see Figure 3.5). Accordingly, an inverse proportionality exists, in this case, between T_{2m} and G' time evolution, this being reasonable in the light of what discussed in chapter 2 about rheology and LF-NMR. In general, when dangling chains do not exist in the network (or their fraction is negligible), this inverse proportionality holds. This is not always the case in the opposite situation (Chiarappa et al., 2017). In order to make more evident the relation between magnetic and mechanical properties, Figure 3.8 shows the variation of the final values (i.e. values recorded when no further system variations occurred (about 1 h)) of G', evaluated at 1 Hz, and T_{2m} corresponding to systems heated at different temperatures.

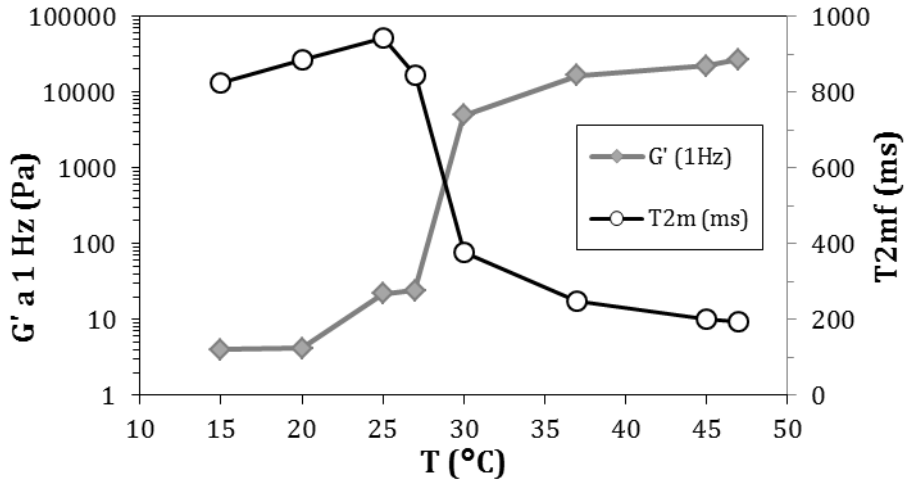

Figure 3.8 Elastic modulus G'(at 1 Hz) and mean relaxation time T_{2m} dependence on the heating temperature T. G' and T_{2m} are determined after about 1 h when no further system changes were observable.

It is clear that starting from 25°C, T_{2m} decrease correspond to G' increase and that both G' and T_{2m} do not considerably vary for T≥30°C.

Interestingly, eq.2.34 fitting to experimental data highlights, for T<30°C, the presence of only one relaxation time (T_{21}=T_{2m}) in the entire T_{2m} time evolution (Fig. 3.9A), whereas for T≥30°C, two relaxation times appear (T_{21} and T_{22}) in the T_{2m} drop phase (Figure 3.9B). It can be argued that the gelling process implies the temporal formation of two pseudo-phases, one richer in polymer and the other poorer in polymer. More precisely, it could be supposed that the different relaxation times do not only depend on polymer concentration but also on polymeric chains three-dimensional organization. Accordingly, the richer polymer phase could be thought as gel-buds where the gelation process is more developed (lower relaxation time T_{22}) than in the other pseudo-phase, characterized by a higher relaxation time (T_{21}).

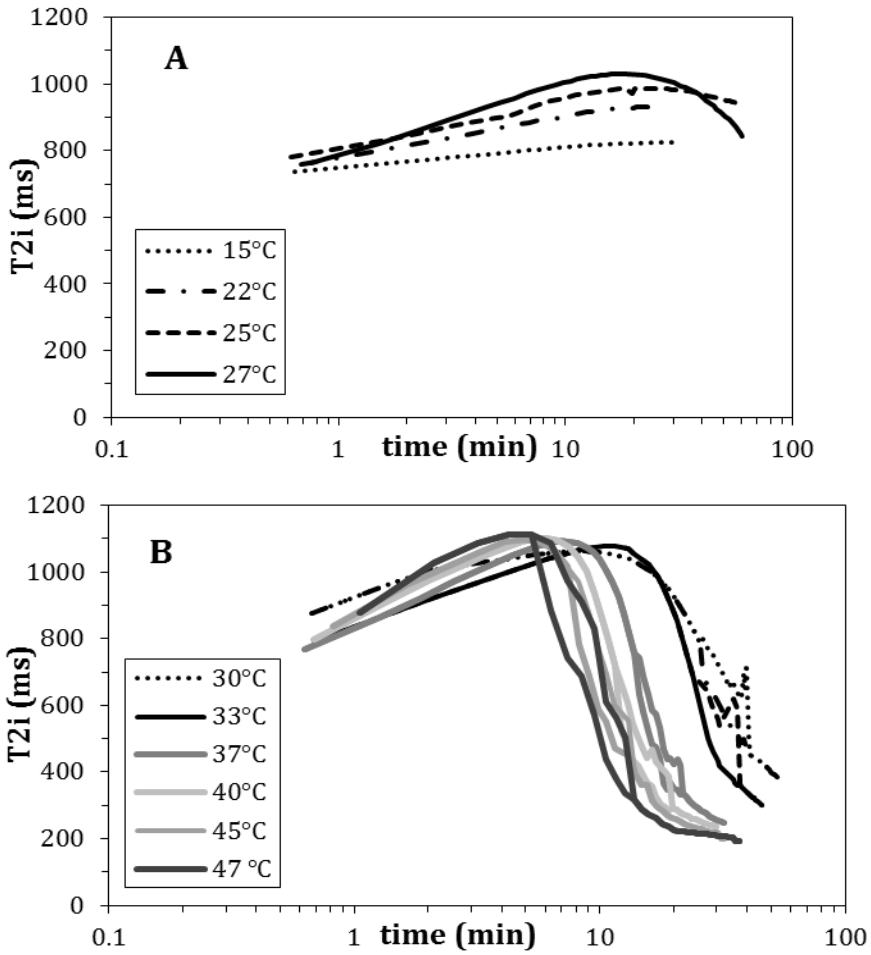

Figure 3.9 Temporal evolution of relaxation time components, T_{2i}, for CS/β-GP systems at different temperature: (**A**) below 30°; (**B**) above 30 °C

During time, buds grow up and their volume increase to the detriment of the other pseudo-phase that, at the end, disappears. Thus, finally, the system comes back to a homogenous condition so that only one relaxation time is detectable. This interpretation is supported by the temporarily trend of the volumetric factions (A_i) associated to the bud phase (A_{22}, T_{22}) and to the other phase (A_{21}, T_{21}). Indeed, while A_{22} increases with time, A_{21} decreases as shown in Figures 3.10A-B in the case of a heating temperature of 37°C (similar results occur provided that T≥30°C):

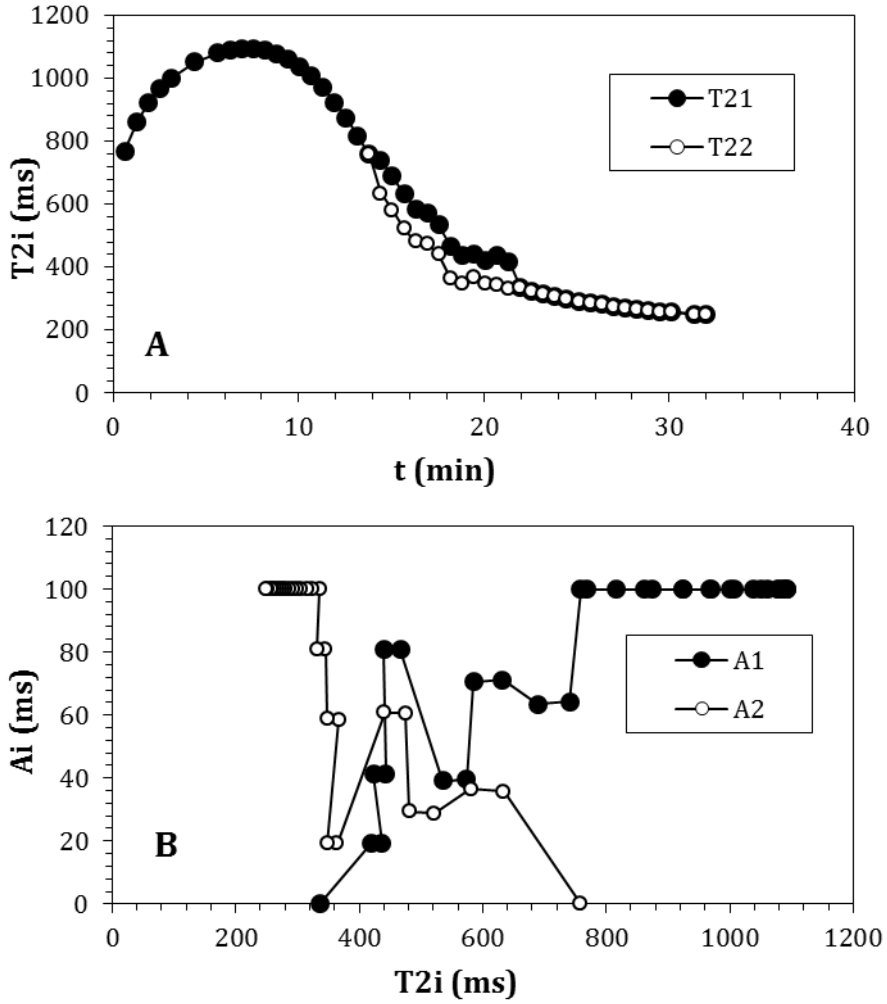

Figure 3.10 (**A**) Temporal evolution of the two relaxation times (T_{21}, T_{22} – bud phase) when heating temperature is 37°C. (**B**) Temporal evolution of the relaxation spectrum (A_1-T_{21}; A_2-T_{22} bud phase) corresponding to the window appearing in A. Times elapses from right to left.

The presence of two relaxation times (T_{21}, T_{22}) opens a "window" in the T_2 trend shown in Figure 3.10A. The relaxation spectrum of both pseudo-phases (A_1-T_{21}; A_2-T_{22} bud phase) are reported in Figure 3.10B, where time elapses from right (higher

relaxation times) to left (lower relaxation times). As for heating temperatures <30°C the "bud-phenomenon" does not occur, it can be supposed that its occurrence is mandatory for the formation of a strong hydrogel relaying on CS/β-GP systems.

The theoretical approach presented in chapter 2, devoted to the estimation of gel mesh size resorting to rheology and LF-NMR, can be used to evaluate how the crosslinking reaction affects the mesh size of the forming three-dimensional polymeric network. For what concerns the rheological approach, the main assumption is that the value of the elastic modulus (G') essentially represents the shear modulus (G) of the forming gel. Obviously, this is substantially true only when G' is much higher (about ten times) than the loss modulus G'' and, in the case of our pivot gel (that heated at 37°C), this takes place after about 8 minutes heating (see Figure 3.3). On the basis of this assumption, eq.2.12 and eq.2.22 allow the estimation of the time evolution of the gel mesh size (ξ_{Rheo}) as shown in Figure 3.11.

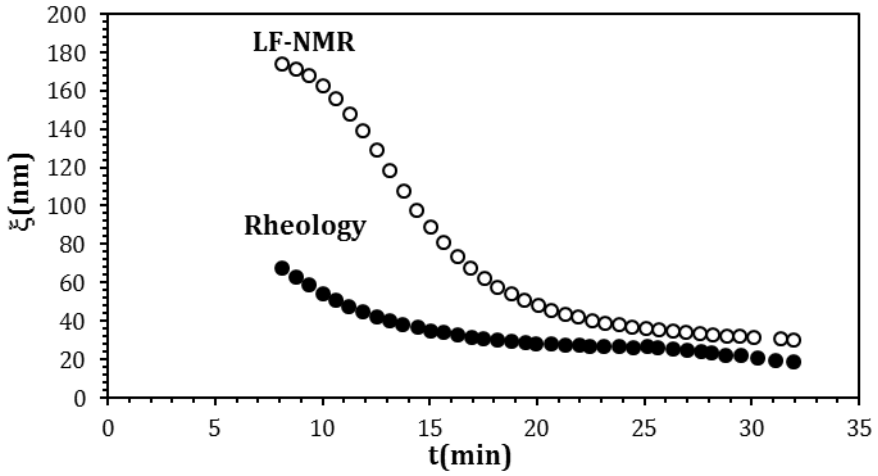

Figure 3.11 Temporal evolution of the gel mesh size according to the rheological approach (ξ_{Rheo}) and the LF-NMR ($\xi_{LF\text{-}NMR}$) approach presented in chapter 2. Data refers to the gel heated at 37°C. t is the time elapsed from the beginning of the crosslinking reaction.

In the case of the LF-NMR approach, the main assumption is that a real gel network occurs only after the maximum exhibited by the average relaxation time (T_{2m}) as shown, for example, in Figure 3.10. Indeed, as above discussed, before the maximum, the variation of T_{2m} is mainly due to system heating and only, then, the

effect of the developing three-dimensional network on T_{2m} becomes relevant. In the case of our pivot system (that heated at 37°C), this condition takes place after around 8 minutes since the beginning of the crosslinking reactions (see Figure 3.10). The strategy adopted to evaluate the mesh size evolution according to LF-NMR ($\xi_{LF\text{-}NMR}$) relies on eq.2.26 and eq.2.42. Indeed, assuming that the gel is completely formed after 32 min (Figure 3.10), eq.2.26 and eq.2.42 allows the valuation of the relaxivity $\langle\mathcal{M}\rangle$:

$$\langle\mathcal{M}\rangle = \left(\left\langle\frac{1}{T_2}\right\rangle - \frac{1}{T_{2H2O}}\right)\frac{R_f}{2}\left(\frac{1-0.58\varphi}{\varphi}\right) \qquad \text{eq.3.1}$$

Knowing that for our pivot system $R_f \approx 1$ nm (monomer size have been estimated by structural data (Mazeau et al., 1994)), $1/T_2 = 4\ s^{-1}$, T_{2H2O} (37°C) = 3.694 s and ϕ = 0.0104, it follows $\langle\mathcal{M}\rangle = 1.79*10^{-7}$ m/s. Accordingly, the fast diffusion conditions are met as the parameter $\mathcal{M}R_c/D = 5.79*10^{-7} << 1$. Thus, only one relaxation time is needed to identify a mesh of dimension ξ. Interestingly, this relaxivity value resembles what found in low concentration scleroglucan–borax and guar gum–borax hydrogels (0.7% w/v), (Coviello et al., 2013). Relaying on the knowledge of the relaxivity, it is possible establishing a connection between the mesh size and the relaxation time T_2 (the experimental datum) by a simple mathematical manipulation of eq.2.26 and eq.2.42:

$$\xi = 2\langle\mathcal{M}\rangle\left(\frac{\varphi}{1-0.58\varphi}\right)\sqrt{\frac{1-\varphi}{\varphi}\frac{C_1}{C_0}}\Big/\left(\left\langle\frac{1}{T_2}\right\rangle - \frac{1}{T_{2H2O}}\right) \qquad \text{eq.3.2}$$

The results of eq.3.2 are depicted in Figure 3.11 and compared with the outcomes deriving from the rheological approach. It can be seen that the two approaches converge to very similar results only when the gel is almost completely developed. This is not surprising in the light of the different heating kinetics of the sample. Indeed, while both in the rheological and LF-NMR characterisation sample volume is approximately the same (≈ 1 cm^3), the "rheological" heating surface is about 2 times that of the LF-NMR. In addition, while in the rheological case the sample is in direct contact with the heating surface (the inferior sensor plate), in the LF-NMR situation, a glass wall, constituting the sample holder, of about 0.5 mm separates the sample from the heating source. Thus, it seems reasonable that the faster

rheological heating reflects in more rapid gelation kinetics with respect to the LF-NMR case.

The LF-NMR approach for the evaluation of the mesh size, can be also applied to the "window" zone where two relaxation times are needed to describe the water ^{1}H relaxation behaviour (Figure 3.10A). Indeed, in eq.3.2 it is sufficient substituting the average value of $1/T_2$ by $1/T_{21}$ and $1/T_{22}$ corresponding to the two pseudo-phases constituting the "window" (see Figure 3.10). The result, depicted in figure 3.12, allows saying that the two pseudo-phases can be interpreted as two gel zones characterised by different mesh size. That characterised by the smaller mesh size, previously labelled as "buds", will give origin to final network while the other one will disappear.

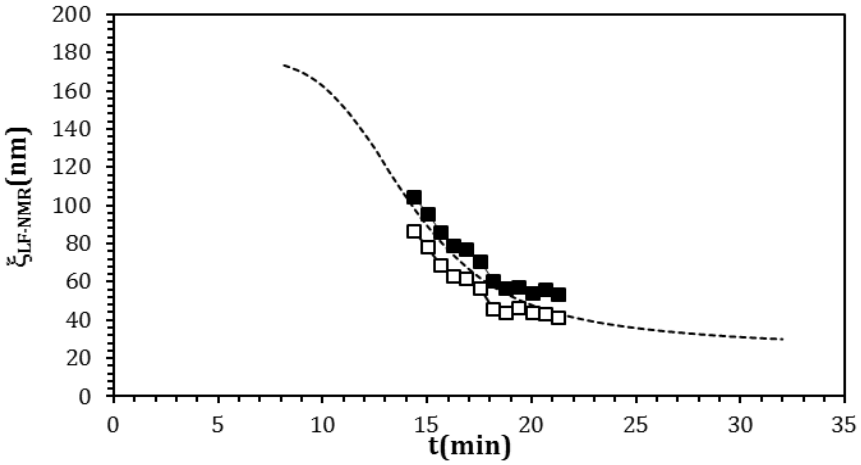

Figure 3.12 Temporal evolution of the gel mesh size inside the "window" depicted in Figure 3.10 according to the LF-NMR approach ($\xi_{LF\text{-}NMR}$). Open and close squares indicate, respectively, the bud and the other phase. The dashed thin line indicates the trend of the average mesh size $\xi_{LF\text{-}NMR}$.

In conclusion, I can say that the combination of rheology and LF-NMR allowed formulating a hypothesis about the gelling kinetics of CS/β-GP systems in response to different heating temperatures. This aspect could be very important in the light of final applications that imply an *in situ* gel formation. Indeed, although the *G'*-*G''* crossover takes place at every temperature (among those considered), when T<30°C, the gel final properties could be too weak to guarantee the minimal gel residence time at the site of action. However, for T<30°C, the system guarantees an easy injection because its rheological properties are closer to that of a liquid than to that of a solid material.

3.1.1.5 Results and discussion: II part

This second part is dedicated to a deeper characterization of CS/β-GP heated at 37°C as this temperature is the most interesting in the light of biomedical applications.

For what concerns rheology, CS/β-GP system underwent a time sweep test at 37°C for one hour immediately followed by a frequency sweep test (figure 3.13A-B). From the mechanical spectra clearly emerges the gel like nature of this system where not only G' largely exceeds G'' but also G' and G'' are almost frequency independent.

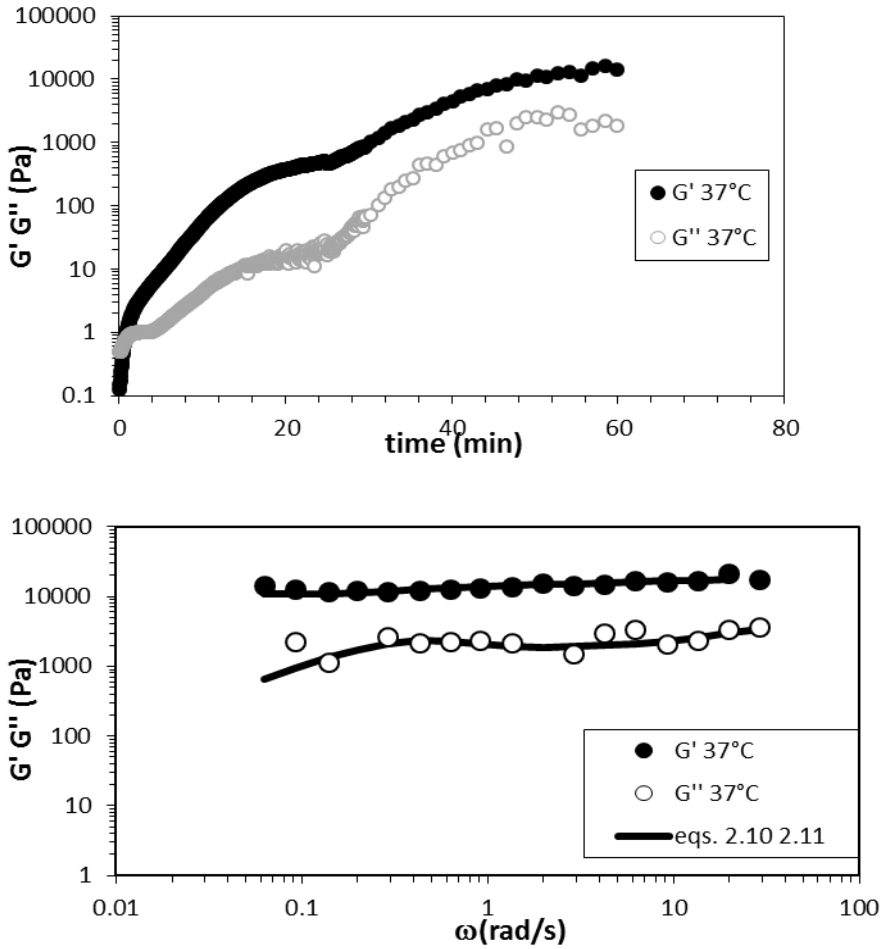

Figure 3.13 rheological characterizations for CS/β-GP system at 37°C with (**A**) time sweep test and (**B**) frequency sweep test, where G' and G'' indicate, respectively, the storage and loss moduli and continuous lines represent eqs. 2.10 and 2.11 best fitting.

Experimental mechanical spectra were fitted by the generalized Maxwell's model (section 2.1.3.1-2) and the fitting results are shown in Figure 3.14. As G_i are

substantially independent on λ_i, the mechanical relaxation spectrum is typical of strong gels. The statistical reliability of the fitting is proved by the Ftest (4,27,0.95<40)

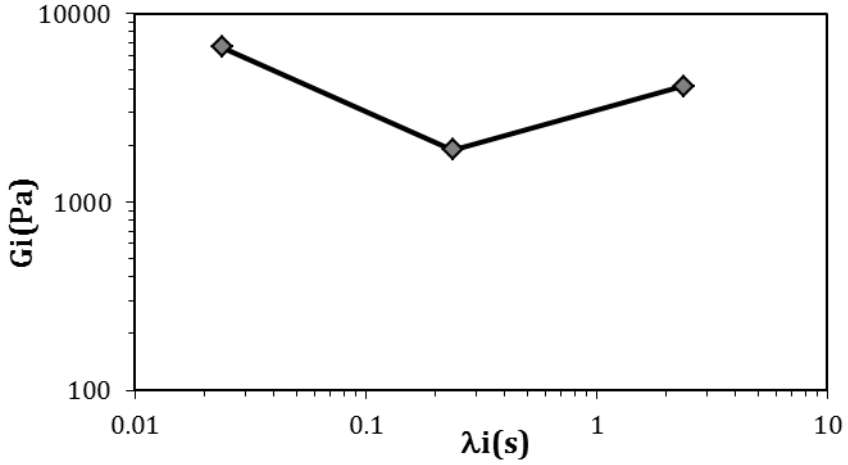

Figure 3.14 Fitting resulats of Maxwell's model where *Gi* elements are reported related to relaxation times λi.

The rheological characterization was followed by the LF-NMR one with particular to the determination of the continuous mesh size distribution according to eq.2.35. Figure 3.15 shows eq.2.35 best fitting (*I(t)*, dashed line) to experimental relaxation data I_s (open circles).

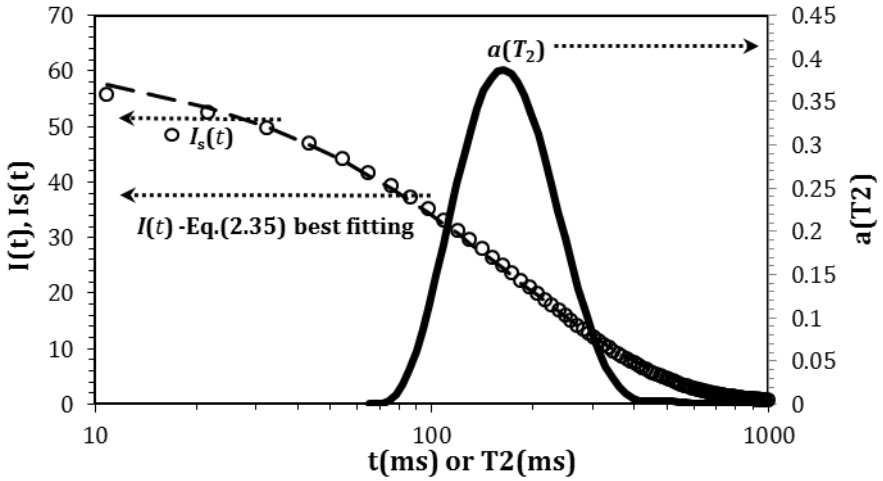

Figure 3.15 Eq.2.35 best fitting (I(t), dashed line) to experimental signal decay (I_s, open circles). $a(T_2)$, representing the amplitude of the spectral component at relaxation time T_2, indicates the result of this fitting.

The continuous line indicates the result of the best fitting in terms of the spectral component at relaxation time T_2, $a(T_2)$. As underlined in part I, the condition of fast

diffusion is met. Accordingly, each mesh size can be associated to only one relaxation time and the continuous mesh size distribution can be directly deduced from the T_{2m} distribution. If it were not the case, more than one relaxation time would be necessary to describe the relaxation of the water entrapped in a mesh of dimension ξ and the conversion $T_{2m} - \xi$ would not be so straightforward. The appearance of only one peak in the continuous distribution (solid line in Figure 3.15) suggests a gel network rather homogeneous in terms of mesh size. Finally, eqs.2.44 and 2.45 allow the determination of the mesh size distribution according to eq.2.46 (figure 3.16). Within the experimental error, $P_i(\xi)$ presents a single-modal distribution of mesh diameters with a peak at about 29 nm.

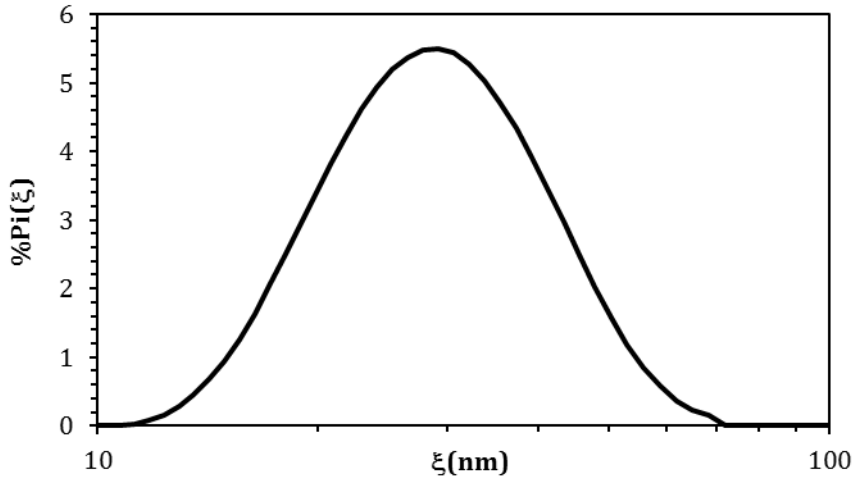

Figure 3.16 Percentage probability P_i (ξ) of finding a mesh of size ξ inside the polymeric network of our hydrogel

Based on this result, we would expect the gel to slow down the diffusion of dissolved ingredients with hydrodynamic radius of the order of 15 nm. Based on this consideration, we then decided (in collaboration with Istituto Nazionale di Scienza e Tecnologia dei Materiali (Napoli), and the Salerno University-Department of Industrial Engineering) to measure the characteristic times of diffusion t_{diff} of a model drug. Hence, the gel was loaded with B12 and the release has been monitored on time. To evaluate the release of B12, few ml of the dissolution bulk were withdrawn and analyzed by UV-vis spectrometer in the range of 400-190 nm, since vitamin B12 absorbs at the wavelength of 360 nm. After measurements, the withdrawn volume and the Petri dish were reinserted in the beaker. Cumulative percentage release of vitamin B12 from the gel was

expressed as the percentage ratio between the vitamin B12 detected at the time *t* ($B12_t$) and the initial vitamin B12 ($B12_i$) amount added in the gel: $B12_{released}\%=(B12_t/B12_i)*100$.

As this gel undergoes erosion roughly developing in a three phases (up to 1 day, from 1 to 9 days and from 9 to 26 days (Dalmoro et al., 2017)), B12 release is the result of both diffusion in the polymeric network and network erosion. In about the first day (28 h), a 10 % of the total weight of the gelled is lost; this could be ascribed to the release of uncross-linked chitosan chains that quickly dissolve into the buffer media (first phase) allowing a gel rearrangement (drop in water content) and simultaneous release of a large amount of B12. Then, a plateau region is observed up to 9 days (216 h); this could be interpreted as an induction period in which the slow hydrolysis of the chains is not synchronous to a reduction in weight (second phase). In other words, the slow random scission of the network chains does not immediately induce the formation of oligomeric species, whose diffusion out of the gel causes a reduction of weight. After the 9th day, the weight began to decrease in a steep way, as also observed from thickness shrinkage. The total mass reduces up to a residue of about 10 % at the 16th day (third phase). Finally, breaks of the residual gel matrix induced final weight loss, thus complete erosion was observed at 28 days since the test's starting (all the gelled chitosan disappears from the Petri dish). All in all, these facts lead us to conclude that the degradation belongs to the bulk-erosion process, in agreement with what observed by Dang and co-workers (Dang et al., 2011).

The profile of B12 release (Figure 3.17) is coherent with the phenomena observed during the erosion tests. Indeed, the B12 release in the dissolution bulk occurs in two main steps. Each step is driven by a different mechanism: the first is probably due to the "free" passage of B12 from unstructured part of CS/βGP gel. The second, instead, is due to diffusive phenomena of B12 through the aqueous medium entrapped in the large pores of the well-structured gel.

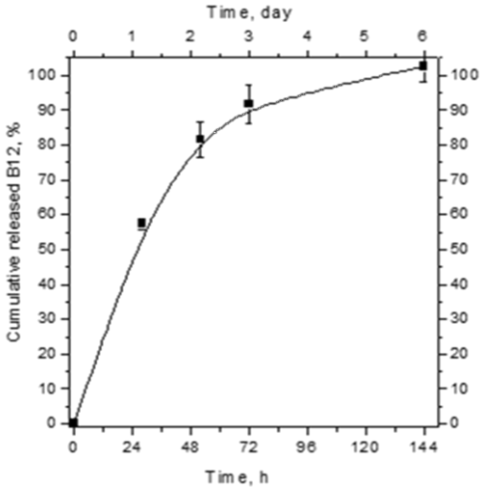

Figure 3.17 Cumulative percentage release of B12 vitamin from crosslinked chitosan gel

3.1.2 Salt addition and sonication time effect on the structuration of highly-carboxilated cellulose suspension

3.1.2.1 Introduction to cellulose fibers

Over the last two decades, a large amount of research has focused on natural cellulose fibers, since they are "green" and renewable raw materials: they are a unique and promising natural materials extracted from native cellulose (found in plants, animals, and bacteria) composed of the nanoscale structure material (figure 3.18).

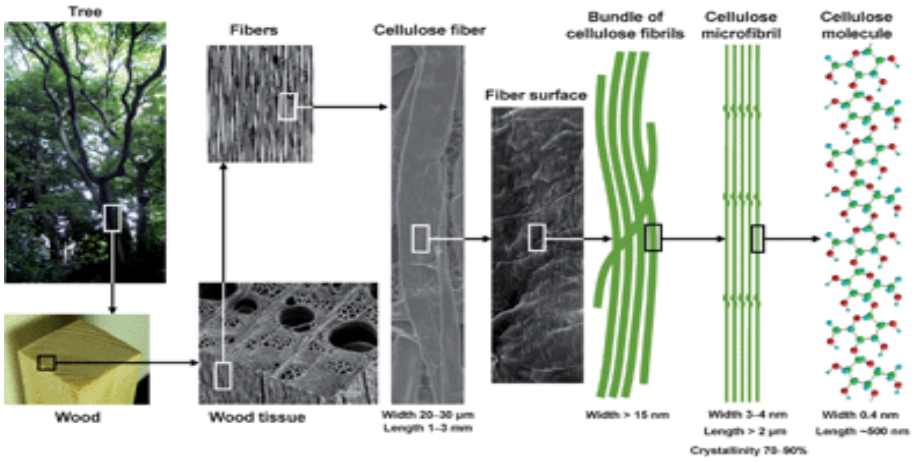

Figure 3.18 Hierarchical structure of wood biomass and the characteristics of cellulose myofibrils (Isogai et al., 2010)

Cellulose is a linear homopolymer composed of D-glucopyranose units linked by β-1,4-glycosidic bonds; when cellulose is nanostructured, it is called nanocellulose. There are three different types of nanocellulose cellulose nanocrystals (CNC), cellulose nanofibrils (CNF) and bacterial cellulose (BC).

Much attention is raised for nanocellulose use as biomedical material, because of its remarkable physical properties, special surface chemistry and excellent biological properties (biocompatibility, biodegradability and low toxicity) (Lin and Dufresne, 2014). Its applications spread from rheological modifiers (Misich et al., 2013) or paper additives (Wang et al., 2014), to tissue engineering, drug delivery (Lonnber et al., 2008) and functional materials (Karim and Afrin, 2015).

However, the processing of cellulose is complicated by its very strong fibrillary structure. Using different kind of pretreatments such as chemical or enzymatic methods, it is possible to increase the accessibility of cellulose to swelling and reactive agents and more controlled derivatization is possible (Hiltunen et al., 2005). The main problem is the completely isolation of individualized cellulose microfibrils from plant cellulose fibers without serious damage or yield losses, because numerous hydrogen bonds are present between cellulose microfibrils in cellulose fibers. In 2006, a new method emerged to prepare completely individualized cellulose nanofibrils (3-4 nm wide and few microns long) from wood cellulose fiber by 2,2,6,6-tetramethylpiperidine-1-oxyl radical (TEMPO) mediated oxidation under moderate aqueous conditions (Saito et al., 2007).

In this thesis, we exactly deal with native wood cellulose oxidized by (TEMPO)-mediated oxidation, obtaining the fibrous TEMPO-oxidized celluloses (TOCs). This new preparation method already finds applications in biomedical field as biomolecules carriers (Weishaupt et al., 2015), drug delivery (Shimotoyodome et al., 2011) and polysaccharide sponge (Lin et al., 2012). This chapter focusses on the study of the three-dimensional arrangement of nanocellulose fibers in presence of salts and sonication time.

3.1.2.2 Materials

All reagents used were from Sigma (St. Louis, MO) and were used without further purification. Never dried soft bleach pulp (Celeste90©) were received from SCA-Ostrand© (Sweden).

2,2,6,6-tetramethylpiperidinyloxy (TEMPO) oxidized cellulose (TOC) was obtained by the a slight modification of the Saito et al. procedure (Saito et al., 2007). In brief, 1g of cellulose pulp was swollen in 100ml water under stirring for 1 hr. Then 0.1g NaBr, 1.75mL NaClO and 16.2mg TEMPO were added under vigorous stirring. The pH of the solution was maintained in the interval 10.5-11-0 by addition of 1M NaOH until it remained almost constant (around 0.75ml NaOH were added). Then, the slurry of TOC was carefully purified by other chemicals and brought to pH 7 by repeated washings in ultrapure water and concentrated by a rotary evaporator (Heidolph, Schwaback Germany) to obtain a final TOC concentration of 6 mg/ml.

System sonication was performed by using an ultrasonic homogenizer (HD2200 Bandelin Sonoplus, Berlin Germany) equipped with a 13 mm titanium tip. An output power Weff of 160W was delivered in 40 ml of TOC slurry for a variable time.

Titrations were performed to determine the carboxylation of TOC. The pH of a TOC suspension (2 mg/ml) was brought to 2.0 by HCl and 1mM NaCl was added. Then, the pH was raised until 13.0 by addition of small aliquots of sodium hydroxide (0.1 M). The pH and conductivity values were recorded after each addition by a HD 2256.2 Delta Ohm instrument (Padova, Italy). This measurement, allowed to conclude that about 41% of the cellobiose units were carboxylated.

3.1.2.3 Results and discussion: I part

The dynamic rheological behavior of 6 mg/ml TOC suspensions, characterized by different sonication times (0, 30, 60, 120, 240, 360, 480 sec) was investigated in detail by frequency sweep tests (in the linear viscoelastic range) in the interval 0.01-10 Hz (Fig. 3.19) and by the flow curve (Figure 3.20). Mechanical spectra allow individuating three distinct rheological behaviors. In fact, when the sonication times lies in the interval 30-360 sec, samples showed a gel-like behavior

(Winter and Chambon 1986), being G' >> G'' and G' independent of frequency (Figure 3.19). In addition, these systems show a sudden drop of viscosity at stress around 60 Pa (Figure 3.20), this indicating the fracture of the internal structure. Interestingly, despite their gel nature, the connectivity of these gels is not very high. Indeed, assuming, for the sake of simplicity, that the shear modulus of the gels is represented by the average G' value over the frequency range explored (≈ 60 Pa – see Fig. 3.19) and that Flory theory holds (Flory, 1953), the resulting average mesh size is considerable wide (≈ 50 nm).

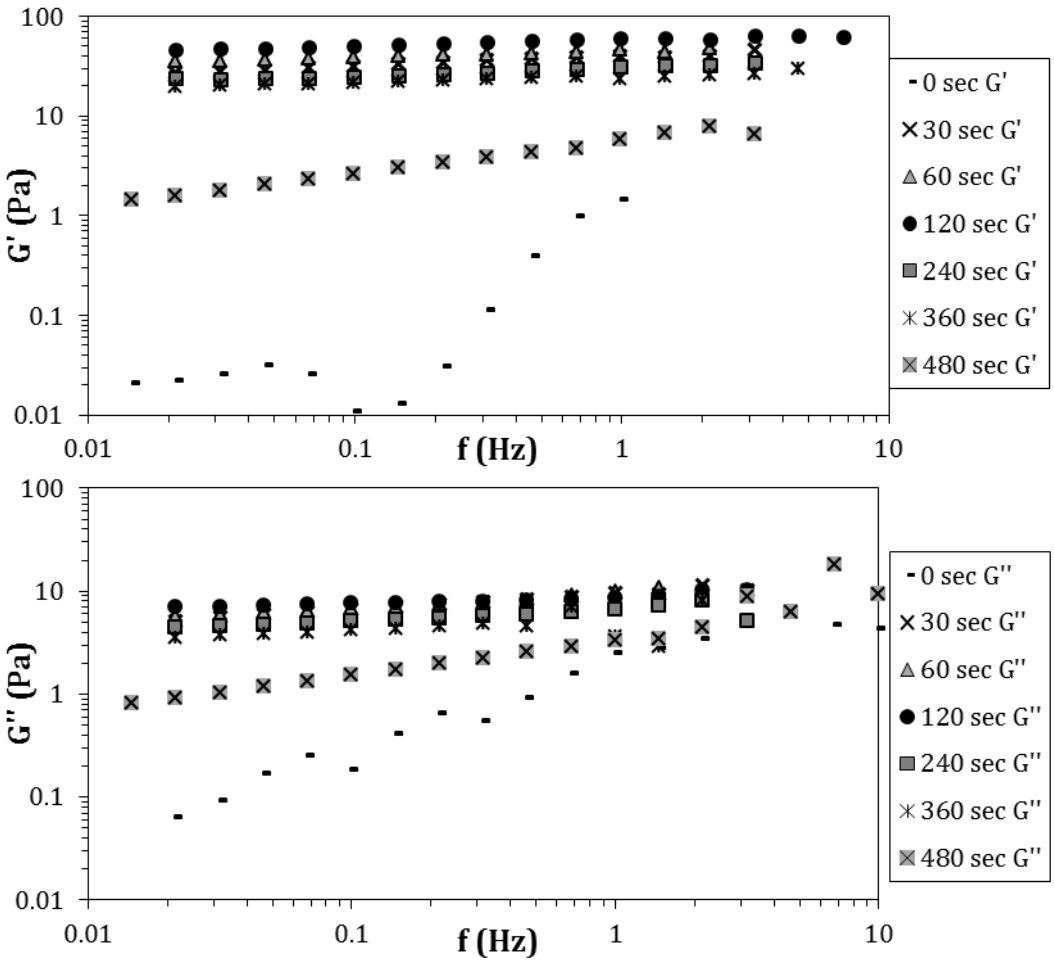

Figure 3.19 Frequency Sweep test on TOC suspensions no sonicated (0 sec) and sonicated at variable time: in upper graph, G' values are reported, beneath also G'' values are reported

Accordingly, this evidence suggests the presence of a tenuous, transient network (statistical network), involving non-covalent associations among polymeric chains, typical of weak polysaccharides gels (Grassi et al, 1996; Coviello et al., 2013). Despite these considerations, the effect of sonication is not negligible as, without

sonication, TOC suspension showed $G' < G''$, G' frequency dependent, low and constant viscosity over the whole interval of stress values (see Fig. 3.19, 3.20).

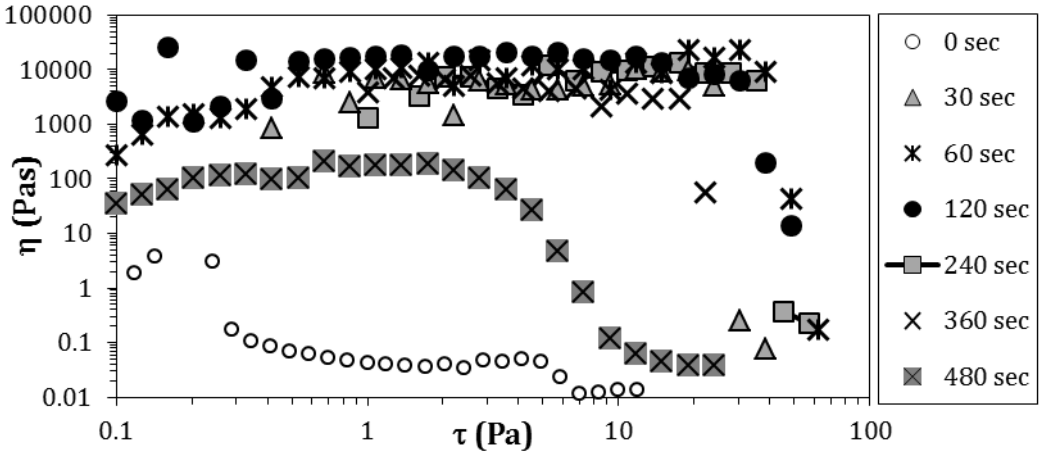

Figure 3.20 Flow curve on TOC suspensions no sonicated and sonicated in a range from 30 to 480 sec

Finally, for sonication times ≥ 480 sec, an intermediate behavior occurred. Indeed, mechanical spectra revealed the decrease of G' that approaches G'', being both moduli frequency dependent, so that the condition of incipient weak gel (sol-gel transition) should be used for these systems (Coviello et al., 2013). Indeed, as performed before for the stiffer gels, the application of Flory theory would lead to the conclusion that the average mesh size is wide, being around 110 nm (average shear modulus ≈ 6 Pa). The scarce connectivity of these systems is also proved by the flow curve trend. Indeed, not only the zero shear viscosity is lower with respect to stiffer gels (see Figure 3.20), but also the abrupt viscosity drop, seen for stiffer gels, has been substituted by a smooth decrease starting from shear stress ≥ 5 Pa. Thus, a too long sonication time seems to hinder the formation of a three-dimensional network probably because of a too efficient nano-fibrils detachment.

Transversal nuclear magnetic relaxation time (T_2) of water was used to get further insight about the organization of TOC nano-fibrils in suspensions with or without sonication. Table 3.1-1 reports the average water relaxation time (T_{2m}), its components (T_{2i}) and the respective relative abundances (A_i) for the different sonication times considered. The double phase nature of TOC dispersion without sonication (it consists of a superior liquid phase lying on an inferior ensemble of

polymeric clusters), suggested to consider as representative relaxation time, that associated to the liquid phase.

Table 3.1-1 Average water relaxation time (T_{2m}), and relaxation spectra (A_i, T_{2i}) referring to nano-cellulose systems undergoing different sonication times.

Sony time (s)	T_{2m}(ms)	T_{21}(ms)	A_1%	T_{22}(ms)	A_2%
0	1747	/	/	/	/
30	1531	1703	71.2	1108	28.8
60	1651	1745	75.5	1360	24.5
120	1476	/	/	/	/
240	1448	/	/	/	/
360	1412	/	/	/	/
480	1360	/	/	/	/

Table 3.1-1 shows that only in the 30 and 60 s cases two relaxation times are needed to describe the relaxation of the xy component (M_{xy}) of the magnetization vector (M). However, as the two relaxation times (T_{21}, T_{22}) do not differ too much and the relative abundance (A_1) is preponderant with respect to the other (A_2), it can be concluded that, whatever the sonication time, homogeneous systems occurred (Chiu at al., 1995).

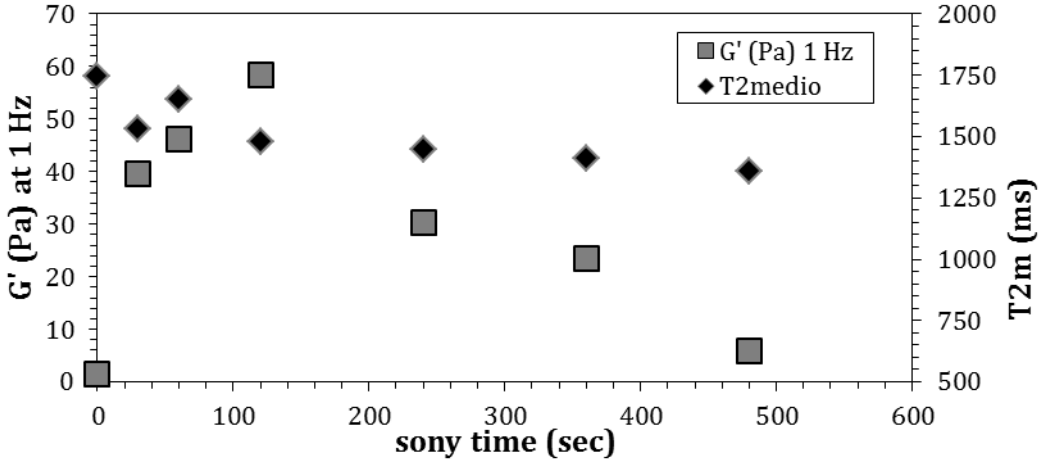

Figure 3.21 Dependence of the average relaxation time (T_{2m}) and the elastic modulus G'(1 Hz) on the sonication time (nano-cellulose based systems).

Figure 3.21 shows that the increase of the sonication time implies a reduction of T_{2m} and this, in turn, indicates that fibers progressively detach each other so that the polymeric surface available for the interaction with water molecules increases.

Indeed, the higher the solid (polymeric) surface available for interaction with water, the lower the water ^1H relaxation time (Chiu et al., 1995). Accordingly, 480 s represent the nano-fibrils maximum separation grade. In addition, Figure 3.21 allows understanding the complementarity of rheology and LF-NMR. Indeed, while LF-NMR indicates the nano-fibrils detachment increases with the sonication time (T_{2m} decreases), rheology provides information about the nano-fibrils attitude to form a three-dimensional network. Up to 120 s, T_{2m} and G' are inversely proportional, this indicating that fibers detachment favors their interaction to form a three-dimensional network. On the contrary, longer sonication times imply further fibers detachment (T_{2m} decreases) but a reduced attitude to form a three-dimensional network as G' decreases.

The importance of sonication can be also indirectly evinced by salt addition to the TOC system. Indeed, choosing the 240 sec sonication condition as the average sample, it is interesting evaluating the effect of two different way of salt addition, i.e. before or after sonication. At this purpose, sodium chloride (NaCl) and calcium chloride ($CaCl_2$) were added in two different concentrations (10 or 100 mM) before sonication. In so doing, four samples were prepared: 1-NaCl 100mM, 2-NaCl 10mM, 3-$CaCl_2$ 100mM, 4-$CaCl_2$ 10mM. All salty solutions were, then, sonicated for 240 sec. The rheological behavior of these suspensions were investigated, in the linear viscoelastic field, by frequency sweep test (Figure 3.22) and flow curves (Figure 3.23)

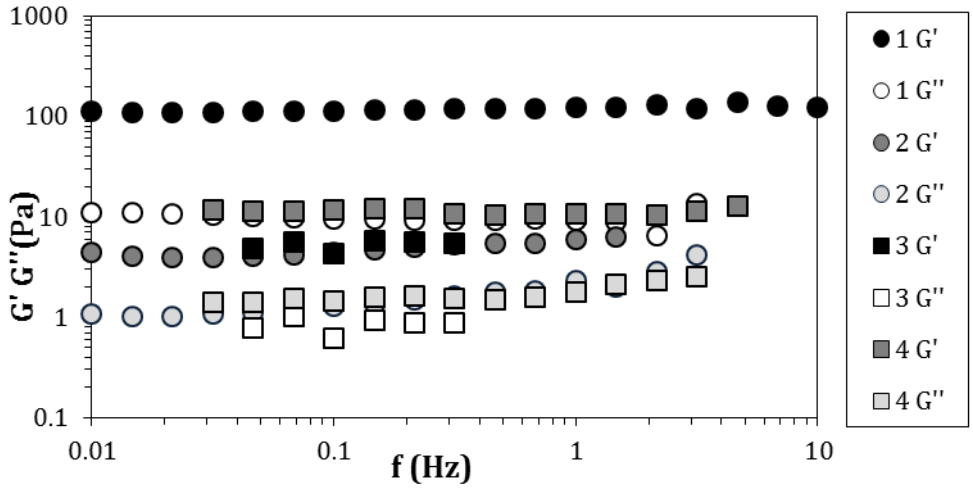

Figure 3.22 Mechanical spectra of sonicated suspensions, where NaCl (100-10 mM:1-2) or $CaCl_2$ (100-10mM:3-4) was added.

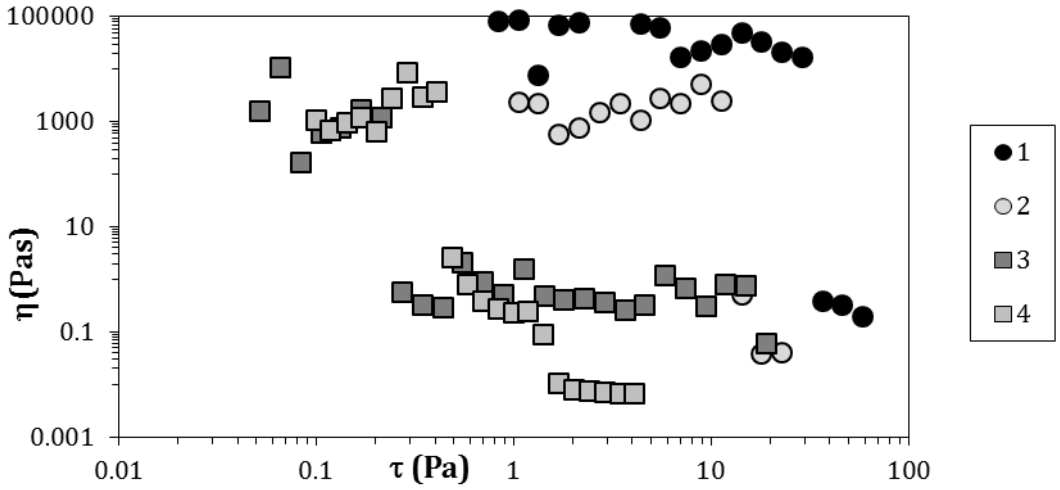

Figure 3.23 Flow Curve of TOC suspensions 1-2-3-4

Figures 3.22 and 3.23 reveal that the choice of salt and its concentration have strong influence on the final structure. Sample 1 (NaCl 100mM) is the strongest one, being its *G*' one order of magnitude bigger than *G*' of the others systems. In addition, sample 1 shows the typical gel behavior being *G*' >> *G*'' and both moduli being frequency independent. In addition, NaCl 100mM presence makes the system stronger than the simple solution sonicated for 240 s (see Figure 3.19). Also Samples 2 (NaCl 10mM) and 4 ($CaCl_2$ 10 mM) present a gel behavior because *G*' >> *G*'' and both moduli are frequency independent. However, these gels are weaker than sample 1 as both *G*' and *G*'' are, about, one order of magnitude lower. Notably, salt addition, does not reflect in system strength increase (compare *G*' values of Figure 3.19 and 3.22). System 3 ($CaCl_2$ 100mM) is the weakest one and its instability, due to its heterogeneity, makes it very fragile and difficult to manage. Accordingly, in this case, salt presence lowers the fibers attitude to form a three-dimensional network so that it is hard supposing that a significant fibers structuration takes place. Flow curves (Figure 3.23) substantially confirm the above discussed scenario.

If, on the contrary, salt is added after 240 sec sonication, the scenario changes a lot. The new four samples, indicated with a star (1*,2*,3*,4*), were characterized by frequency sweep test (linear viscoelastic field; Figure 3.24) and flow curve (Figure 3.25).

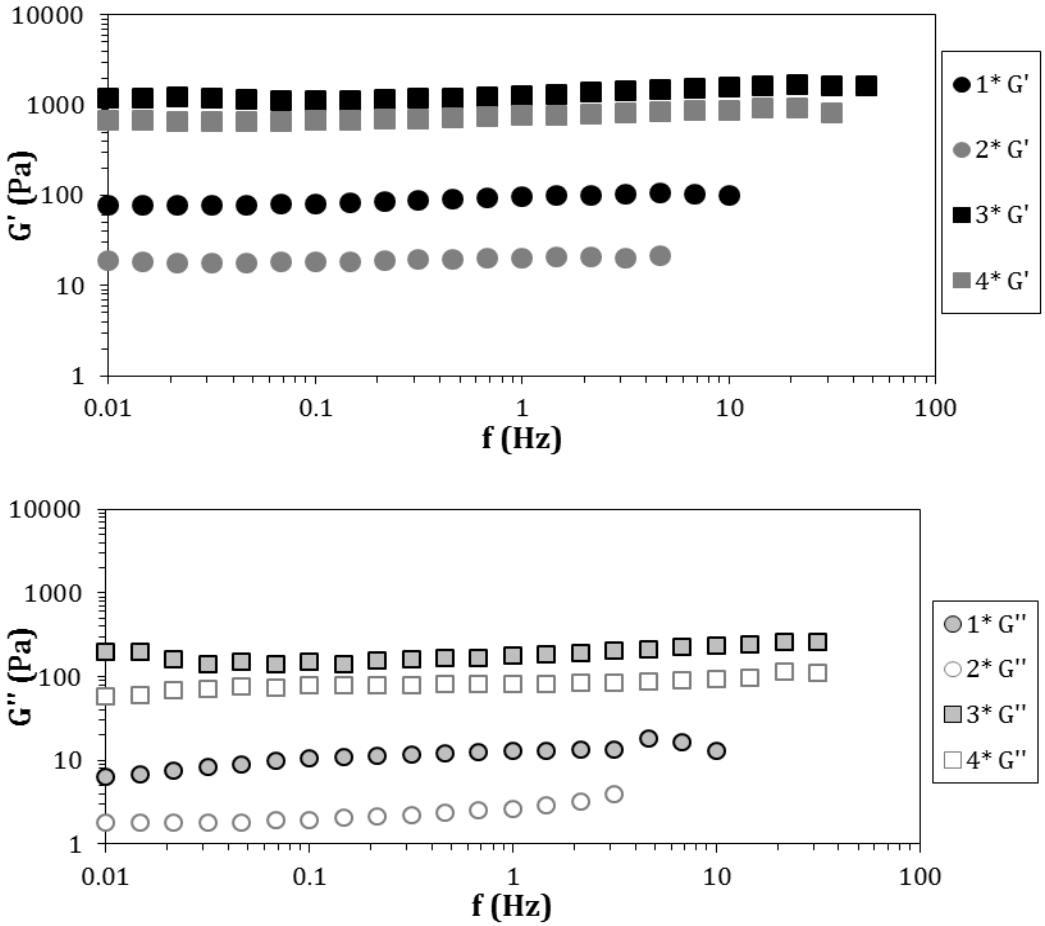

Figure 3.24 Frequency sweep of systems 1*, 2*, 3* and 4*: above are reported *G'* values, below *G''* ones

While salt addition after sonication did not reflect in substantial effect on systems 1 and 2, a huge difference occurred for systems 3 and 4. Indeed, the comparison of systems 1 - 1* and 2-2* (NaCl) reveals similar rheological behaviors (see Figures 3.22 – 24). On the contrary 3-3* and 4-4*present a huge *G'* – *G''* increase, this witnessing the importance of $CaCl_2$ addition after sonication (see Figures 3.22 – 24). Interestingly, for gels 3*, the application of Flory theory would lead to the conclusion that the average mesh size is around 19 nm (average shear modulus ≈ 1000 Pa). It is probable that sonication, inducing fibers separation, allows a better Ca^{++} interaction with TOC fibers, this leading to a strong gel. Without sonication an inhomogeneus gel forms, because of the formation of an external gel layer hindering the diffusion of Ca^{++} in the inner part. Interestingly, however, no huge difference appears between the 10 mM and the 100 mM gels. This could be due to a sort of saturation of TOC sites where polymeric chain - Ca^{++} interactions take

place. Probably, the different systems behavior (Figure 3.22-24) is due to the different dimension of the cations (Na^+, Ca^{++}).

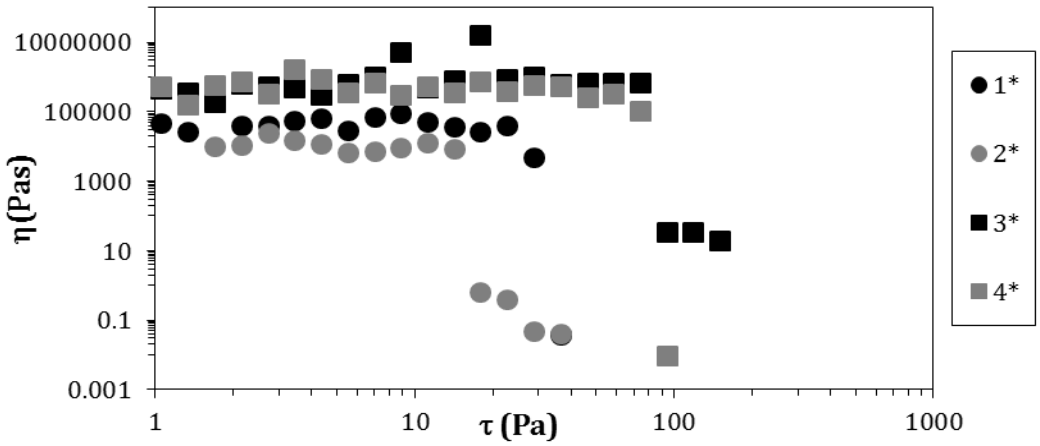

Figure 3.25 Flow curve of systems 1*, 2*, 3* and 4*

While the smallest Na^+ does not necessitate the effect of sonication to get the interaction sites of cellulose fibers, the biggest Ca^{++} cannot get the interaction site unless sonication promotes fibers detachment.

Interestingly, Table 3.1-2 reveals that salt addition after sonication reflects in weak variations of T_{2m} whatever the system. On the contrary, it implies the formation of more complex three-dimensional architectures as witnessed by the increase of the relaxation times numbers (up to three for systems 1*, 3* and 4*).

Table 3.1-2 Average water relaxation time (T_{2m}), and relaxation spectra (A_i, T_{2i}) referring to nano-cellulose systems where salt was added before or after (* systems) 240 s sonication

Sample	Salt	[mM]	T_{2m}(ms)	T_{21}(ms	A_1%	T_{22}(ms)	A_2%	T_{23}(ms)	A_3%
1	NaCl	100	1142	1825	24	918	76	/	/
1*	NaCl	100	1392	1943	36	1281	45	613	19
2	NaCl	10	990	/	/	/	/	/	/
2*	NaCl	10	880	1284	7	848	93	/	/
3	$CaCl_2$	100	1421	/	/	/	/	/	/
3*	$CaCl_2$	100	1313	2204	32	1124	37	601	31
4	$CaCl_2$	10	1298	/	/	/	/	/	/
4*	$CaCl_2$	10	1123	2119	24	857	66	514	10

In addition, whatever the salt and the concentration considered, both systems 1-4 and 1*-4* show a clearly more complex architecture with respect to corresponding solution without salt addition that are characterized by only one relaxation time (see Table 3.1-1). This means that both NaCl and $CaCl_2$ coordinate fibers in a more complex way than simple sonication does.

Again, the joint use of rheology and LF-NMR can enlighten structural aspects otherwise hidden by the use of only single approach.

3.1.2.4 Results and discussion: II part

In order to better understand the effect of sonication time, the attention was focused on salt addition (100 mM NaCl or $CaCl_2$) to nano-cellulose systems after different sonication times. In particular, 30, 60, 120, 240, 360, 480 sec were considered. Whatever the sonication time, the addition of both Na^{+} or Ca^{++} gives origin to gels, as proved by the frequency independence of *G*' and *G*'' and the clear prevalence of *G*' on *G*'' (data not shown). In addition, Figure 3.26 showing, for system 1* (NaCl), the *G*' variation with sonication time and frequency, makes clear that *G*' increases up to 120 s and, then, it undergoes a small reduction.

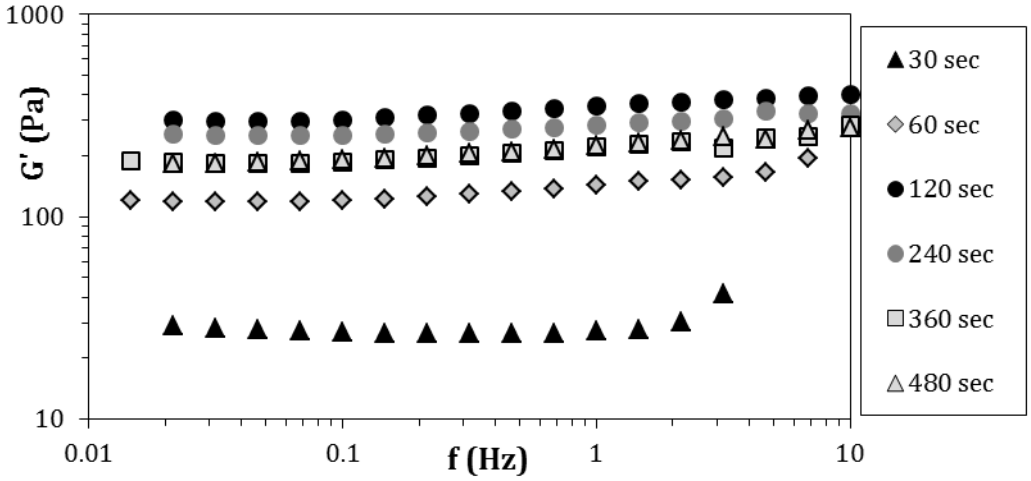

Figure 3.26 G' trend with frequency for samples belong to series 1*(addition of NaCl 100 mM after sonication).

Figure 3.27 (system 3* $CaCl_2$), reporting the *G*' variation with sonication time and frequency, reveals that, up to 120 s, *G*' considerably increases and it remains substantially constant for higher sonication times. This is probably due to the fact that ion-polymer interaction sites become more and more available to Ca^{++} as

nano-fibrils undergo un-packing. As the effect of sonication time is more evident in the case of the bigger Ca^{++} ion, it is evident the crucial role of nano-fibrils un-packing to make the interaction sites available. Interestingly, once nano-fibers are un-packed, the ability of Ca^{++} to form a three-dimensional structure is much better than that of Na^{+}.

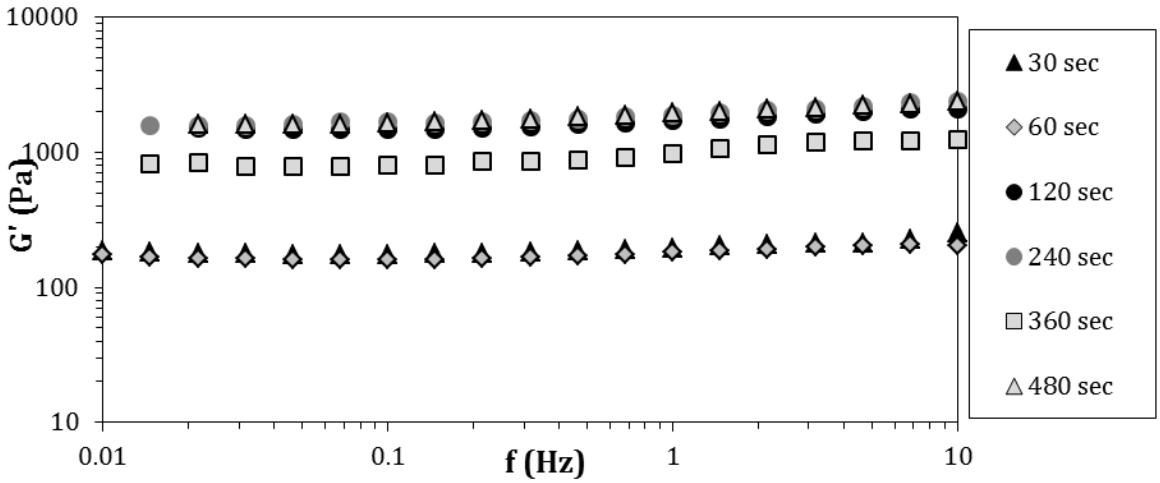

Figure 3.27 *G'* trend vs frequency for samples 3* (addition of $CaCl_2$ 100 mM after sonication).

In order to join the information coming from LF-NMR and Rheology, Tab 3.1-3 reports the average relaxation time T_{2m} and the relaxation spectra (A_i, T_{2i}) for systems 1* and 3* undergoing different sonication times. For what concerns systems 1*, Table 3.1-3 and Figure 3.28 indicate that T_{2m} does not seem undergoing important variation with the sonication time. As the un-salted system behavior does not detach so much (Tab. 3.1-1 and Figure 3.19), sonication time does not seem so important in the case of NaCl addition as, probably, Na^{+} can get the polymer interaction site very easily regardless of the un-packing grade of fibers. However, different sonication times reflect in more complex structures respect to the un-salted system (see Tab. 3.1-1) as two, instead of only one, relaxation times appear (Tab. 3.1-3).

Table 3.1-3 Average water relaxation time (T_{2m}), and relaxation spectra (A_i, T_{2i}) referring to nano-cellulose systems undergoing salt addition (NaCl or $CaCl_2$ 100mM) after different sonication times t(s).

Sample	Salt	*t*(s)	T_{2m}(ms)	T_{21}(ms)	A_1%	T_{22}(ms)	A_2%
1*	NaCl	30	1331	1452	82.2	774	17.8
1*	NaCl	60	1906	2104	79	1155	21
1*	NaCl	120	1548	1696	76	1073	24
1*	NaCl	240	1569	1806	57	1262	43
1*	NaCl	360	1386	1671	60	962	40
1*	NaCl	480	1503	1834	34	1331	66
3*	$CaCl_2$	30	1590	1782	80	812	20
3*	$CaCl_2$	60	1581	1856	74	789	26
3*	$CaCl_2$	120	1423	1943	48	946	52
3*	$CaCl_2$	240	1179	1721	33.	907	67
3*	$CaCl_2$	360	1145	1721	33	855	67
3*	$CaCl_2$	480	1090	1500	38	833	62

This could explain why sonication time implies a variation of gel mechanical properties as nicely documented by Figure 3.28 showing the T_{2m} and G'(1Hz) trend versus the sonication time. In conclusion, anyway, it seems that the sonication time is not important when NaCl is added.

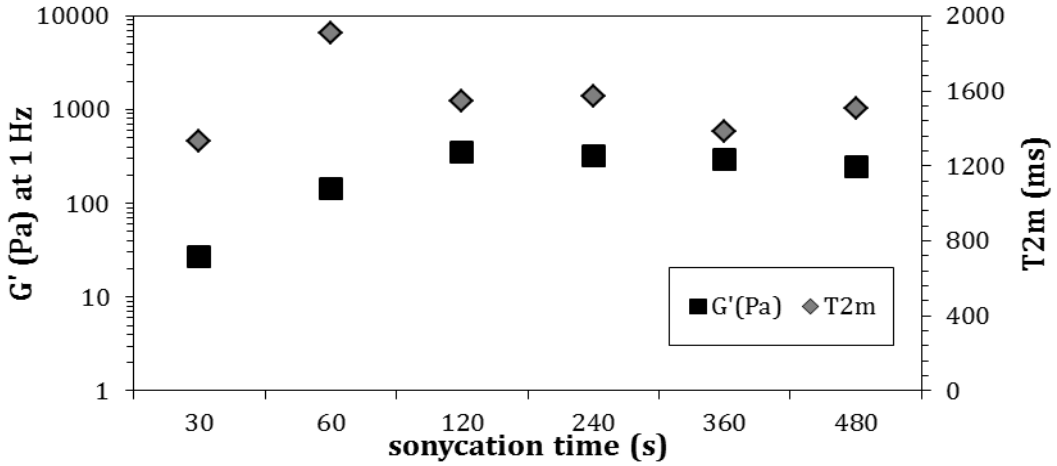

Figure 3.28 G' (1 Hz) and T_{2m} trend versus sonication time for system 1* (addition of NaCl 100 mM after sonication) at different sonication times.

For 3* systems (addition of $CaCl_2$ 100 mM), on the contrary, the effect of sonication time is much more important as also seen from the rheological characterization (Figure 3.27). Indeed, T_{2m} decreases up to 240 s and then it undergoes a very small reduction (Tab. 3.1-3 and Figure 3.29). Interestingly, this is due to the behavior of the lowest relaxation time (T_{22} – Tab. 3.1-3), almost constant with the sonication time (≈ 850 ms), but characterized by an increasing importance of its relative abundance (A_2 – Tab 3.1-3) up to 240 s, than an almost constant value is maintained. In this case, a perfect matching between LF-NMR and rheology occurs as the increase of G' implies a reduction of T_{2m} (Figure 3.29). Then, both of them are practically constant, i.e. gel does not sensibly change its structure.

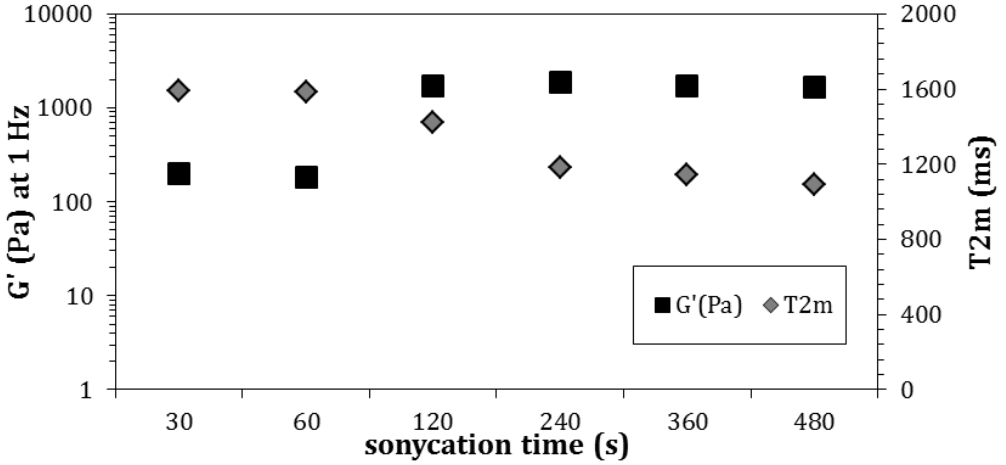

Figure 3.29 G' (1 Hz) and T_{2m} trend versus sonication time for system 3* (addition of $CaCl_2$ 100 mM after sonication) at different sonication times.

Finally, the importance of cations (both Na^+ and Ca^{++}) in ensuring gel stability is given by the following Figures 3.30, 3.31 and 3.32, reporting the variation of T_{2m} with the sonication time for the system without salt (Figure 3.30), with NaCl 100 mM (Figure 3.31) and $CaCl_2$ 100 mM (Figure 3.32). Figure 3.30 tells us that after 15 days resting at 25°C, for TOC systems sonicated below 120 sec, the average T_{2m} tends to decrease, while remains constant for further sonicated TOC systems. This means that these systems, for short sonication time, are not stable due to nano-fibrils re-packing. On the contrary, above 120 sec or when salts are present, although a system evolution occurs, the features of the original systems are essentially maintained as witnessed by the T_{2m} trend that does not detach so much from the that of the freshly prepared systems (Figures 3.31, 3.32).

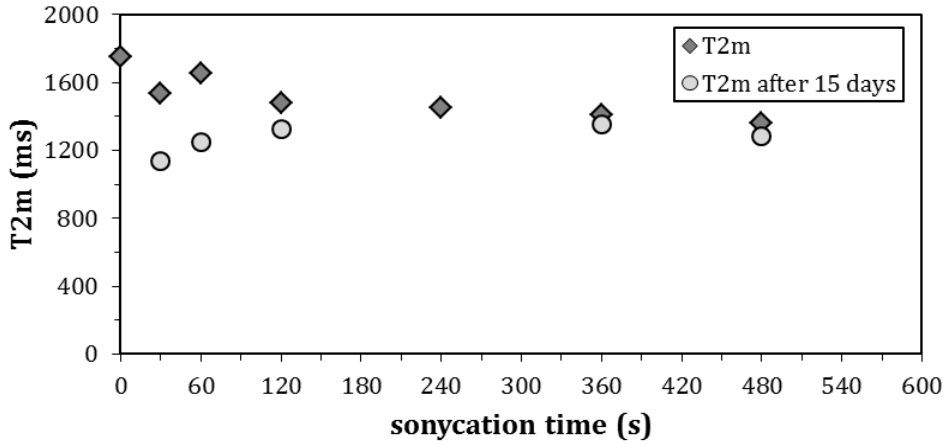

Figure 3.30 T_{2m} trend versus sonication time for freshly prepared (dark grey diamonds) and 15 days aged (light grey circles) un-salted systems.

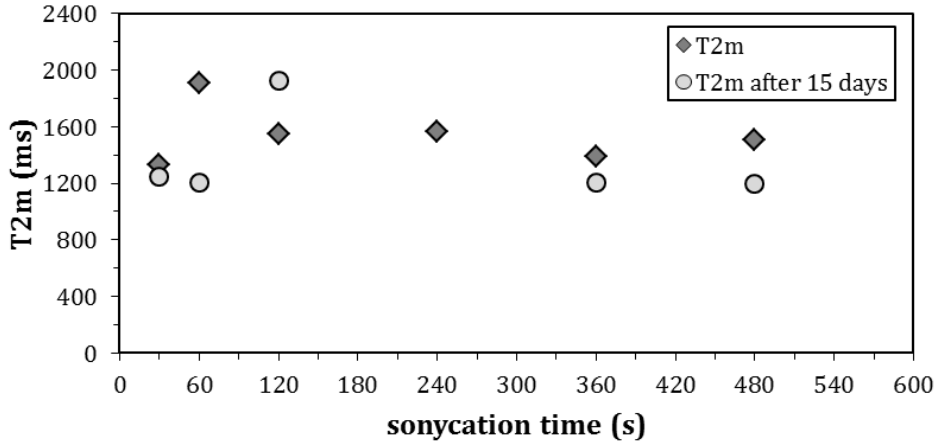

Figure 3.31 T_{2m} trend versus sonication time for freshly prepared (dark grey diamonds) and 15 days aged (light grey circles) NaCl 100 mM added systems.

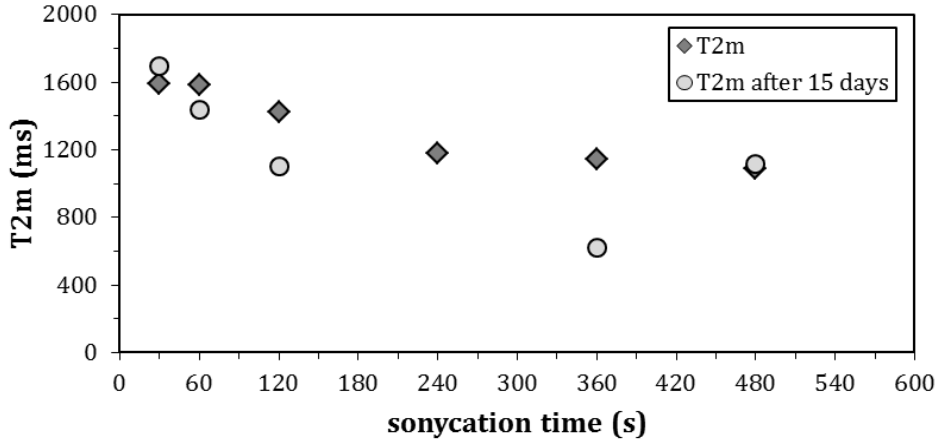

Figure 3.32 T_{2m} trend versus sonication time for freshly prepared (dark grey diamonds) and 15 days aged (light grey circles) $CaCl_2$ 100 mM added systems

Reference

Barba A.A., Dalmoro A., d'Amore M., Lamberti G. "Controlled release of drugs from microparticles produced by ultrasonic assisted atomization based on biocompatible polymers" *Chem. Biochem. Eng. Q.* 2012 (26):345–53

Brownstein K.R., Tarr C.E. "Importance of classical diffusion in NMR studies of water in biological cells" *Phys. Rew. A* 1979 (19):2446-53

Chiarappa G., Abrami M., Dapas B., Farra R., Trebez F., Musiani F., Grassi G., Grassi M. "Mathematical modeling of drug release from natural polysaccharides based matrices" *Nat. Prod. Commun.* in press 2017

Chui M.M., Phillips R.J., McCarthy M.J. "Measurement of the porous microstructure of hydrogels by nuclear magnetic resonance" *J. Colloid Interface Sci.* 1995 (174):336–44

Coviello T., Matricardi P., Alhaique F., Farra R., Tesei G., Fiorentino S., Asaro F., Milcovich G., Grassi M. "Guar gum/borax hydrogel: rheological, low field NMR and release characterizations" *Express Polym. Lett.* 2013 (7):733–46

Dalmoro A., Abrami M., Galzerano B., Bochicchio S., Barba AA., Grassi M., Larobina D. "Injectable chitosan/β-glycerophosphate system for sustained release: gelation study, structural investigation, and erosion tests" *Curr. Drug Deliv.* 2017 (14)

Dang Q.F., Yan J.Q., Li J.J., Cheng X.J., Liu C.S., Chen X.G. "Controlled gelation temperature, pore diameter and degradation of a highly porous chitosan-based hydrogel" *Carbohyd. Polym.* 2011 (83):171-8

Filion, D.; Lavertu, M.; Buschmann, M.D. "Ionization and solubility of chitosan solutions related to thermosensitive chitosan/glycerol-phosphate systems" *Biomacromolecules* 2007 (8):3224-34

Flory P. J. "Principles of polymer chemistry" *Cornell University Press*, 1953

Grassi M., Lapasin R., Pricl S. "A study of the rheological behavior of scleroglucan weak gel systems" *Carbohydr. Polym.* 1996 (29):169-81

Hiltunen M., Maunu S.L., Tenhu H. 13th International Symposium on Wood, Fibre and Pulping Chemistry (ISWFPC) Auckland, New Zealand, 2005 Proceedings (3):143-6

Holz M., Heil S.R., Sacco A. “Temperature-dependent self-diffusion coefficients of water and six selected molecular liquids for calibration in accurate 1H NMR PFG measurements” *Phys. Chem. Chem. Phys.* 2000 (2):4740–42

Huynh C. T., Nguyen M. K., Lee D. S. “Injectable block copolymer hydrogels: achievements and future challenges for biomedical applications” *Macromolecules* 2011 (44):6629–36

Isogai A., Saito T., Fukuzumi H. “TEMPO-oxidized cellulose nanofibers” *Nanoscale* 2011(3): 71-85

Jin R., Teixeira L.S.M., Krouwels A., Dijkstra P.J., van Blitterswijk C.A., Karperien M., Feijen J. “Synthesis and characterization of hyaluronic acid-poly(ethylene glycol) hydrogels via Michael addition: an injectable biomaterial for cartilage repair” *Acta Biomater.* 2010 (6):1968–1977

Karim Z., Afrin S. Nanocellulose as Novel Supportive Functional Material for Growth and Development of Cells. Cell Dev Biol 2015 (4): doi:10.4172/2168-9296.1000154

Lavertu M., Filion D., Buschmann M.D. “Heat-induced transfer of protons from chitosan to glycerol phosphate produces chitosan precipitation and gelation” *Biomacromolecules* 2008 (9):640–50

Li Y., Toma R., Toma H “Injectable and biodegradable hydrogels: gelation, biodegradation and biomedical applications” *Chem. Soc. Rev.* 2012 (41):2193–221

Lin N., Bruzzese C., Dufresne A. “TEMPO-oxidized nanocellulose participating as crosslinking aid for alginate-based sponges” *ACS Appl. Mater. Interfaces* 2012 (4): 4948–59

Lin N., Dufresne A. “Nanocellulose in biomedicine: Current status and future prospect” *Eur. Polym. J.* 2014 (59):302-25

Lonnberg H., Fogelstrom L., Samir M.A.S.A., Berglund L., Malmstrom E., Hult A. “Surface grafting of microfibrillated cellulose with poly(e-caprolactone) –synthesis and characterization” *Eur. Polym. J.* 2008 (44):2991–97

Mazeau K., Winter W.T., Chanzy H. “Molecular and crystal structure of a high-temperature polymorph of chitosan from electron diffraction data” *Macromolecules* 1994 (27):7606-12

Misic K.D., Gane P.A.C., Paltakari J. "Micro- and nanofibrillated cellulose as a rheology modifier additive in CMC-containing pigment-coating formulations" *Ind. Eng. Chem. Res.* 2013 (52): 16066–83

Mohan T., Hribernik S., Kargl R., Kleinschek K:S. "Nanocellulosic materials in tissue engineering applications" chapter in "Cellulose - Fundamental aspects and current trends" edited by Matheus Poletto and Heitor Luiz Ornaghi Junior 2015

Ruel-Gariépy E., Shive M., Bichara A., Berrada M,. Le Garrec D. Chenite A., Leroux JC. "A thermosensitive chitosan-based hydrogel for the local delivery of paclitaxel" *Eur. J. Pharm. Biopharm.* 2004 (57):53-63

Saito T., Kimura S , Nishiyama Y., Isogai A. "Cellulose nanofibers prepared by TEMPO-mediated oxidation of native cellulose" *Biomacromolecules* 2007 (8): 2485–91

Shimotoyodome A., Suzuki J., Kumamoto Y., Hase T., Isogai A. "Regulation of postprandial blood metabolic variables by TEMPO-oxidized cellulose nanofibers" *Biomacromolecules* 2011 (12):3812–18

Singh N.K., Lee D.S. "In situ gelling pH- and temperature-sensitive biodegradable block copolymer hydrogels for drug delivery" *J. Control. Rel.* 2014 (193):214–27

Souza R. D., Zahedi P., Allen C. J., Piquette-Miller M. "Biocompatibility of injectable chitosan–phospholipid implant systems" *Biomaterials* 2009 (30):3813-24

Tan H., Chu C.R., Payne K.A., Marra K.G. "Injectable in situ forming biodegradable chitosan-hyaluronic acid based hydrogels for cartilage tissue engineering" *Biomaterials* 2009 (30):2499–506

Wang Z., Tammela P., Zhang P., Strømme M., Nyholm L. "Efficient high active mass paper-based energy-storage devices containing free-standing additive-less polypyrrole–nanocellulose electrodes" *J. Mater. Chem. A* 2014 (2):7711-16

Weishaupt R., Siqueira G., Schubert M., Tingaut P., Maniura K., Zimmermann T., Thöny-Meyer L., Faccio G., Ihssen J. "TEMPO-oxidized nanofibrillated cellulose as a high density carrier for bioactive molecules" *Biomacromolecules* 2015 (16):3640–50

Winter H.H. and Chambon F "Analysis of Linear Viscoelasticity of a Crosslinking Polymer at the Gel Point" *J. Rheo.* 1986 (30):367-82

Zhou H.Y., Jiang L.J., Cao P.P., Li J.B., Chen X.G. "Glycerophosphate-based chitosan thermosensitive hydrogels and their biomedical applications" *Carbohyd. Polym.* 2015 (117):524-36

3.2 Structure characterization of hydrogels for drug delivery

3.2.1 Degradable PEG functionalized hydrogel for antibodies controlled release

3.2.1.1 Introduction on PEG and Diels-Alder reaction

Among synthetic hydrogels, polyethylene glycol (PEG) hydrogels belong to the most important materials as they exhibit many advantageous properties such as transparency, deformability, biocompatibility (Bal et al., 2013) and permeability to gases and nutrients (Cruise et al., 1998). PEG hydrogels are widely used in biomedical applications including artificial tissue scaffolds, matrices for the controlled release of biomolecules, (Bal et al., 2013), wound dressings (Zhang et al., 2008), and contact lenses (Kopečeg, 2009). Thus, understanding diffusion mechanisms within PEG hydrogels and understanding them with respect to the polymeric structure is of great interest (Hagel et al., 2013). In addition, in most of the hydrogel biomedical applications, precise control over the cross-linking density, and hence the swelling capacity, mechanical properties and degradability of the hydrogel, is crucial for success or failure of the system (Huebsch et al., 2010). The classical chain-growth polymerization techniques do not guarantee a defined gel network and, often, the produced hydrogel suffers from poor reproducibility and incomplete crosslinking, which could represent a potentially toxicological risk (Kloxing et al., 2010). The step-growth polymerization of star-shaped polymer, instead, could lead to a better control over cross-linking density. The resulting hydrogels possess more homogeneous network structures, which often lead to superior mechanics when compared to chain growth networks of similar crosslink density (Lutolf and Hubbel, 2003). In this frame, the Diels-Alder reaction is a very interesting way to get crosslinking. This reaction, consisting in a [4+2] cycloaddition between a conjugated diene and a substituted alkene, is highly specific and occurs in water without any catalyst or initiator. Moreover, DA reaction is reversible at body temperature. Its application in the biomaterials field

is less common and only few examples of its use are present in literature (Kirchhoff et al., 2013). Nevertheless, in this work, in collaboration with the University of Regensburg, Department of Pharmaceutical Technology, I analysed a step-growth polymerization of star-shaped poly(ethylene glycol) (PEG)-derived macro-monomers. As explained, this approach provides better control over the network architecture and allows the synthesis of hydrogels that readily degrade at body temperature. In particular, the rheological, LF-NMR and release tests approaches have been used to study an eight-armed PEG, molecular weight 10 kDa (8armPEG10k) functionalized with furyl (Figure 3.33A) and maleimide groups, respectively. The obtained macro-monomers were cross-linked via DA reaction (Figure 3.33B). This hydrogel degrades under physiological conditions by retro-DA reaction and subsequent ring-opening hydrolysis of the generated malemide groups (Figure 3.33C). (Kirchhof et al., 2015). This means that the release kinetics of a drug, embedded in this kind of hydrogels, will be due to both diffusion and gel erosion.

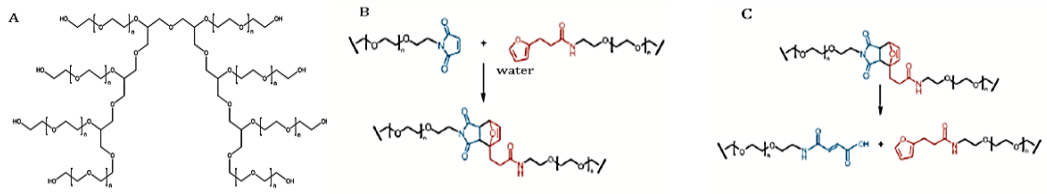

Figure 3.33 A Chemical structure of 8armPEG-furan; **B** Diels-Alder reaction of PEG-malemide and furyl-substituted PEG in water at 37°C; **C** retro D-A reaction (for B and C only one arm of the breached macromonomers is shown).

As model drug for release test, Bevacizumab and fluorescein isothiocyanate-labeled dextrans (characterised by different molecular weight), were used. Bevacizumab is a monoclonal antibody that inhibits angiogenesis by neutralizing vascular endothelial growth factor (VEGF) and it is approved for the treatment of various types of cancer. Furthermore, it is used off label in the treatment of neovascular age-related macular degeneration (AMD) (Ip et al., 2008;The CATT research group, 2011). Since the bioavailability of antibodies in the posterior segment of the eye is generally low, bevacizumab is administered every four to six weeks by intravitreal injection. However, these injections are associated with significant discomfort and rare but severe complications (Sampat and Garg, 2010).

To reduce the injection frequency and improve the compliance, the use of controlled release systems for bevacizumab seems obvious.

3.2.1.2 Material

Eight-armed PEG (10 kDa molecular mass, hexaglycerol core) was purchased from JenKem Technology (Allen, TX, USA) and functionalized with furyl (8armPEG10k-furan) and maleimide groups (8armPEG10k-maleimide) as previously described (Kirchhoff et al., 2013). For the release test fluorescein isothiocyanate-labeled dextrans (FD) with molecular masses of 4 kDa, 20 kDa, 150 kDa and 500 kDa (FD4, FD20, FD150 and FD500) obtained from Sigma-Aldrich (Taufkirchen, 5 Germany) and bevacizumab (Avastin®, 25 mg/ml,roche, Basel, Switzerland) kindly provided by hospital pharmacy, University of Regensburg, Germany, were used.

For rheological measurements, equal molar amounts of 8armPEG10k-furan (38.0 mg) and 8armPEG10k10 maleimide (37.0 mg) were dissolved in 750 µL of water, and cast onto the lower plate of the rheometer. The upper plate was immediately lowered to a gap size of 500 µm, and the sample was allowed to gel over night at 37 °C.

For NMR experiments, equal molar amounts of 8armPEG10k-furan (51.0 mg) and 8armPEG-maleimide (49.0 mg) 20 were dissolved in 1000 µL of water and transferred into an NMR tube.

Lastly, for release test, equal molar amounts of 8armPEG10k-furan (61.0 mg) and 8armPEG10k-maleimide (59.0 mg) were dissolved in 1080 µL of water; 120 µL of an FD (10 mg/ml) or 150 µl of bevacizumab (15 mg/ml) stock solutions were added. Directly after mixing, 375 µL of the prepared solution were cast into cylindrical glass molds (7 mm inner diameter) and allowed to gel over night at 37 °C. The gel cylinders were carefully removed from the glass molds, immersed in 5 mL of 50 mM phosphate buffer, pH 7.4, and incubated at 37 °C in a shaking water bath. Samples of 1000 µL were withdrawn at regular time points and replaced with fresh buffer. The samples were stored at 4 °C until completion of the release experiment. The amount of released FD (λ_{ex} = 485 nm and λ_{em} = 510 nm) was determined on a fluorescence microplate reader (BMG LABTECH, Ortenberg, Germany) using standard calibration curves. The amount of released bevacizumab

(λ_{ex} = 280 nm and λ_{em} = 335 nm) was determined on a PerkinElmer LS 55 Fluorescence spectrometer (Perkin Elmen, Weisbaden, Germany) using a standard calibration curve.

3.2.1.3 Results and discussion

Rheological characterisation consisted in stress sweep test, aimed at the determination of the extension of the linear viscoelastic field, and frequency sweep test devoted to determine the mechanical spectrum, the shear modulus (G) and, thus, the average mesh size (ξ_{RHEO}) (Figure 3.34A, B). The stress sweep shown in Figure 3.34A indicates a broad linear viscoelastic region of 10% (w/v) 8armPEG10k hydrogels.

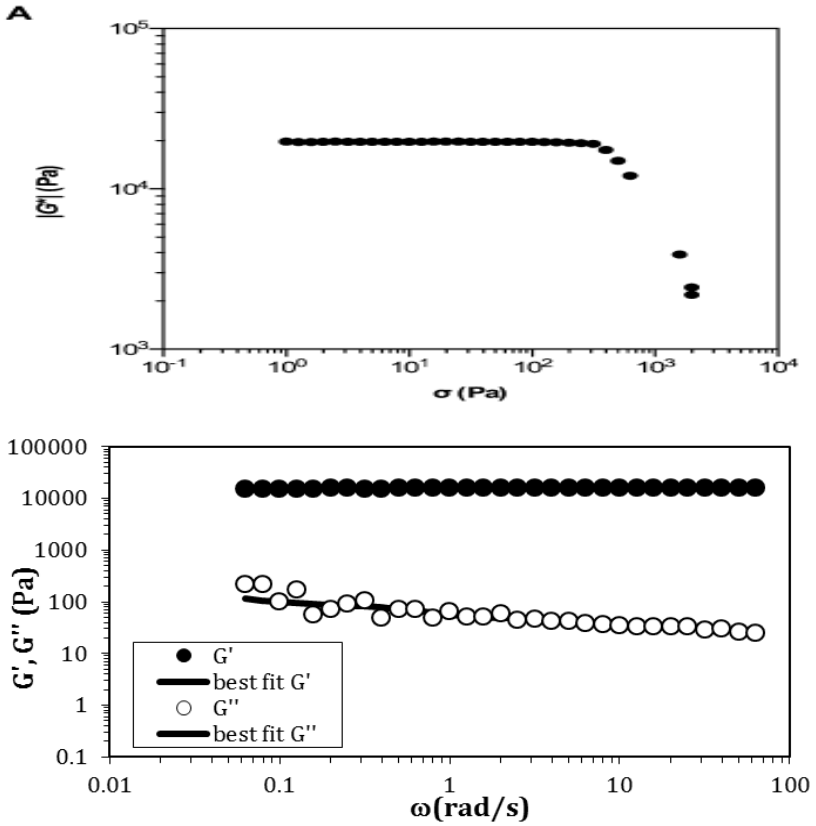

Figure 3.34 Rheological characterization on 8armPEG10k-hydrogel **A:** Stress Sweep test, the absolute value of the complex shear modulus (G^*) vs oscillatory stress (σ). and **B:**Frequency sweep test, elastic (G' closed circles)and shear (G'' open circles)moduli vs oscillatory frequency, the solid lines represent the best fitting of eqs2.10 and 2.11

The absolute value of the complex shear modulus (G^*) was independent from the applied oscillatory stress (σ) between 1 and 200 Pa. The subsequent frequency

sweep experiments (σ = 79.5 Pa) were run within the linear viscoelastic region of the hydrogels. As shown in Figure 3.34B, 10% (w/v) 8armPEG10k hydrogels are strong, fully elastic hydrogels. The storage modulus (G'), which represents the elastic portion of the hydrogel, was 2 orders of magnitude higher than the loss modulus (G''), which represents the viscous portion of the hydrogel. Moreover, both G' and G'' were virtually independent from the angular frequency (ω), which is characteristic for covalently cross-linked, permanent hydrogels. The determination of the average mesh size (ξ_{RHEO}) implied the generalized Maxwell model (eqs.2.10 and 2.11) fitting to experimental frequency sweep data of Figure 3.2.2B. The simultaneous fitting of eqs2.10, 2.11 to the experimental data of G′ and G″ was performed assuming that the relaxation times (λ_i) are scaled by a factor of 10. Hence, the parameters of the model are G_i, G_e, and λ_1. Based on a statistical procedure (chapter 2), the number of Maxwell elements (n) was selected in order to minimize the product $\chi^2 \cdot (n + 2)$, where χ^2 is the sum of the squared errors. In this case, n = 4 Maxwell elements were necessary. The shear modulus (G) could be calculated from the sum of all elastic contributions by $G = G_e + \Sigma G_i$ = 15'988 ± 9'508 Pa (see Tab 3.2-1).

Table 3.2-1 Parameters relative to Maxwell's model best fitting to the experimental data shown in Fig. 3.2.2B. Ge, G1, G2, G3 and G4, are the spring constants of the generalized Maxwell model, λ_1 is the relaxation time of the first viscoelastic Maxwell element, while F(5,35) indicate the F-test results about the statistical acceptability of data fitting

G_1 (Pa)	G_2 (Pa)	G_3 (Pa)	G_4 (Pa)	G_e (Pa)
48±3	58±4	103±13	227±42	15'551±9'508
λ_i	**F-test (5,35)<**			
0.029 ± 0.004	63			

Knowing the shear modulus, the Flory theory (eq.2.13) allows to estimating the crosslink density ρ_x=6.2*10^{-6} ± 3.7*10^{-6} mol/cm^3. Finally, the "equivalent network" approach allows calculating the average mesh size ξ_{RHEO}=8 ± 2 nm according eq.2.22.

In order to estimate the statistical distribution of ξ, LF-NMR measurements were performed. Transverse relaxation time (T_2) was measured over 24h, starting from the time point of gelation preparation; however no significant changes in T_2 are

recorded. Thus, it is conceivable that a physical gel is formed initially, which is the reinforced by chemical cross-links. The discrete distribution of T_2 was determined by fitting eq.2.34 to the relaxation data. Two different relaxation times were identified, with T_{21} longer and more abundant one, and T_{22} shorter and least abundant one. The determined T_{2i} values and their relative weights, A_i, are reported in table 3.2-2.

Table 3.2-2 Transverse relaxation times (T_{2i}) of protons of water molecules entrapped in polymer meshes; A_i represent the relative weights of T_{2i}. The reported T_{2i} values represent the average of all measurements performed during 24 h.

T_{21} (ms)	2568 ± 96	T_{22}(ms)	603 ± 109
A_1 (%)	91±2	A_2 (%)	9 ± 2

Relying on the Sherer theory (section 2.1.6.2) the mesh size of the ideal network, ξ_{IDEAL}, could be calculated. Knowledge of polymer volume fraction (ϕ=0.082) and fiber radius (R_f=0.51), allows, via eq 2.24, the evaluation of ξ_{IDEAL} (fiber cell model, section 2.2.2.2). According to this theory, the knowledge of the average of the inverse relaxation time of the water protons entrapped within the polymer network, $<1/T_2>$, with the relaxation time of protons of bulk water, T_{2H2O}, and ξ_{IDEAL} allows the determination of the relaxation sink strength, $\langle\mathcal{M}\rangle$ ((7±1.2)*10^{-10} m/s) Hence, by knowing T_{2i} and $\langle\mathcal{M}\rangle$, ξ_{iNMR} can be calculate for each class of network meshes by eq.2.43. Using this strategy, the ξ_{iNMR} values of 10%(w/v)8armPEG10k-hydrogels were estimated. The value of ξ_{1NMR}, which represents about 91% of all network meshes, has been found to be 11.±2.1 nm. The remaining 9% representing by ξ_{2NMR} is 0.95 ±0.26 nm. The weighted average mesh size, $\xi_{avg-disc} = 100\%/\big((A_1/\xi_{1NMR}) + (A_2/\xi_{2NMR})\big)$ is 5.36 nm (Table 3.2-3).

Table 3.2-3 Estimated values for the two network meshes ξ_{1NMR} - ξ_{2NMR}, and the average mesh size $\xi_{avg\text{-}disc}$

ξ_{1NMR} (nm)	ξ_{2NMR} (nm)	$\xi_{avg\text{-}disc}$ (nm)
11.±2.1	0.95 ±0.26	5.36

To evaluate the continuous distribution of mesh size, the relaxation time distribution, $a(T_2)$, is determined by fitting eq.2.45 to the relaxation data. The

result reveals the presence of two peaks occurring at relaxation times similar to T_{21} and T_{22} respectively (Figure 3.35)

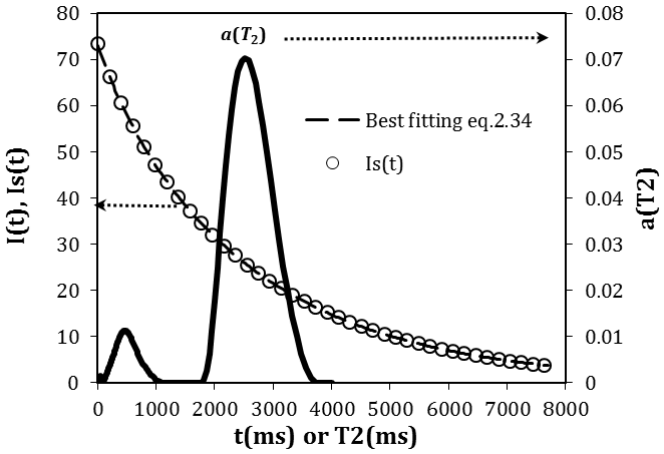

Figure 3.35 Signal intensity, related to the decay of the transverse component of the magnetization vector, vs. time. The open symbols represent the relaxation data, and the dashed line represents the best fit of eq.2.34. The solid line represents the continuous distribution of the relaxation time, $a(T_2)$.

Once $a(T_2)$ or $A(T_2)$ are known, $\langle \mathcal{M} \rangle$ can be derived from eq.2.42, with the only difference that <$1/T_2$> is calculated according to: $\langle 1/T_2 \rangle = \sum_{i=1}^{N}(A_i/T_{2i})/\sum_{i=1}^{N} A_i$. Using eq. 2.43, $A(T_2)$ is converted into the mesh size distribution $A(\xi)$, where $A_i(\xi)=A_i(T_2)$. To allow the comparison of mesh size distributions of different systems, A_i is normalized. As shown in figure 3.36 $A(\xi)$ spanned over three orders of magnitude, meshes as large as 300 nm were observed, even if the probability, A_i, is very low. Two distinct peaks were identified: a small peak at around 1 nm and a larger one at around 10 nm. Interestingly, the proportion between the two peaks matched the result found in the discrete approach (about 9% smaller meshes and 91% larger meshes, table 3.2-2). However, the continuous distribution provided more information than the discrete one. The most abundant mesh size (A_i=5.2%) was found to be ξ_{cont}=9.2 nm, which is in good agreement with the values derived from the other methods (Table 3.2-4). Generally, when the target is the determination of the mesh size distribution, the continuous T_2 distribution is more convenient with respect to the discrete one.

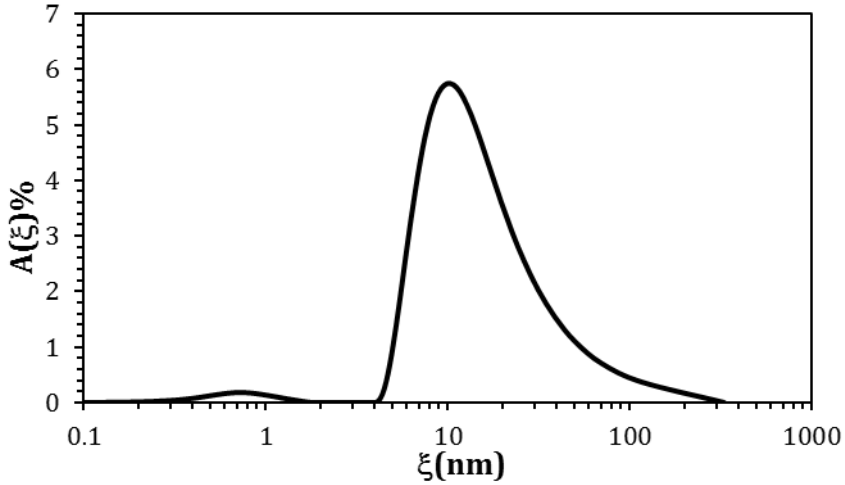

Figure 3.36 Continuous distribution of the mesh size, $A(\xi)$of 10% (W/v) 8armPEG10k hydrogels. The results represent the average of all measurements performed during 24h.

Table 3.2-4 Mesh size of 10%(w/v) 8armPEG10k hydrogels s determined by rheological experiments and low field NMR.

Type of mesh	Method	Determined value (nm)
Average mesh size, ξ_{RHEO}	Rheological experiment	8.0
Most abundant size, ξ_{1NMR}	LF-NMR (discrete)	11±2.1
Least abundant size, ξ_{2NMR}	LF-NMR (discrete)	0.95 ±0.26
Average mesh size $\xi_{avg\text{-}disc}$	LF-NMR (discrete)	5.4
Most abundant size, ξ_{cont}	LF-NMR (continuous)	9.2

These conclusions are supported by measurements of the water self-diffusion coefficient (D_{H2O}). PGSE studies (section 2.2.3) revealed that two exponential terms are required to properly describe the experimentally determined ratio of A_t/A_0 vs q^2 (see eq.3.3) for every t_d considered (7.6 ms < t_d < 44 ms):

$$A_t = \sum_{i=1}^{p} A_{0i} e^{-q^2 t_d D_i} \; ; q = \gamma g \delta \; ; \; A_0 = \sum_{i=1}^{p} A_{0i} \qquad \text{eq.3.3}$$

where A_t and A_0 are the measured amplitudes of the echo with and without the gradient applied, γ is the gyromagnetic ratio of protons, g is the known magnetic field gradient, and A_{0i} are the fraction of water molecules characterized by a self-diffusion coefficient D_i.

Figure 3.37A shows the existence of two species of water molecules with different mobility. The fastest species is characterized by a self-diffusion coefficient of $D_1 \approx 2.7*10^{-9}$ m^2/s, which is close to the self-diffusion coefficient of free water at

37°C (D_{H2O}=3.04*10^{-9} m^2/s) (Holz et al., 2000) and represents about 94% of all water molecules. The slowest specie is characterized by D_2≈5.4*10^{-10} m^2/s and represents the remaining 6% of water molecules (Figure 2.37B).

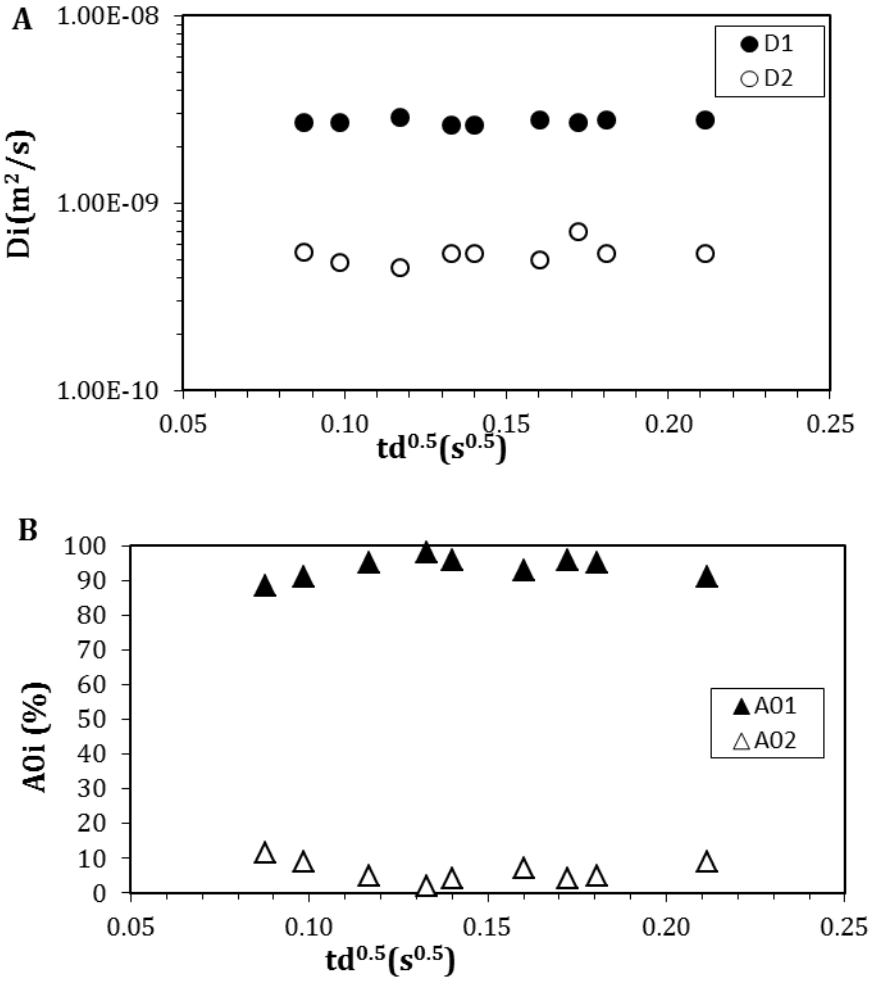

Figure 3.37 A High (D_1) and low (D_2) self-diffusion coefficients of water molecules versus the square root of the diffusion time, t_d. **B** A_{01} and A_{02} represent the relative abundance of the fast and slow diffusing species, respectively.

While D_1 is connected to the existence of wide network meshes (with respect to the size of water molecule), D_2 is most likely due to the presence of narrow meshes that significantly hinder the diffusion of water molecules. Interestingly, these findings exactly match the results of T_2 measurements (tables 3.2-2, 3.2-3). Moreover, it is worth mentioning that, as D_1 and D_2 are essentially independent from t_d, both wide and narrow meshes are interconnected (Momot and Kuchel, 2006). Indeed, at long diffusion times in a system made up isolated meshes (not interconnected) the apparent diffusion coefficient (D_{app}) would become zero.

However in well connected meshes, D_{app} approaches finite non-zero value for an infinite diffusion time (Stait-Gardner et al., 2009).

To correlate the determined mesh size with release profiles, the *in vitro* release of macromolecules from DA hydrogels was investigated. Fluorescein isothiocyanate-labeled dextrans (FDs) were used as model compounds. Four different molecular masses (4, 20, 150 and 500 kDa), with respectively increasing hydrodynamic radius R_h (nm)= 1.8, 3.7, 8.9 and 15.1 were studied. Release tests proved the accuracy of our ξ_{cont} estimation. Indeed, as shown in Figure 3.38, FDs with $2R_h$ smaller than ξ_{cont} (FD4 and FD20) are free to diffuse throughout the gel, and release profile is very fast.

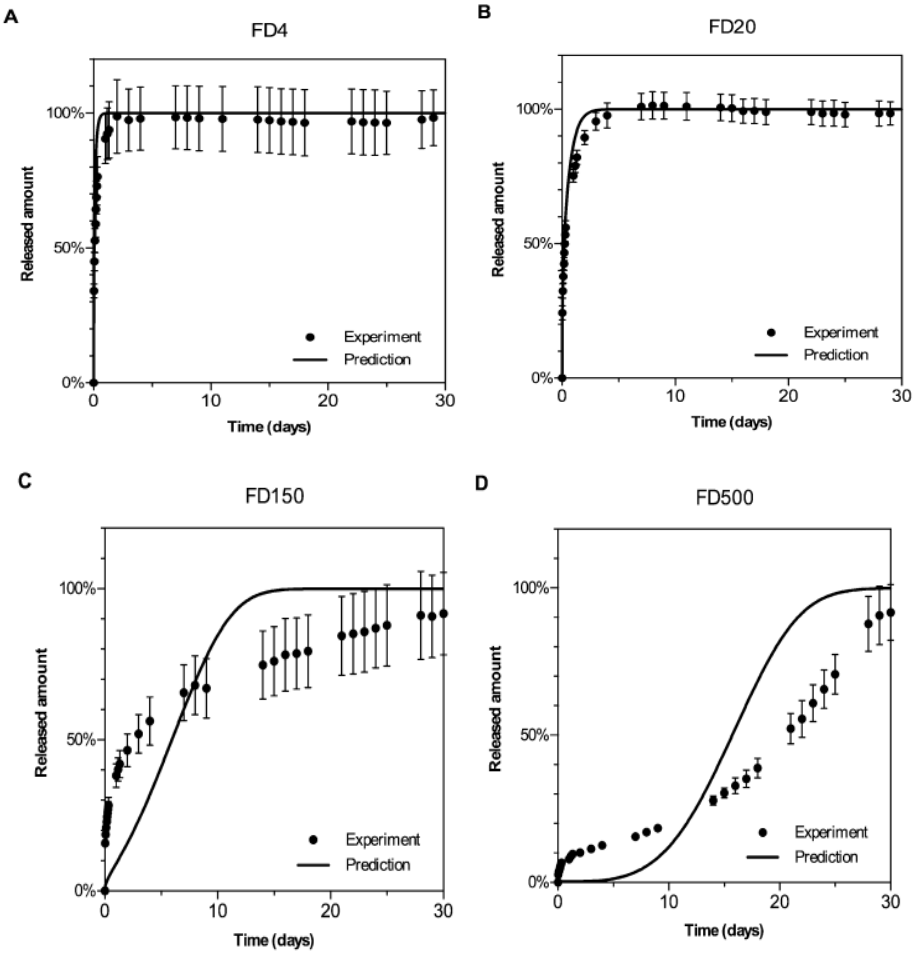

Figure 3.38 Release profile of dextran probes (FD) with four different molecular mass. Experimental data are represented by filled circles while solid lines indicate the best fitting of an interpretative model based on Fick's law (section 2.3).

On the contrary, FD150 and FD500 releases are considerably slower, even if, in these case, profiles present an initial "burst" release probably due to the existence of larger meshes ($\xi > 2R_h$), but the continued existence of smaller meshes may delay the terminal phase of release. Also, this mesh size distribution finds agreement in our NMR results, where ξ_{cont} spans from 0.3 to 300 nm.

In the light of biomedical application, the profiles of FDs are compared with bevacizumab release rate. This is a monoclonal antibody with an R_h=6.5 nm, hence the release from DA hydrogel should be comparatively fast: it should fall between those of FD20 and FD150. Actually, experimentally determined release profile, significantly, differs from compared FDs (Figure 3.39).

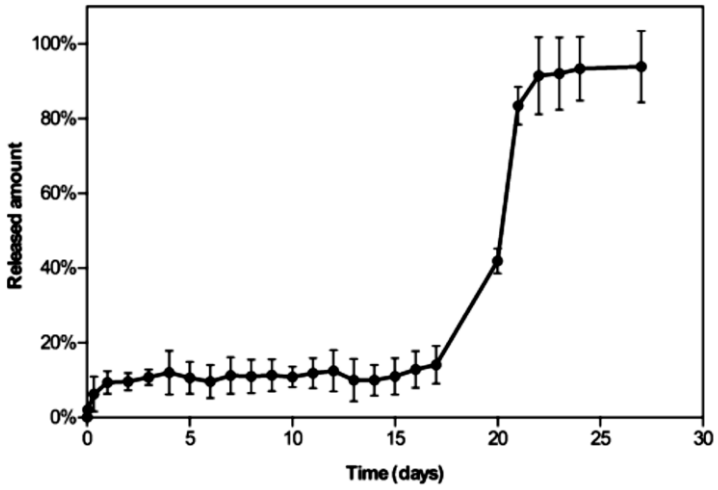

Figure 3.39 Release of bevacizumab from DA hydrogels. Data is expressed as mean ± standard deviation of 3 samples.

Approximately 10% of the incorporated bevacizumab is released after 24h and this was attributed to non-trapped protein located at the surface of the gel. Until 16th day no further release occurred, meaning that antibodies are trapped within hydrogel meshes. Between day 17 and 22, since ξ was increasing during degradation process, the incorporated bevacizumab was completely released. This discrepancy in release profiles could be explained by the different molecular configuration of dextran and protein molecules. The first is a flexible polymer, while proteins are globular and rigid molecules. As a consequence, FDs are able to pass through pores smaller than molecules itself, whereas the globular structure and rigidity of the protein delays bevacizumab release.

In conclusion, both methods (rheological and NMR experiments) gave similar estimates of the network mesh size, which combined with the hydrodynamic radius of the drug molecule, could be used to predict drug release over the time. When R_h is smaller than ξ_{avg}. the predicted release profile matched the experimentally determined release profile very well. However, deviation from theoretical predictions are observed when R_h is similar or grater than ξ. These deviations are most likely due to the statistical distribution of ξ in the real polymer network. Obtained results should promote the benefit from the established correlation between ξ and the release rate for a more rational designed of controlled release system for antibodies.

3.2.2 Physical characterization of photocrosslinked poly(vynil pyrrolidone) (PVP) and PVP-alginate hydrogels for micro-drug delivery systems

3.2.2.1 Introduction

Oral delivery is still the preferred administration route even if a series of drawbacks (drug solubility, permeability and stability) can limit the bioavailability of drug molecules (Wilson and al., 2013), this reflecting in frequent administrations in order to maintain an efficient therapeutic action. An emerging approach is given by the downscaling of drug delivery systems to very small dimensions, which at the same time can allow a more intimate contact with the irregular surface of the mucosa and avoid unspecific endocytosis (Caldorera and Peppas, 2009). In particular, there has been an increasing interest in reservoir based micro-devices (Chirra and Desai, 2012) for carriers of water insoluble compounds and fragile biomolecules. These micro-devices are designed to provide protection against drug degradation, cyto-adhesion and unidirectional drug release. Previous works presented a reproducible approach aimed at micro-containers drug loading for the oral delivery of a poorly water soluble compound (Marizza et al., 2014). An inkjet printing was used to dispense water based solutions of poly(vinyl-pyrrolidone) (PVP) in water with precise volumes in the

pico- up to nano- litre range into micro-containers (Marizza et al., 2013). PVP is a neutral and amphiphilic polymer (figure 3.40) which exhibits high solubility both in water and many organic solvents (Cooley et al., 2009) and is widely used as excipient for oral dosage forms (Lee et al., 2017).

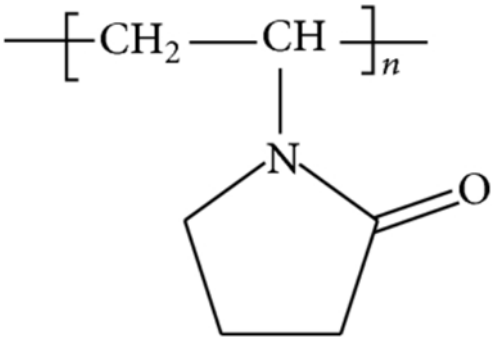

Figure 3.40 Chemical structure of poly-vynilpyrrolidone

PVP K30 and K90 (respectively, medium and high molar weight) can be crosslinked by exposure to UV radiation (Fechine et al., 2014), giving a water insoluble gel material which swells in water. The crosslinking induced by UV radiation follows a radical mechanism (Fouassier and Lalevée, 2012) activated by a photoinitiator. It is well known that, in many case, the biocompatibility of photo-initiators is a critical issue ad most of them are cytotoxic (Williams et al., 2005) even if, recently, an UV crosslink on aqueous solution of PVP was obtained without initiator (Lopergolo et al., 2003). The same authors added hydrogen peroxide (H_2O_2) to PVP solution as crosslinking agent increasing portion of polymer fixed in the network after radiation, up to 90%

I have already had the opportunity to stress the importance of crosslink density as it determines the polymeric network mesh size, which, in turn, reflects on the drug mobility inside the hydrogel. Hence, the determination of this parameter is of paramount importance for the control of drug release kinetics (Marizza et al, 2016). In collaboration with the department of micro- and nanotechnology of the Technical University of Denmark (Lyngby, Denmark) I developed a study focused on:

i) the characterization of PVP photocrosslinked hydrogels with particular care to the effect of irradiation time, polymer concentration photo-initiator concentration.

ii) the improvement of hydrogel rheological properties by PVP blending with alginate in order to obtain an Interpenetrated Polymer Network (IPN) (Matricardi et al., 2013).

To this purpose, I combined complementary analyses including rheology, low field nuclear magnetic resonance spectroscopy (LF-NMR) and Transmission Electron microscopy (TEM) to estimate the polymer mesh size of the gels prepared under different conditions.

3.2.2.2 Material

Poly(vinylpyrrolidone) (PVP K90, Mw $3.6*10^5$ Da), hydrogen peroxide (H_2O_2) aqueous solutions (30 wt%) and deuterium oxide (>99.9% isotopic purity) were supplied by Sigma Aldrich. Water was deionized (DI). All the employed solvents were degassed before preparation of the solutions.

For hydrogel preparation, the PVP powder is dissolved in mixtures of DI water (99.1%v/v) and H_2O_2 (0.9%v/v), with polymer concentration of 10, 20, and 30 w/v% under stirring (250 rpm) at 50°C for 36 h. Even at the highest concentration, PVP was perfectly dissolved, resulting in high viscous and transparent solutions. For the rheological and the LF-NMR investigations, macroscopic specimens of the hydrogel were prepared. To investigate the influence of the initiator concentration on the structural properties, additional 30%PVP solutions were prepared with double and triple amounts of H_2O_2 (referred to as 30%+2H and 30%+3H). From preliminary photocrosslinking tests performed on layers of different thickness, it was found that gels thicker than 1 mm exhibit a macroscopically inhomogeneous structure with a softer texture at the bottom and a more elastic one on the top. Gels thinner than 1 mm, were very fragile and unpractical to handle. As a consequence, a fixed thickness of 1 mm was used.

Solutions were cast into cylindrical moulds (1 mm in depth, 15 mm in diameter) and 0.5 mm thick glass discs were clamped onto the mould to prevent water evaporation during the UV exposure. It was verified that the glass absorbs a negligible amount of the radiation emitted by the UV lamps. Considering an emitted power density of 29 mW/cm2, each sample was exposed to 67, 100, and 134 J corresponding to irradiations for 22, 33, and 44 min, respectively. After

photo-crosslinking, gels were separated from the mould with a spatula and dipped in DI water under stirring to extract unreacted polymer and photo-initiator (washing). The crosslinked polymer volume fraction after washing was ϕ_0. Gels were, then, let to swell in water for 24 h and the polymer volume fraction went down to ϕ. After swelling, the superficial water on the gels was removed.

Alginate (molecular weight ≈ 10^6 Da), a kind gift from FMC Biopolymer Ltd, UK, was characterized by a high content of guluronic units (70% guluronic and 30% mannuronic). For IPN hydrogel at the starting PVP solutions were added 0.5 w/v% of alginate solution. UV exposition doesn't prompt the crosslink of alginate chains, which was obtained by spraying a $CaCl_2$ solution (Ca^{++} concentration equal to 9 g/l) on gel surface. The gelling solution was let acting for 5 minutes, then samples were gently washed.

3.2.2.3 Results and discussion: I part

Nine PVP hydrogels were studied: three different polymer concentrations (10, 20 and 30% w/v) for three different irradiation time (22=A, 33=B and 44=C minutes). These samples are indicated by 10A, 10B, 10C – 20A, 20B, 20C – 30A, 30B, 30C.

In order to perform a proper sample characterisation it was necessary to preventively evaluate the hydrogel polymer volume fraction in the reference (ϕ_0) and in the swollen (ϕ_p) conditions. Indeed, the preparation procedure implied a washing after crosslinking, which made the estimation of ϕ_0 as well as the PVP volume fraction in the swollen condition (ϕ_p) very difficult. For this purpose, a semi- empirical approach, based on LF-NMR, was designed in order to estimate ϕ_0 and ϕ_p for the different hydrogels studied. This approach was based on the experimental evidence that the average relaxation time (T_{2g}) of a polymeric hydrogel is always lower than the one of the aqueous solutions (T_{2s}) with equal polymer volume fraction. Thus, the hydrogel and the polymeric solution differ only for the different arrangement of the polymeric chains due to the presence of the crosslinks occurring in the hydrogel. It can be assumed that while in a solution the polymeric chains are in a curled configuration with intramolecular and possibly in clusters, in the case of a gel the crosslinks constrain the chains in a three-

dimensional network, where the polymer configuration is less curled and the surface accessible to water is higher. Based on these assumptions, the curled state implies a reduced surface area (S) of the polymer/water interface that is the key point for the determination of the water protons relaxation time. The original Chui theory (Chiu et al., 1995) states:

$$R_h = \frac{2V}{S} \; ; \; \left\langle \frac{1}{T_2} \right\rangle = \frac{1}{T_{2H2O}} + 2\frac{\langle \mathcal{M} \rangle}{R_h} \qquad \text{eq.3.4}$$

where R_h is the hydrodynamic radius while V is a volume proportional to the solvent (water in our case) volume fraction ($1-\phi_p$) in the gel. While V weakly depends on the conformation assumed by the polymeric chain (Mahabadi and Rudin, 1979), S is strongly dependent on the chains conformation and it will be higher in the case of a linear configuration while it will decrease in the case of curled chains. Being ϕ_p (polymer volume fraction in the gel) the same, R_h in a gel network will be lower than in a solution. As a consequence, from eq.3.4, it follows that the average value of the inverse of the relaxation time of the gel, $\langle 1/T_2 \rangle_{gel}$, is bigger than the same parameters competing to solution, $\langle 1/T_2 \rangle_{sol}$, being $\langle \mathcal{M} \rangle$ and free T_{2H2O} the same for both systems (hydrogel and solution). Thus, $T_{2gel} < T_{2sol}$. As for a hydrogel, eq.(3.4) can be re-written as:

$$\left\langle \frac{1}{T_2} \right\rangle_{gel} = \frac{1}{T_{2H2O}} + \frac{2\langle \mathcal{M} \rangle}{R_f} \frac{{\phi_p}^n}{1-0.58{\phi_p}^n} \qquad \text{eq.3.5}$$

I assumed that, for a solution, the following relation holds (Marizza et al., 2016):

$$\left\langle \frac{1}{T_2} \right\rangle_{sol} = \frac{1}{T_{2H2O}} + \frac{2\langle \mathcal{M} \rangle}{R_f} \frac{{\phi_p}^n}{1-0.58{\phi_p}^n} \qquad \text{eq.3.6}$$

where n is an empirical fitting parameter that is equal to 1 in the case of hydrogels and it has to be greater than 1 in case of solutions in order to yield $T_{2gel} < T_{2sol}$. Accordingly, eq.3.6 was fitted (n and $\langle \mathcal{M} \rangle$ fitting parameters; R_f = 0.91 (Theodoru and Suter, 1985)), to the experimental relaxation data referring to PVP aqueous solutions characterized by different, and experimentally known, polymer volume fractions (ϕ_p) as shown in Figure 3.41 (filled circles). Eq.3.6 fitting to experimental data was statistically reliable, as proved by the F-test ($F(1,16,0.95)<235$), and fitting parameters resulted n = (1.9 ± 0.3) and $\langle \mathcal{M} \rangle$= (7.7 ± 2.9)$10^{-3}$ nm/ms. The knowledge of $\langle \mathcal{M} \rangle$ was used to determine ϕ_p from eq.3.6 as $\langle 1/T_2 \rangle_{gel}$ is known from experimental measurements.

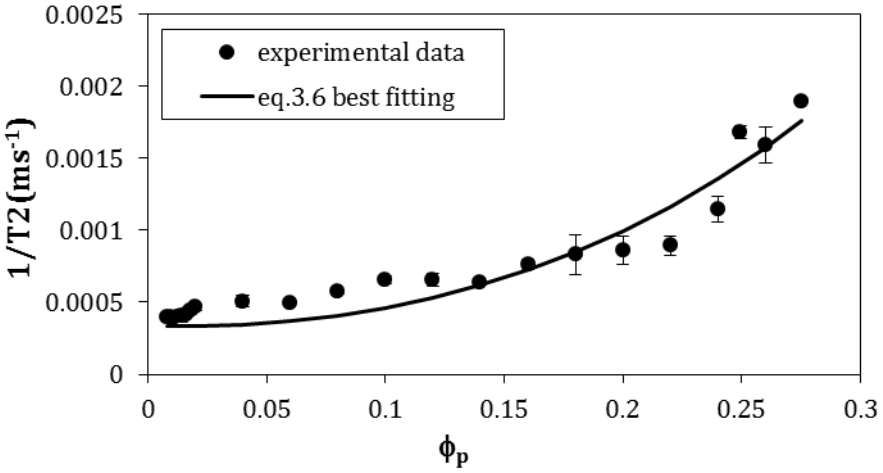

Figure 3.41 Dependence of the inverse of water relaxation time ($1/T_2$) on the PVP volume fraction (ϕ_p) characterizing different PVP aqueous solutions. Dots indicate experimental data while solid line represents eq.3.6 best fitting. Vertical bars indicate SD (N=3).

For the different examined systems, Table 3.2-5 shows the values of ϕ_0 and ϕ_p obtained with this approach. It can be seen that the washing/swelling processes implies a considerable sol fraction, i.e. un-crosslinked portion of the polymer, of the system considered.

Table 3.2-5 Relaxation time (T_2) and polymer volume fraction (ϕ_p) and of the nine gels considered. Each gel is identified by a number indicating the polymer concentration of the originating water solution (10 wt%, 20 wt% and 30 wt%) and a letter indicating the crosslinking time (A=22 min; B =33 min; C =44 min) (N =3).

% PVP	**T_2 (ms)**	**ϕ_p*10^3**	
10_A	2104	8.3 ± 3.2	**ϕ_0*10^3 10%**
10_B	2380	5.1 ± 2.0	8.6 ± 3.3
10_C	2291	6.1 ± 2.3	
20_A	2447	4.4 ± 1.7	**ϕ_0*10^3 20%**
20_B	2328	5.7 ± 2.2	11.4 ± 4.4
20_C	2393	5.0 ± 1.9	
30_A	2451	4.4 ± 1.7	**ϕ_0*10^3 30%**
30_B	2412	4.8 ± 1.8	14.4 ± 5.5
30_C	2489	4.0 ± 1.5	

Rheological tests (25°C; serrated surfaces PP20Ti, diameter = 20 mm; gap-setting optimization was undertaken according to short stress sweep test and gap ranged between 1 and 2 mm) were successfully preformed on all samples. Stress sweep tests revealed (data not shown) that, for all the studied gels, the linear viscoelastic range holds for stresses above the value adopted for the frequency sweep tests (τ=5 Pa).

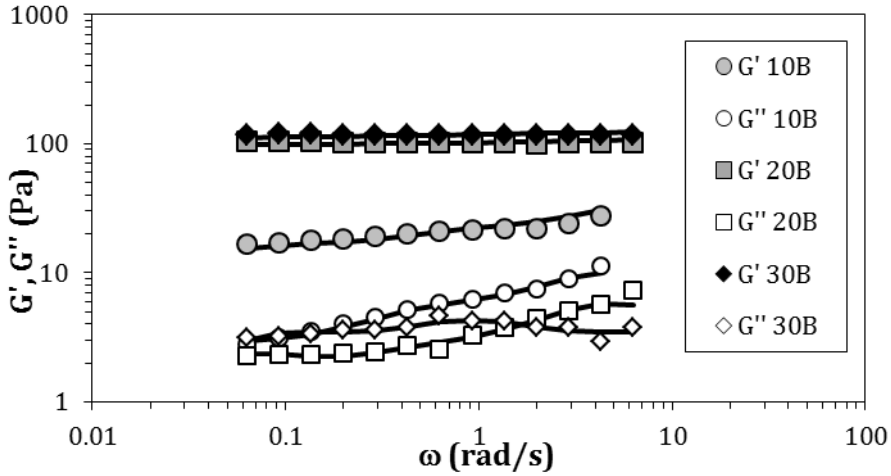

Figure 3.42 Mechanical spectra referring to gels 10B, 20B, and 30B. G' and G'' indicate, respectively, the storage (filled symbols) and loss moduli (open symbols). Continuous lines represent eqs. 2.10 and 2.11 best fitting.

In addition, Figure 3.42 reports the mechanical spectra referring to systems 10B, 20B, and 30B in the swollen state. As for all the three systems, the storage (G') and the loss (G'') moduli are substantially independent from the angular frequency $\omega=2\pi f$ and G' is definitely prevalent over G'', they can be defined as gels. However, the typical gel characteristics (for instance the ratio G'/G'' >10), are much more pronounced passing from 10B to 20B than from 20B to 30B. Notably, in the series 10B to 30B, while G'' is more or less unchanged, G' undergoes an increase of one order of magnitude. It is worth notice that while G' increases with the concentration of the originating polymeric solution (10, 20, 30% wt), the polymer volume fraction ϕ_p corresponding to these systems is almost the same (see Table 3.2-5). Thus, the increase of the polymer concentration of the initial polymer solution does not entail an increase of the gel fraction: reasonably, the number of polymeric chains involved in the crosslinking reaction remains constant whilst an increase of initial PVP concentration or of irradiation time produces more

crosslink points among a stable number of polymeric chains. Table 3.2-6, showing the crosslink density, ρ_x, regarding gels 10-B, 20-B and 30-B, seems to confirm this hypothesis. Three Maxwell elements plus a purely elastic element (G_e) were needed for a statistically reliable fitting of the frequency sweep data shown in Figure 3.42. The data fitting reveals also that the average mesh size (ξ_{RHEO}) of these gels ranges between 65 and 48 nm, where 10-B gel exhibits the highest ξ_{RHEO}.

Table 3.2-6 Crosslink density (ρ_x), shear modulus ($G=\Sigma G_i$), average mesh diameter ξ_{RHEO} (nm), and generalized Maxwell model fitting parameters (λ_1, G_1, G_2,G_3 and G_e) relative to gels 10B, 20B, and 30B.

	10B	**20B**	**30B**
ρ_x(mol/cm^3)	$(12 \pm 4)10^{-9}$	$(28 \pm 10)10^{-9}$	$(25 \pm 9)10^{-9}$
***G*(Pa)**	42 ± 4	113 ± 13	126 ± 7
ξ(nm)	64 ± 8	48 ± 6	50 ± 6
λ_1(s)	0.19 ± 0.09	0.19 ± 0.02	0.11 ± 0.5
***G*$_e$**	12.9 ± 1.7	95.5 ± 8.0	109 ± 7
***G*$_1$**	18.5 ± 2.6	11.0 ± 8.0	5.3 ± 1.1
***G*$_2$**	6.4 ± 2.1	2.6 ± 1.8	6.5 ± 1.1
***G*$_3$**	4.0 ± 1.2	3.9 ± 0.9	5.3 ± 1.1
***F*(4,19,0.95)<**	36.2	44.1	64.8

The analysis of gels 10A, 10C, 20A, 20C, 30A, and 30C led to similar conclusions (data not shown). Figure 3.43 sums up the results of the characterization of gels 10ABC, 20ABC, and 30ABC by showing the trend of the shear modulus ΣG_i. It is evident that G increases both with the crosslinking time (horizontal axis) and with the increase of the polymer concentration (10%, 20%, 30%), that also translates higher crosslink density, ρ_x, and correspondingly, smaller average mesh size, ξ_{RHEO} (Table 3.2-6). It is interesting to notice that, for the "C" gels, the increase of ΣG_i, in the series 10-20-30, is more pronounced than those of the "A" and "B" gels.

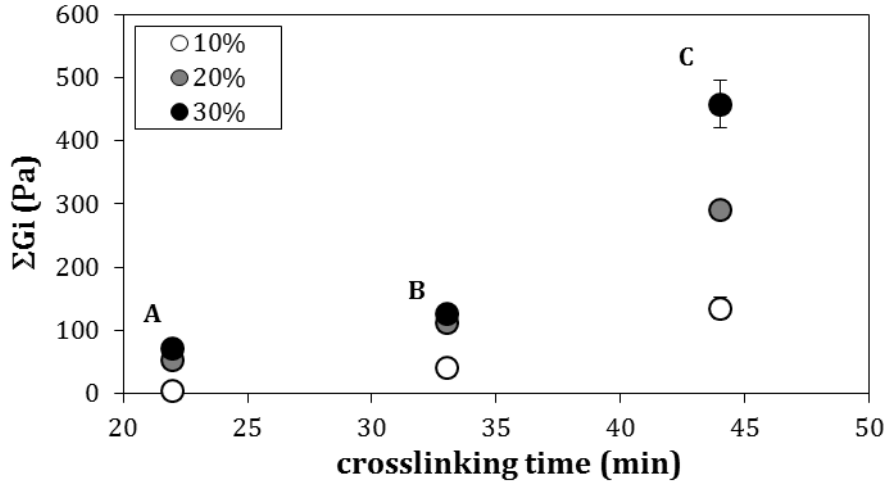

Figure 3.43 Shear modulus, ΣG_i, dependence on UV irradiation time for gels characterized by at different [PVP] concentration (10-, 20- and 30 %). Vertical bars indicate SD (N=3).

Figure 3.44 shows the results of the frequency sweep tests related to systems characterized by an increasing initial concentration of photo-initiator (H_2O_2; 1H, 2H, 3H). In particular, the attention is focussed on 30B, 30B-2H and 30B-3H gels. These samples clearly belong to the viscoelastic class of gels as *G*' independent on pulsation ω, *G*'' is weakly dependent and *G*' is neatly prevailing on *G*''. Substantially, the increase of the H_2O_2 amount reflects into an increase of *G*' whereas *G*'' is almost constant.

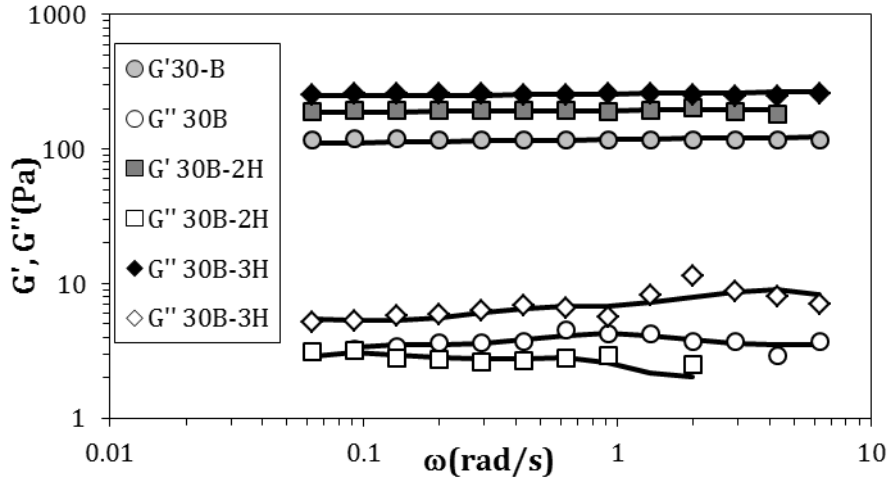

Figure 3.44 Mechanical spectra referring to gels 10B, 20B, and 30B. G′ and G″ indicate, respectively, the storage (filled symbols) and loss moduli (open symbols). Continuous lines represent eqs. 2.10 and 2.11 best fitting.

The increase of *G*' with the H_2O_2 concentration is more gradual than in the case of the increase of the originating polymeric solution (see Figure 3.42). Two/three

Maxwell elements plus a purely elastic element (G_e) were needed for a statistically reliable fitting of the frequency sweep data shown in Figure 3.44 (see Table 3.2-7).

Table 3.2-7 Crosslink density (ρ_x), shear modulus (ΣG_i), average mesh diameter ξ_{RHEO} (nm), and generalized Maxwell model fitting parameters (λ_1, G_1, G_2,G_3 and G_e) relative to gels 30B, 30B-2H, and 30B-3H.

	30B	**30B-2H**	**30B-3H**
ρ_x(mol/cm^3)	(25 ± 9)10^{-9}	(34 ± 12)10^{-9}	(69 ± 25)10^{-9}
ΣG_i(Pa)	126 ± 7	195 ± 8	275 ± 16
ξ(nm)	50 ± 6	45 ± 5	36 ± 4
λ_1(s)	0.11 ± 0.5	1.33 ± 0.3	0.22 ± 0.06
G_e	109 ± 7	186 ± 8.0	242 ± 16.0
G_1	5.3 ± 1.1	4.4 ± 0.6	16.0 ± 2.0
G_2	6.5 ± 1.1	5.1 ± 0.7	8.4 ± 2.1
G_3	5.3 ± 1.1	/	8.5 ± 2.1
F(4,19,0.95)<	64.8	243.0	65.0

From Table 3.2-7 it can be noticed that the increase of the H_2O_2 concentration corresponds to an increase of the crosslink density (ρ_x) and a consequent decrease of the average mesh size (ξ_{RHEO}). Qualitatively similar conclusions can be drawn for the gels 30A, 30A-2H, 30A-3H, 30C, 30C-2H and 30C-3H.

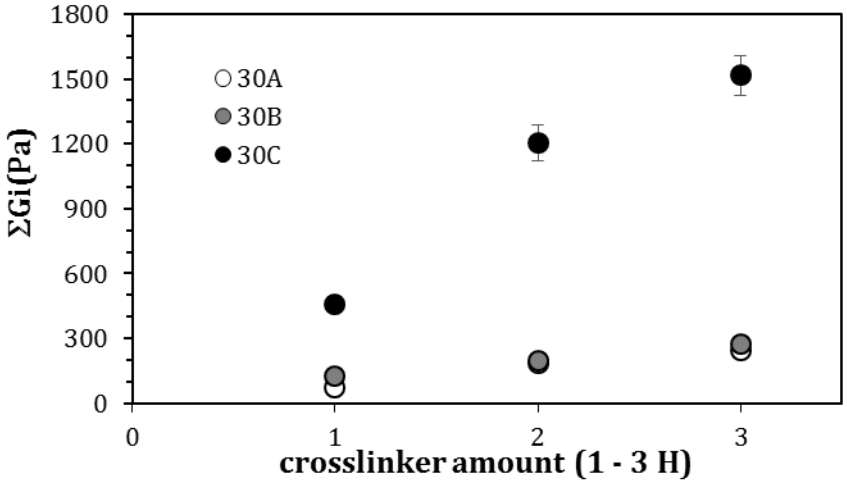

Figure 3.45 Dependence of the shear modulus ΣG_i(Pa) on the crosslinker amount (1H, 2H, 3H) relative to gels 30A, 30B, and 30C. Vertical bars indicate SD (N = 3).

Figure 3.45 shows the trend of the shear modulus ΣGi with the H_2O_2 amount of the 30% PVP gels with different H_2O_2 concentration. For all these gels, ΣGi increases with the photo-initiator content and this trend is maximised for the 30C series.

LF-NMR analysis revealed that all the studied gels are characterized by only one relaxation time (T_2) (see Table 3.2-5). This means that all the hydrogels are homogeneous systems, i.e. all the water molecules interact with the polymeric chains in the same manner. Consequently, in the light of the Scherer´s theory (Sherer, 1994), these gels are characterized by meshes of similar dimensions. On the contrary, the highly heterogeneous gels, such as those prepared from alginate, up to four relaxation times can be found (Abrami et al., 2014). Relying on T_2 measurements, on the theory shown in chapter 2 and on the PVP radius R_f = 0.91 nm (Marizza et al., 2016), it is possible estimating the average mesh size (ξ_{NMR}) of our hydrogels as shown in Table 3.2-8.

Table 3.2-8 Water self-diffusion coefficient (D_g) and average mesh size (ξ_{NMR}) referring to the studied gels.

GEL	ξ_{NMR} (nm)	D_g(m^2/s)*10^{-9}
10_A	31 ± 6	2.26±0.04
10_B	39 ± 7	2.23±0.07
10_C	36 ± 7	2.25±0.05
20_A	42 ± 8	2.26±0.01
20_B	37 ± 7	2.22±0.02
20_C	40 ± 7	2.12±0.04
30_A	42 ± 8	2.20±0.05
30_B	40 ± 8	2.20±0.05
30_C	44 ± 8	2.10±0.05
30-A-2H	37 ± 7	2.20±0.06
30-B-2H	43 ± 8	2.20±0.06
30-C-2H	40 ± 8	2.10±0.04
30-A-3H	33 ± 6	2.20±0.06
30-B-3H	33 ±6	2.20±0.12
30-C-3H	34 ± 6	2.20±0.06

It can be noticed that ξ_{NMR} is almost constant and spans from 31 nm to 44 nm. These high values are comparable with the evaluation of the water self-diffusion coefficient (D_g) in the gels. Indeed, for all gels, D_g is very close to the value of the free water self-diffusion coefficient at 25°C ($2.3*10^{-9}$ m^2/s (Holz et al., 2000)). This means that the hindering action exerted by polymeric chains on water molecules diffusion is very weak as occurs with gels characterized by wide meshes.

In order to have more insight about the studied gels, Small Angle X ray Scattering (SAXS) was considered. A collimated beam, with a wave-length λ = 0.1542 nm, was irradiated through a vacuum sealed cell containing the gel sample. The scattered field was then detected with a 2D camera, which allowed the evaluation of the diffracted intensity down to q = 0.1 nm^{-1}. While q is the scattering vector defined as $q = (4\pi)*\sin(\theta)/\lambda$, θ is the angle between the incident and the scattered field. Intensities were collected at room temperature for 30 minutes. Raw data were corrected for dark current and background and then normalized with respect to the primary beam intensity. A further correction for both Porod constant and the de-smearing effect was applied and the results were plotted as Iq^2 vs q. SAXS analysis revealed that, in the investigated range of scattering vector q, experimental data do not display any significant order length. Indeed, the features, reported in Figure 3.46 (referring, for example, to gel 20-B), are more typical of a semi-flexible random coil.

In order to interpret the SAXS datasets, the worm like chain (WLC) model (Kratki and Parod, 1949) was adopted. In this model, the polymeric chain is characterized by two characteristic lengths: the contour length (L) and the persistence length (l_p). In the limit of $L >> l_p$, the following relationship exists between the scattering intensity $I(q)$ and the scattering vector q:

$$\frac{I(q)}{I(0)} = 2u^{-2}[exp\{-u\} - 1 + u] + \frac{l_p}{L}\left[\frac{4}{15} + \frac{7}{15u} - \left(\frac{11}{15} + \frac{7}{15u}\right) exp\{-u\}\right] \quad \text{eq.3.7}$$

where:

$$u = \frac{L l_p q^2}{6} \quad \text{eq.3.8}$$

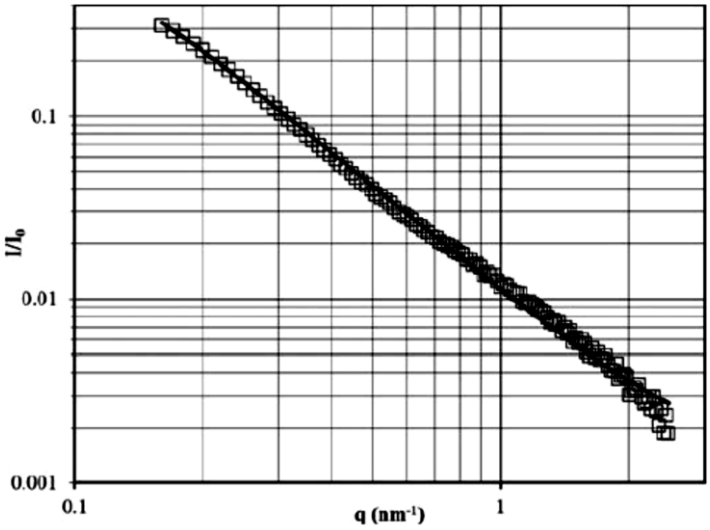

Figure 3.46. Scattering intensity I/I_0 versus the scattering vector q relative to gel 20B. Empty squares represent experimental points; the black line is related to the model.

Eq.3.7 best fitting to experimental data shown in Figure 3.46 yields to the following values of the two lengths: L = 547 nm, l_p = 2.13 nm. These values are compatible with the average mesh size found. Indeed, the value of L implies that, on average, each polymeric chain is involved in about 10 – 20 meshes. In addition, the persistence length l_p (rigid chain portion) seems compatible with meshes spanning in the range 30 – 44 nm (see Table 3.2-8)

For a better comprehension of the differences existing between the rheological and the LF-NMR approach, Figure 3.47 shows the comparison between ξ_{RHEO} and ξ_{NMR} for the studied gels: 10A-B-C, 20A-B-C, 30A-B-C. In order to perform a more exhaustive comparison, the horizontal axis reports the shear modulus (ΣG_i) competing to each gels. It can be observed that when ΣG_i exceed about 140 Pa, both methods lead to similar values. However, for smaller G, rheology gives to a larger estimation of the average mesh size. This could be explained by the presence of dangling chains that, being bound to one end of the network, are elastically inactive and, thus, irrelevant for the determination of G and ξ according to the rheological approach (Frankær et al., 2012). On the contrary, for the LF-NMR approach, both elastically active and inactive chains are important. As the number of dangling chains can be roughly connected to the viscous properties of the gel

(*G''*), it is reasonable to say that dangling chains have a smaller and smaller effect when *G* increases. In this case, the *G* threshold appears to be around 140 Pa.

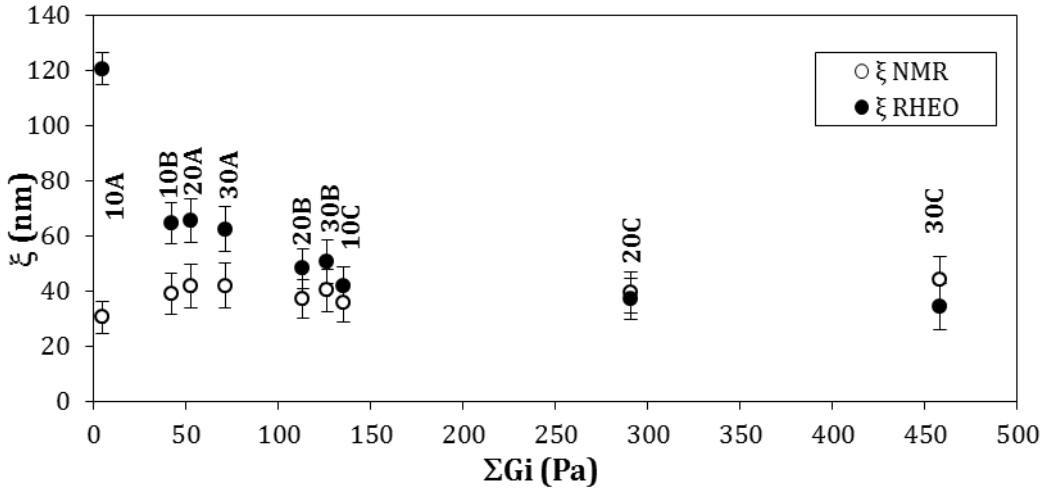

Figure 3.47 Average mesh size evaluated according to the rheology (ξ_{RHEO}) and LF-NMR approach (ξ_{NMR}) for gels 10A-B-C, 20A-B-C, and 30A-B-C. Error bars represent SD (N=3).

These considerations are substantially confirmed by Figure 3.48 reporting the comparison between the average mesh diameters evaluated by means of rheology and LF-NMR for the gels 30A-2H-3H, 30B-2H-3H, and 30C-2H-3H. Indeed, for ΣG_i>100 Pa, the rheological and the LF-NMR approach yield to similar estimation of the average mesh size.

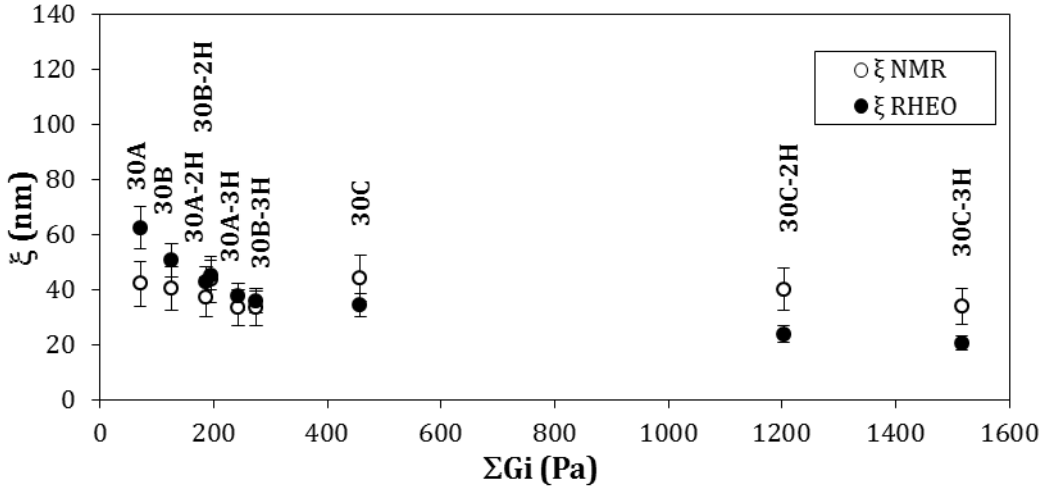

Figure 3.48 Average mesh size evaluated according to the rheology (ξ_{RHEO}) and LF-NMR approach (ξ_{NMR}) for gels 30A-2H-3H, 30B-2H-3H, and 30C-2H-3H. Error bars represent SD (N = 3).

Finally, Figure 3.49 reports the continuous mesh distribution referring to gel 20A (chosen as a representative example of all other gels) determined according to the

LF-NMR approach. It can be seen that the most probable mesh size is around 40 nm while the distribution spans from about 25 nm up to 120 nm.

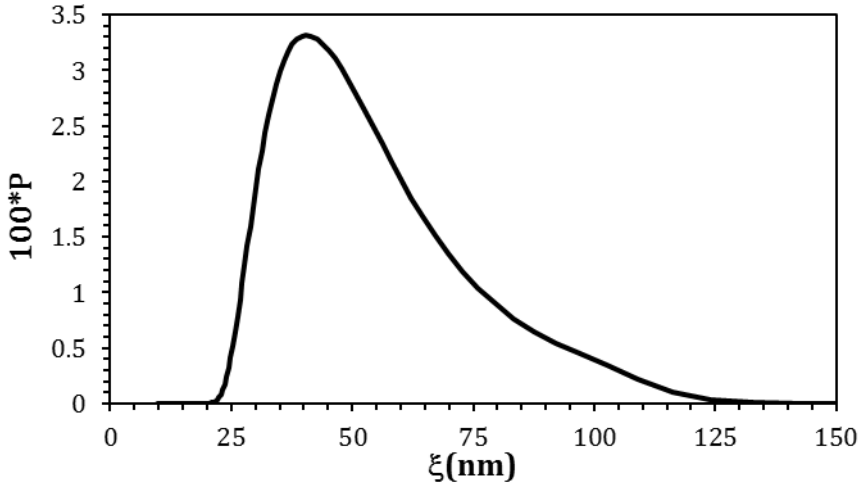

Figure 3.49 Average mesh size evaluated according to the rheology (ξ_{RHEO}) and LF-NMR

Summarizing, UV-crosslinked PVP hydrogels were investigated in order to understand the effects of irradiation dose, polymer and photo-initiator concentrations. Rheology, low field NMR and SAXS were used as characterizing techniques. The comparison of the results, leading to different estimation of the network mesh size, revealed the presence of a complex structure of the hydrogel networks, comprehending more elastically active chains, and an elastically inactive/viscous portion composed by dangling chains, experimentally "invisible" to the rheological measurements. Rheology and LF-NMR converge to similar mesh size values in the stronger hydrogel where elastic response prevails over the viscous one.

3.2.2.4 Results and discussion: II part

In the light of the problems connected to the PVP escape from the hydrogel (see part I), alginate, a widely used polysaccharide in biomedical field, was considered to limit/prevent PVP escape in virtue of the formation of an interpenetrated network PVP/alginate. Alginate is a natural biopolymer derived from brown algae, which can be used to create hydrogels via ionic cross-linking by exposing aqueous alginate to divalent cations (e.g., Ca^{2+}, Ba^{2+}). It has been utilized for many applications, such as tissue engineered constructs (Khattak et al., 2007) delivery

systems (Abrami et al., 2013) and scaffolds for three-dimensional cell culture (Fiorentino et al., 2017).

Alginate addition (0.5% w/v) regarded all the systems previously studied (10A-B-C, 20A-B-C, 30A-B-C). While PVP underwent the usual crosslinking procedure, three different strategies were considered for alginate:

i) alginate was simply added without crosslinking (samples labelled NO_Ret);

ii) Alginate underwent crosslinking by bivalent cations after PVP crosslinking and gel washing for the removal of un-crosslinked PVP (24 hours at 25°C in pure water). As this procedure implied gel swelling, these samples were labelled Swell_Ret. Alginate crosslinking implied gel exposition to a $CaCl_2$, solution (9 g/l of Ca^{++}) for 5 minutes (contact crosslinking).

iii) Alginate underwent crosslinking by bivalent cations after PVP crosslinking but before gel washing. Accordingly, these sample were labelled Ret_Swell. Alginate crosslinking implied gel exposition to a $CaCl_2$, solution (9 g/l of Ca^{++}) for 5 minutes (contact crosslinking).

Rheology characterization revealed that all the studied systems can be defined gels as G' was always >> G'' and, substantially, frequency independent (data not shown). Figure 3.50 summarizes the results of the frequency sweep tests (performed inside the linear viscoelastic field) showing the dependence of the calculated shear modulus (ΣG_i) on PVP crosslinking time and alginate crosslinking strategy. For a better comparison, also the gel without alginate is reported (NO_Alg). The discussion is now focussed on the 20% PVP gels as qualitatively similar results were obtained for the other two PVP concentrations (10% and 30%).

Interestingly, the inspection of Figure 3.50 shows that alginate addition increased the gel mechanical strength (higher shear moduli ΣG_i), but not marked rheological differences emerge upon alginate crosslinking (especially for PVP crosslinking time of 22 and 33 min).

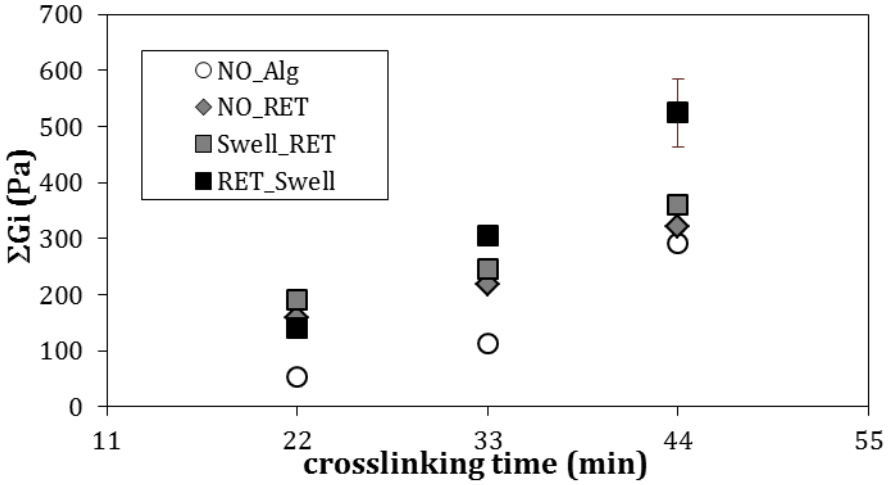

Figure 3.50 Shear modulus, ΣG_i, dependence on crosslinking time, for gels characterized by 20% PVP concentration plus 1) 0% Alginate (NO_Alg), 2) 0.5% alginate concentration without alginate crosslinking (NO_Ret), 3) 0.5% alginate concentration and alginate crosslinking after gel washing (Swell_Ret), 4) 0.5% alginate concentration and alginate crosslinking before gel washing (Ret_Swell). In all systems, PVP underwent crosslinking before alginate crosslinking.

On the contrary, the LF-NMR characterization of the same systems (figure 3.51) reveals that the effect of alginate is truly significant.

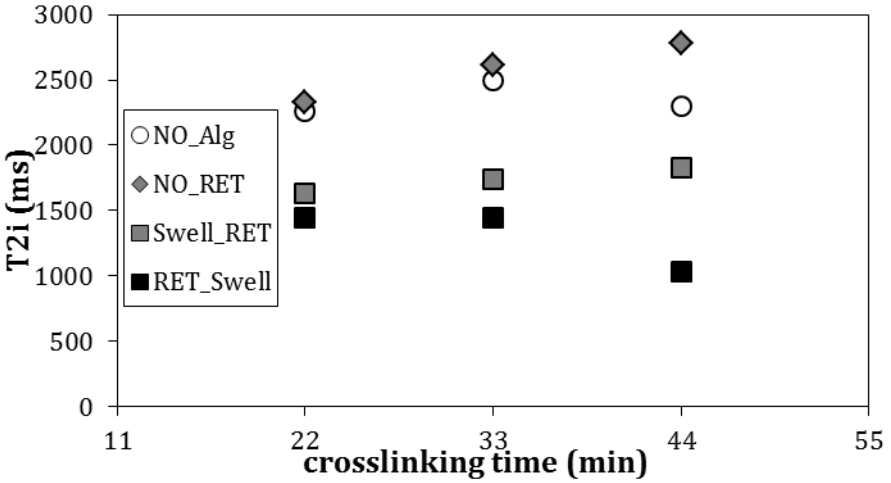

Figure 3.51 Average relaxation time, T_{2m}, dependence on PVP crosslinking time, for gels characterized by 20% PVP concentration plus 1) 0% Alginate (NO_Alg), 2) 0.5% alginate concentration without alginate crosslinking (NO_Ret), 3) 0.5% alginate concentration and alginate crosslinking after gel washing (Swell_Ret), 4) 0.5% alginate concentration and alginate crosslinking before gel washing (Ret_Swell). In all systems, PVP underwent crosslinking before alginate crosslinking.

Indeed, a considerable T_{2m} decrease occurs when alginate is crosslinked, this suggesting a mesh size reduction. It can be supposed that this apparent

disagreement between rheology and LF-NMR is due to the presence of different but coexistent chain structures constituting the three-dimensional gel polymeric network. The presence of two relaxation time for the gels containing crosslinked alginate (see Table 3.2-9) demonstrates the coexistence of highly and poorly crosslinked regions inside the network.

Table 3.2-9 Average water relaxation time (T_{2m}), and relaxation spectra (T_{2i}, A_i) referring to 20%PVP cpncentration crosslinked at 22, 33 and 44 min, plus 0% Alginate (NO_Alg), 0.5% alginate concentration without alginate crosslinking (NO_Ret), 0.5% alginate concentration and alginate crosslinking after gel washing (Swell_Ret), 0.5% alginate concentration and alginate crosslinking before gel washing (Ret_Swell).

20%PVPplus	**UV time (min)**	T_{2m}	T_{21}	A_1	T_{22}	A_2
NO_Alg	22	2256	/	/	/	/
	33	2496	/	/	/	/
	44	2299	/	/	/	/
(Alg)**NO_Ret**	22	2329	/	/	/	/
	33	2613	/	/	/	/
	44	2779	/	/	/	/
(Alg)**Swell_Ret**	22	1628	/	/	/	/
	33	1741	/	/	/	/
	44	1824	1978	47	1686	53
(Alg)**Ret_Swell**	22	1450	1720	43	1246	57
	33	1448	1514	90	849	10
	44	1038				

The small rheological effect could be explained assuming that the highly crosslinked zones, made up by crosslinked alginate, do not pervade the whole system so that they do not realize a continuum. On the contrary, only the loosely crosslinked zones, made up by crosslinked PVP, do constitute a structure pervading the whole gel volume as depicted in Figure 3.52. It is possible that the formation of the highly crosslinked regions is due to the presence of PVP that does not allow a uniform and homogenous alginate crosslinking all over the gel volume

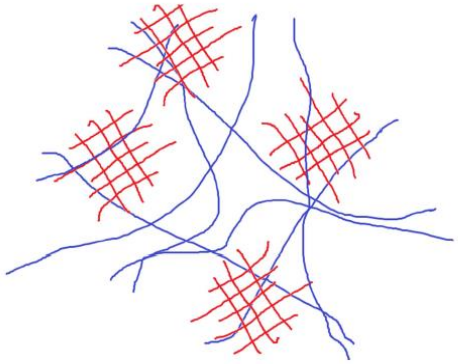

Figure 3.52 Hypothesized structure of PVP-alginate gels. Blue chains represent crosslinked PVP while red chains indicate crosslinked alginate.

The same concept can be represented in terms of average mesh size according to the rheological (ξ_{RHEO}) and LF-NMR (ξ_{NMR}) approaches. At this purpose, also for these systems, the semi-empirical approach explained in part I discussion to calculate ϕ_p and ϕ_0, was performed. This, in turn, enabled the evaluation of ξ_{RHEO} and ξ_{NMR} as shown in Figure 3.53 for the 20%PVP systems (assumed as representative of all the other PVP concentrations).

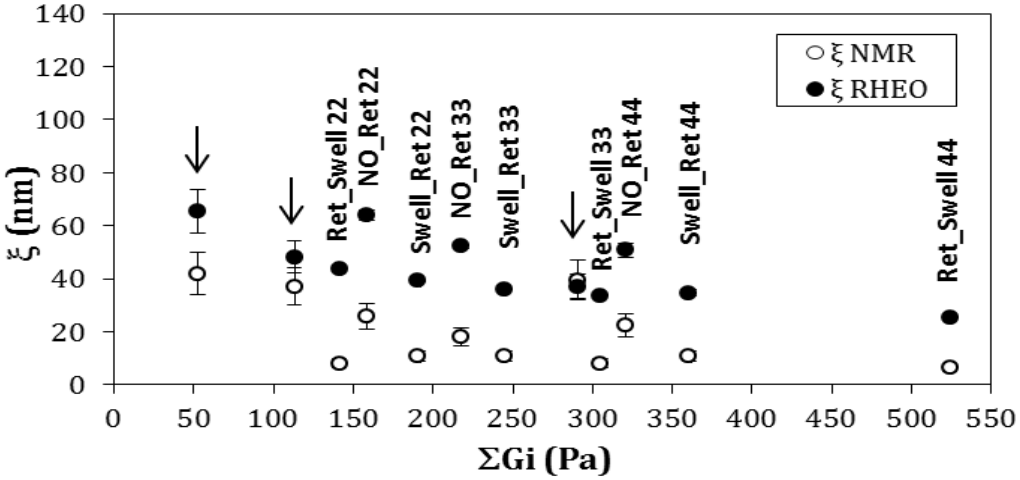

Figure 3.53 Average mesh size evaluated according to the rheology (ξ_{RHEO}) and LF-NMR approach (ξ_{NMR}) for gels 20A(22)-B(33)-C(44) No-Alg, No-Ret, Swell-Ret, Ret-Swell. Error bars represent SD (N=3). Arrows indicate systems with no alginate.

The discrepancy between rheology and NMR is reflected also in the evaluation of the average mesh size. Indeed, ξ_{NMR} is lower than ξ_{RHEO} whatever the system. The arrows indicate samples without alginate, where the concordance between rheological and NMR estimation is certainly better. The hypothesis proposed in Figure 3.52 is supported by the TEM pictures shown in Figure 3.54. These pictures

refer to systems characterized by 20% PVP *plus* 0.5% Alg exposed to UV irradiation for 33 min, washed in water for 24h, with and without alginate crosslinking (20B(Alg)_RET_Swell and 20B(Alg)_No_RET).

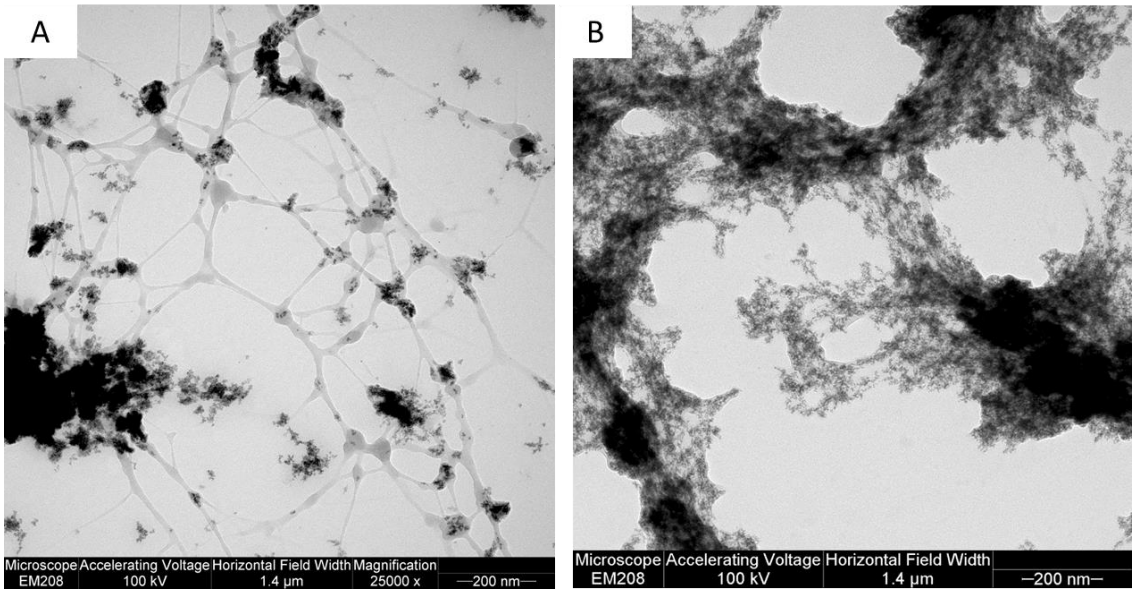

Figure 3.54 TEM image referring to 20% PVP *plus* 0.5% Alg exposed to UV irradiation for 33 min, washed in water for 24h, with **A**: (20B(Alg)_ RET_Swell) and without **B:** (20B(Alg)_NO_RET) alginate crosslinking.

Contrast agent bounds alginate chains, evidencing that when polysaccharide chains are not crosslinked, they are widely diffused in the blend (imagine B). On the contrary, the Ca^{++} effect is clearly indicated in imagine A: alginate chains drastically shrink in several isolated clusters, i.e. exactly was suggested in picture 3.52.

These findings, once more, highlight LF-NMR ability to investigate nanoscale network details that cannot emerge by the rheological analysis. It is also important to underline the essential role played by the comparison among information coming from LF-NMR and rheological approach: this dialog allows deducing structural aspects that each technique, singularly taken, could not give.

Reference

Abrami M, D'Agostino I, Milcovich G., Fiorentino S., Farra R., Asaro F., Lapasin R., Grassi G., Grassi M. "Physical characterization of alginate–Pluronic F127 gel for endoluminal NABDs delivery" *Soft Matter* 2014 (10):729–37

Bal T., Kepsutlu B., Kizilel S. "Characterization of protein release frompoly(ethylene glycol) hydrogels with crosslink density gradients". *J Biomed Mater Res A.* 2014 (102):487-95

Caldorera-Moore M., Peppas N.A. "Micro- and nanotechnologies for intelligent and responsive biomaterial-based medical systems" *Adv. Drug Deliv. Rev.* 2009 (61):1391–401

Chirra H.D., Desai T.A. "Multi-reservoir bioadhesive microdevices for independent rate-controlled delivery of multiple drugs" *Small* 2012 (8):3839–46

Chui M.M., Phillips R.J., McCarthy M.J. "Measurement of the porous microstructure of hydrogels by nuclear magnetic resonance" *J. Colloid Interface Sci.* 1995 (174):336–44

Cooley, P.; Wallace, D.; Antohe, B."Applications of Ink-Jet Printing Technology to BioMEMS and Microfluidic Systems" *J. Assoc. Lab. Autom.* 2002 (7):33–9

Cruise G.M., Scharp D.S., Hubbell J.A. "Characterization of permeability and network structure of interfacially photopolymerized poly(ethylene glycol) diacrylate hydrogels" *Biomaterials* 1998 (19): 1287–94

Fechine G.J.M., Barros J.A.G., Catalani L.H. "Poly(N-vinyl-2-pyrrolidone) hydrogel production by ultraviolet radiation: new methodologies to accelerate crosslinking" *Polymer* 2004 (45):4705–09

Fiorentino S.M., Carfì Pavia F., La Carrubba V., Brucato V., Abrami M., Farra R., Turco G., Grassi G., Grassi M. "Characterization of PLLA Scaffolds for biomedical applications" *Int. J. Polym. Mat.* 2017(in press)

Frankær S.M.G., Jensen M.K., Bejenariu A.G., Skov A.L. "Investigation of the properties of fully reacted unstoichiometric polydimethylsiloxane networks and their extracted network fractions" *Rheol. Acta* 2012 (51):559–67Fouassier J.P., Lalevée J. "Photoinitiators for Polymer Synthesis: Scope, Reactivity, and Efficiency" *Wiley-VCH* 494 pp

Hagel V., Haraszti T., Boehm H. “Diffusion and interaction in PEG-DA hydrogels” *Biointerphases* 2013 (8):1-9

Holz M., Heil S.R., Sacco A. “Temperature-dependent self-diffusion coefficients of water and six selected molecular liquids for calibration in accurate 1H NMR PFG measurements” *Phys. Chem. Chem. Phys.* 2000 (2):4740–42

Huebsch N., Arany P.R., Mao A.S., Shvartsman D., Ali O.A., Bencherif S.A., Rivera-Feliciano J. Mooney D.J.“Harnessing traction-mediated manipulation of the cell/matrix interface to control stem-cell fate” *Nat. Mater*. 2010 (9): 518–26

Ip M.S., Scott I.U., Brown G. C., Brown M. M., Ho A. C., Huang S. S., Recchia F. M. “Anti–Vascular Endothelial Growth Factor pharmacotherapy for age-related macular degeneration” *Ophthalmology* 2008 (115):1837–46

Kirchhof S., Brandl F.P., Hammer N., Goepferich A.M. “Investigation of the Diels–Alder reaction as a crosslinking mechanism for degradable poly(ethylene glycol) based hydrogels” *Mater. Chem. B* 2013 (1):4855-64

Kirchhof S., Abrami M., Messmann V., Hammer N., Goepferich A.M., Grassi M., Brandl F.P. “Diels–Alder hydrogels for controlled antibody release: correlation between mesh size and release rate” *Mol. Pharmaceutics* 2015 (12):3358–68

Khattak S.F., Chin K.S., Bhatia S.R., Roberts S.C. “Enhancing oxygen tension and cellular function in alginate cell encapsulation devices through the use of perfluorocarbons” *Biotechnol. Bioeng*. 2007 (96):156-66

Kloxin A.M., Kloxin C.J., Bowman C.N., Anseth K.S. “Mechanical properties of cellularly responsive hydrogels and their experimental determination” *Adv. Mater* 2010 (22):3484–94

Kopeček J. “Hydrogel biomaterials: A smart future?” *Biomaterials,* 2007 (28): 5185–92

Kopecek J. “Hydrogels: from soft contact lenses and implants to self-assembled nanomaterials” *J Polym Sci Part A* 2009 (47): 5929-46

Kratky O., Porod G. “Röntgenuntersuchung gelöster Fadenmoleküle” *Rec. Trav. Chim. Pays-Bas.-J. R. Netherlands Chem. Soc.* 1949 (68):1106–123

Lee H., Kim J, Park J., Rhee S., Park Y., Park C, Park E. “Controlled-release oral dosage forms containing nimodipine solid dispersion and hydrophilic carriers” *J. Drug Del. Sci. Tech.* 2017 (13):28-37

Lopérgolo L.C., Lugão A.B., Catalani L.H. "Direct UV photocrosslinking of poly(N-vinyl-2-pyrrolidone) (PVP) to produce hydrogels" *Polymer* 2003 (44):6217–22

Lutolf M.P., Hubbell J.A. "Synthesis and physicochemical characterization of end-linked poly(ethylene glycol)-co-peptide hydrogels formed by Michael-type addition" *Biomacromolecules*.2003 (4):713–22

Mahabadi H.K., Rudin A. "Effect of solvent on concentration dependence of hydrodynamic volumes and GPC elution volumes" *Polym. J.* 1979 (11):123–31

Marizza P., Keller S.S., Boisen A. "Inkjet printing as a technique for filling of micro-wells with biocompatible polymers" *Microelectron. Eng.* 2013 (111):391–5

Marizza P., Keller S.S., Müllertz A., Boisen A. "Polymer-filled microcontainers for oral delivery loaded using supercritical impregnation" *J Control. Rel*. 2014 (173):1–9

Marizza P., Abrami M. Keller S.S., Posocco P., Laurini E., Goswami K, Skov A.L. Boisen A, Laorbina D., grassi G., Grassi M. "Synthesis and characterization of uv photocrosslinkable hydrogels with poly(n-vinyl-2-pyrrolidone): determination of the network mesh size distribution" *Int. J. Polym. Mater. Biomat.* 2016 (65):516-25

Matricardi P., Di Meo C., Coviello T., Hennink W.E., Alhaique F. "Interpenetrating Polymer Networks polysaccharide hydrogels for drug delivery and tissue engineering." *Adv Drug Deliv Rev.* 2013 (65):1172-87

Momot K.I. and Kuchel P.W. "PFG NMR diffusion experiments for complex systems" *Concepts Magn. Reson.* 2006 (28A): 249–69

Sampat K.M., Garg S.J. "Complications of intravitreal injections" *Cur. Opin. Ophthalmol.* 2010

Scherer G.W. "Hydraulic radius and mesh size of gels" *J. SolGel Sci. Technol.*, 1994 (1):285-91

Stait-Gardner T., Willis S.A., Yadav N.N, Zheng G., Price W.S "NMR diffusion measurements of complex systems" in diffusion fundamentals III *Leipzig University Press*. (2009):183-204

The CATT Research Group. "Ranibizumab and Bevacizumab for Neovascular Age-Related Macular Degeneration" *N. Engl. J. Med.* 2011 (364):1897–908

Theodorou D.N., Suter U.W. "Detailed molecular structure of a vinyl polymer glass" *Macromolecules* 1985 (18):1467-78

Williams C.G., Malik A.N., Kim T.K, Manson P.N., Elisseeff J. H. "Variable cytocompatibility of six cell lines with photoinitiators used for polymerizing hydrogels and cell encapsulation" *Biomaterials* 2005 (26):1211–18

Wilson C.G., O'Mahony B., Lindsay B. "Physiological factors affecting oral drug delivery" Encyclopedia of Pharmaceutical Technology Third ed. *Marcel Dekker, J. Swarbrick (Eds.)* 2013:2866–74

Zhang X., Yang D., Nie J. "Chitosan/polyethylene glycol diacrylate films as potential wound dressing material" *Int J Biol Macromol* 2008 (43):456–62

4 Biomedical approach of LF-NMR

This last chapter is dedicated to the application of Low Field Nuclear Magnetic Resonance (LF-NMR) as a diagnostic tool in two different clinical disorders: cystic fibrosis and osteoporosis. Despite their considerable difference, these two pathological conditions share, from the LF-NMR point of view one common characteristic. Indeed, in both cases, the water hydrogens relaxation is strictly connected to disease severity.

The first chapter part is focused on Cystic Fibrosis (CF), a lung disease where a defective chloride secretion results in depletion of the airway liquid and mucus layer. This alteration leads to poorly hydrate and hyper-concentrated mucus that impairs muco-ciliary clearance, favouring the pathological invasion of microorganisms (Tildy and Ducan, 2015). I supposed that these features of CF mucus (hyper-concentration and dehydration) could affect the mean relaxation time (T_{2m}) of water hydrogens so that healthy volunteers could be discriminated from patients.

The second chapter part concerns a completely different and more diffuse pathological condition: osteoporosis. Osteoporosis is a common degenerative bone disease which is characterized by a decreased bone strength and increased risk of fracture (Yang and Duan, 2016). Although human bone is porous in nature, in the case of osteoporotic bone, these cavities are much larger and this implies bone strength decrease and femoral fracture risk increase (Rajapakse et al., 2015). I decided to take advantage of the broad and detailed literature about LF-NMR applications in rigid porous system, with the aim to detect porosity alterations through T_{2m} measurements referring to osteoarthritis and osteoporotic bones (obtained from the surgical replacement of human damaged hip joint). In order to understand the efficacy of LF-NMR, μ-CT analysis was used to confirm LF-NMR results.

4.1 The use of LF-NMR for monitoring pulmonary infections in patients affected by cystic fibrosis

4.1.1 Introduction

Cystic fibrosis is a lung disease caused by a severe functional deficiency of the cystic fibrosis trans-membrane conductance regulator (CFTR) protein (Riordan et al., 1989). CFTR is largely expressed in the apical membranes of epithelial cells, which line the cylindrical structures of secreting tissue often rich in mucus and protein. The airways are among the tissues with the highest expression of CFTR. The lack of functional CFTR causes deficient cAMP-dependent chloride and bicarbonate secretion into airway secretions. This defective secretion dehydrates apical mucus layer and prevents mucus strands release from glands, leading to mucus tethering (Figure 4.1) (Cantin et al., 2015).

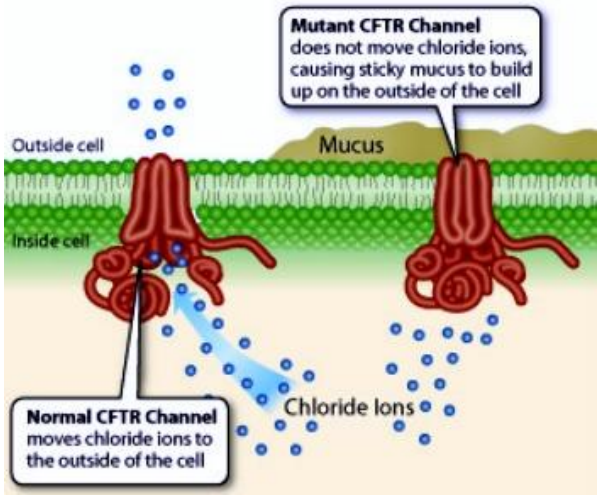

Figure 4.1 Schematic representation of cystic fibrosis cause: the deficiency of CFTR channel protein gives origin to very viscous mucus (Cystic Fibrosis Infographic: https://magic.piktochart.com/output/18485140-cystic-fibrosis)

Mucus dehydration is also favoured by the disequilibrium in the different components such as proteins, alginates, white blood cells, DNA, bacteria and mucin (Zach et al., 1996). This dehydrated and hyper-concentrated mucus impairs muco-ciliary clearance (MCC) (Tildy and Ducan, 2015). MCC system represents the critical task of clearing inhaled pathogens and toxic materials from the lung (Ghosh at al., 2015; Frizzel, 1998). This, in turn, favours chronic retention of pathogens

(overall *Pseudomonas aeruginosa*) (McCaslin et al., 2014), systemic inflammation, tissue destruction and respiratory insufficiency (Boucher, 2007).

There has been a longstanding observation that the amount of the components and dehydration state, in mucus, rises with the increase of pulmonary severity (Hill et al., 2014). Thus, the determination of water molecules condition in mucus can significantly help clinicians in monitoring the lung disease and planning therapy. Nowadays, forced expiratory volume in the first second (FEV_1) and blood test on C-reactive protein (*CRP*) are two methods extensively used to monitor the diseased lung and guide the therapy (Cystic Fibrosis Fundation, 2012). *CRP* is a plasma protein that participates in the systemic response to inflammation. Its plasma concentration increases during inflammatory states (Black and al., 2004). However, measurements obtained both by FEV_1 and *CRP* are highly technique and effort-dependent and often patients find the test uncomfortable (Davis and Alton, 2009). The direct analysis of the sputum has been considered to evaluate the pro-inflammatory cytokines, whose levels in some cases correlate with pulmonary severity, as evaluated by FEV_1 (Davis and Alton, 2009). However, standardization of the method is required before this approach can be routinely used in the clinical context. Thus, the necessity of an experimentally easy and reliable technique for monitoring mucus components in the diseased lung arises.

A recent substitute of the above traditional monitoring techniques is based on the evaluation of the rheological properties of sputum, in relation to FEV_1 (Hill et al., 2014, Tomaiuolo et al., 2014, Dumas et al. 2007). Notably, so far, sputum (obtained by expectoration) is the preferred specimen from those subjects who are capable of expectorating (Hoppe et al., 2015). The increased amount of proteins, alginates, white blood cells, DNA, bacteria and mucin (Fung et al. 2010, Zach 1996), favours the formation of a three dimensional network which alters the viscoelastic properties of the sputum (Sanders et al., 2001) that can be determined by rheological tests. Unfortunately, however, the rheological investigation requires high qualification to perform and interpret the experimental measurements. Moreover, there is the problem of sputum sampling. Indeed, the inhomogeneous nature of sputum makes the sampling procedure not straightforward and the risk of considering a non-representative sample is high.

To overcome the limitations of the above methods, I proposed the use LF-NMR for the evaluation of the sputum. LF-NMR is a non-destructive, non-invasive and low-cost approach requiring only minimal or no sample preparation (Chui et al. 1995).
I hypothesized that it could be possible to evaluate the presence and the amount of pathologic components of the sputum measuring the average water hydrogens relaxation time T_{2m} by LF-NMR. Indeed, I thought that the presence of the different pathological components in sputum could affect the relaxation time T_{2m}. My data, obtained in artificial samples (mucin solutions), in conditional sputum (healthy volunteers saliva, added by different amounts of the pathological components) and in sputum from patients, indicate that LF-NMR can reliably detect sputum components in a dose dependent fashion. As my approach is less expensive, faster, does not cause discomfort to the patients and does not require highly qualified personnel, has the potential to become a valuable monitoring tool for infective chronic pulmonary diseases.

4.1.2 Materials

Artificial samples:
Mucin (Bovine type III, SIGMA-Aldrich) was dissolved in sterile ddH_2O at 8 mg/ml, samples were filtered through 0,45 μm filters. Alginate samples were collected from a mucoid P. aeruginosa strain, grown on mannitol plates for 3-5 days.
Conditional sputum:
The conditional sputum was realised to understand the potential effect of different components commonly found in the sputum of patients affected by CF and COPD(chronic obstructive pulmonary disease). Thus, by means of gently mixing, human healthy saliva was loaded by:
i) sodium alginate (FMC Biopolymer Ltd, UK) at different concentrations (0.2 – 2.5 mg/ml) representing the typical concentrations occurring in the presence of some mucoid bacteria such as *P.aeruginosa* (Frizzel, 1988)
ii) DNA (calf thymus DNA, Sigma), in the typical concentration range 3 to 14 mg/ml (Broughton-Head, 2007)

iii) albumin (Sigma), in the typical concentration range 5 to 10 mg/ml (Sanders et al., 2001)

iv) mucin (SIGMA), in the typical concentration range 10 to 50 mg/ml (Broughton-Head et al. 2007).

As the relaxation time of healthy human saliva can present some minor variations among subjects, the average relaxation time of the systems resulting from the addition of each component (Alginate, DNA, albumin, mucin) was normalised by the relaxation time of the human saliva used (T_{2mN}).

In the attempt of reproducing a conditional sputum as close as possible to a real sputum of diseased subjects, the following mixture of components were realised: mucin (25 mg/ml), albumin (10 mg/ml), alginate (2,5 mg/ml) and DNA (14 mg/ml) (Sanders et al., 2001; Broughton-Head et al., 2007). Each measurement was performed in triplicate.

Patients

Human saliva was collected from eight adult healthy volunteers and the relaxation behaviour was immediately measured (T_{2m} = (3213 ± 200) ms). Sputum samples from adult diseased subjects were provided by Ospedale Burlo Garofalo – Centro regionale fibrosi cistica, and Ospedale di Cattinara – Pulmonology division, following a procedure approved by the Ethics Committee of the Ospedale Burlo Garofalo, (prot n. 496/2916, CI M-11, 22-3-2016). Written informed consent was obtained by each patient. Sputum samples, collected in sterile containers, were obtained by voluntary expectoration during a routine clinical visit from different patients affected by pulmonary obstruction diseases (CF, 30 patients; COPD, one patient; asthma, one patient). Sputum freezing or homogenization was not performed to avoid sample structure alteration. The determination of T_{2m} was performed just after sputum sampling. Each measurement was performed in triplicate.

4.1.3 Results and discussion

For a preliminary evaluation of the LF-NMR skill to reveal pathological components of sputum, we used artificial samples constituted by mucin that is the major component of mucus. In particular, two samples containing bovine mucin

0.8% non-filtered or filtered were tested. By filtration, I partially disrupted mucin oligomerization and reduced mucin concentration as assessed by the reduced viscoelasticity and turbidity of the resulting solution. As an additional component of CF mucus, whose presence correlates with chronic bacterial infection and worsening of the lung disease, we analysed alginate samples collected from a mucoid P. aeruginosa strain. Figure 4.2 clearly shows that the average relaxation time, T_{2m}, referring to the three artificial samples are always lower than the T_{2m} corresponding to pure water at the same temperature (37°C). Moreover, T_{2m} decreases from filtered mucin, to non-filtered mucin and to bacterial alginate. Thus, T_{2m} decreases as mucin concentration increases in the analysed samples.

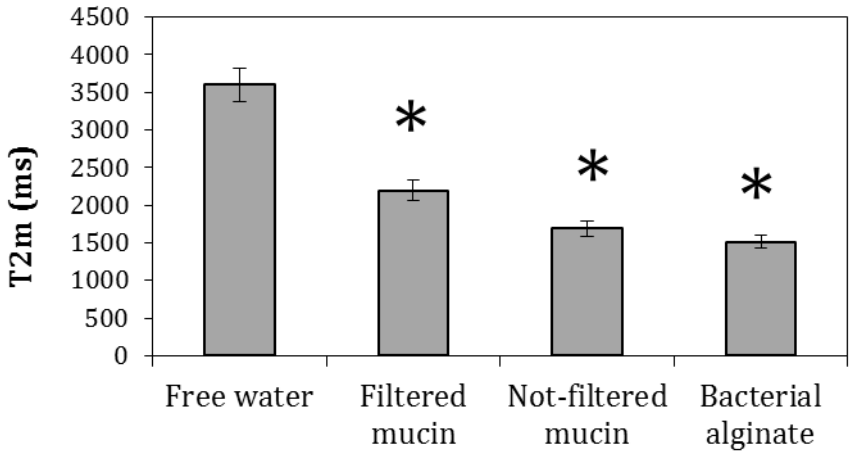

Figure 4.2 Average relaxation time T_{2m} (37°C) relative to free water, two different mucin containing systems (filtered mucin and not filtered mucin) and alginate from *P.aeruginosa*. The results are expressed as means ± S.D. of three independent quantifications. *P < 0.05 compared to relaxation time of free water.

Additionally, alginate behaves similarly showing a T_{2m} comparable to non-filtered mucin and significantly reduced respect to water. This behaviour can be easily explained in the light of the classical LF-NMR theory about solutions and hydrogels (Chui et al., 1995). Indeed, the rise of the solid component implies an increase of the interface, per unit volume, among water molecules and the solid components. As the effect of this interface is to reduce the relaxation time of the hydrogens belonging to water molecules close to the polymeric chains, the increase of mucin concentration, on average, determines the reduction of T_{2m}. In addition, LF-NMR provides further insight about the three dimensional organisation of the polymeric chains of the studied systems. While the two artificial systems (filtered and not

filtered mucin solution) are characterised by only one relaxation time, T_{21}, that coincides with the average one, T_{2m}, this does not hold true for the fourth system (alginate). In this last case T_{2m} is the weighted average of two relaxation times: $A_1\%$ = 72 ± 5, T_{21} = (1630 ± 15) ms, $A_2\%$ = 28 ± 5, T_{22} = (1227 ± 42) ms. As reported in precedent chapters, the presence of two or more relaxation times is typical of gel systems where the realisation of a three-dimensional polymeric network, stabilised by inter-chains bonds (crosslinks), takes place. According to Scherer (Scherer 1994), these relaxation times can be directly associated to the existence of two or more classes of network meshes differing for their size. Thus, not only T_{2m} assumes an important role in system characterisation, but the relaxation times distribution ($A_{i\%}$, T_{2i}) can be also considered a sort of identity card of the micro/nano structure of the system. As, in general, the spatial organisation and the kind of the polymeric chains depend on the specific bacterium which produced them (typically to form a protective shield), hence it is reasonable to surmise that the relaxation time distribution ($A_i\%$, T_{2i}) might have the potential to be used for the identification of specific bacterial strains present in the sputum of patients affected by infective lung diseases. In addition, the presence of more than one relaxation time, indicating the existence of a more complex and articulated micro/nano structure, could predicts variations in the lung microbiota which may require different therapeutic strategies. Further investigations are necessary to fully elucidating this aspect (work in progress).

The promising results, above reported, prompted me to test LF-NMR in more representative samples. For this purpose, I used conditional sputum prepared by adding to the saliva of healthy subjects, increasing amounts of alginates (typically produced by *P. aeruginosa)*, proteins, DNA, and mucin, all falling within the appropriate concentration ranges (Broughton-Head et al., 2007). Indeed, not only alginate overproduction is strictly correlated to mucoid pathogens but, in obstructive lung disease, an abnormal concentration of high molecular weight components, such DNA and albumin (Dawson et al., 2003; Vasconcellos et al.,1994) can be found. Moreover, also in the absence of infection, CF mucus contains high amounts of DNA, mucin, albumin, phospholipids, and inflammatory product (Sanders et al., 2001). Figure 4.3 clearly shows that the increase in alginate

concentration determines a monotonic reduction of the normalised average relaxation time T_{2mN}.

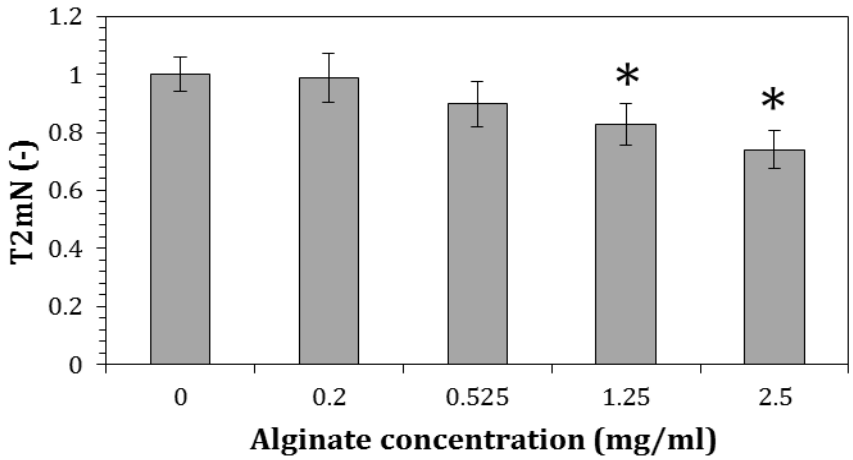

Figure 4.3 Normalized relaxation time T_{2mN} (37°C) relative to human healthy saliva containing increasing alginate concentration. The results are expressed as means ± S.D. of three independent quantifications. *P < 0.05 compared to relaxation time of human healthy saliva for alginate concentration > 0.525 mg/ml.

Table 4.1-1 Relaxation time distribution referring to the addition of alginate, at different concentrations (C), to healthy volunteer saliva. T_{2i} and $A_{i\%}$ indicate, respectively, the ith relaxation time and its % abundance.

***C*(mg/ml)**	**0.2**	**0.525**	**1.25**	**2.5**
$A_{1\%}$**(-)**	100	100	93 ± 5.56	84 ± 5.07
T_{21}**(ms)**	3175 ± 190	2886 ± 173	2787 ± 167	2686 ± 43
$A_{2\%}$**(-)**	-	-	7 ± 0.43	16 ± 1
T_{22}**(ms)**	-	-	977 ± 58	710 ± 16

The inspection of the relaxation time distribution ($A_{i\%}$, T_{2i}) reveals interesting aspects of the spatial organisation of the alginate chains. Indeed, Table 4.1-1 shows that the increase of alginate concentration leads to the appearance of a second relaxation time whose % abundance increases with alginate concentration. Again, the explanation of this behaviour relies on the classical LF-NMR theory about solutions and hydrogels (Chiu and Philips, 1995; Marizza et al., 2016). Indeed, the appearance of the second relaxation time (T_{22}) is reasonably due to an inhomogeneous distribution of polymeric chains that gives origin to clustered regions ($A_{2\%}$, T_{22}) embedded in a homogeneous, less concentrated, continuous

phase ($A_{1\%}$, T_{21}). Inside clustered regions, the higher alginate chains concentration improves the interface of the water-solid phase (alginate chains) responsible for the decrease of the hydrogens relaxation time. Relaying on my data, it descends that the increase of alginate concentration determines the increase of the clustered regions volume ($A_{2\%}$ increases) at the expense of that of the continuous, less concentrated phase ($A_{1\%}$ decreases) (see Table 4.1-1). At the same time, the alginate concentration increase provokes the progressive rise of the polymeric chains concentration in both phases (clusters and continuous phase) as both T_{21} and T_{22} decrease with alginate concentration. Finally, the small value of the ratio T_{22}/T_{21} (about $1/3 \approx 1/4$) let me suppose that the alginate concentration difference between the two phases (clusters and continuous phase) is considerable (Marizza et al., 2016).

Figures 4.4A – C substantially confirms what seen in the case of alginate addition to human saliva obtained from healthy volunteers (conditional sputum). Indeed, the increase of DNA, mucin and albumin concentration determines the decrease of the normalised average relaxation $T_{2\mathrm{mN}}$, even if in different ways. Again, this behaviour can be explained with the increase of the water/polymeric chains interface with the increase of DNA, mucin and albumin concentration. It is worth underlying that, whatever the added component (DNA, mucin, albumin), the reduction of $T_{2\mathrm{mN}}$ can be clearly detectable also at the lowest concentration considered, thus stressing the sensibility of the LF-NMR test. Notably, the appearance of the second relaxation time with the concentration increase, does not take place for albumin while it occurs for DNA and mucin. This reflects the diverse spatial organisation of the different polymeric chains.

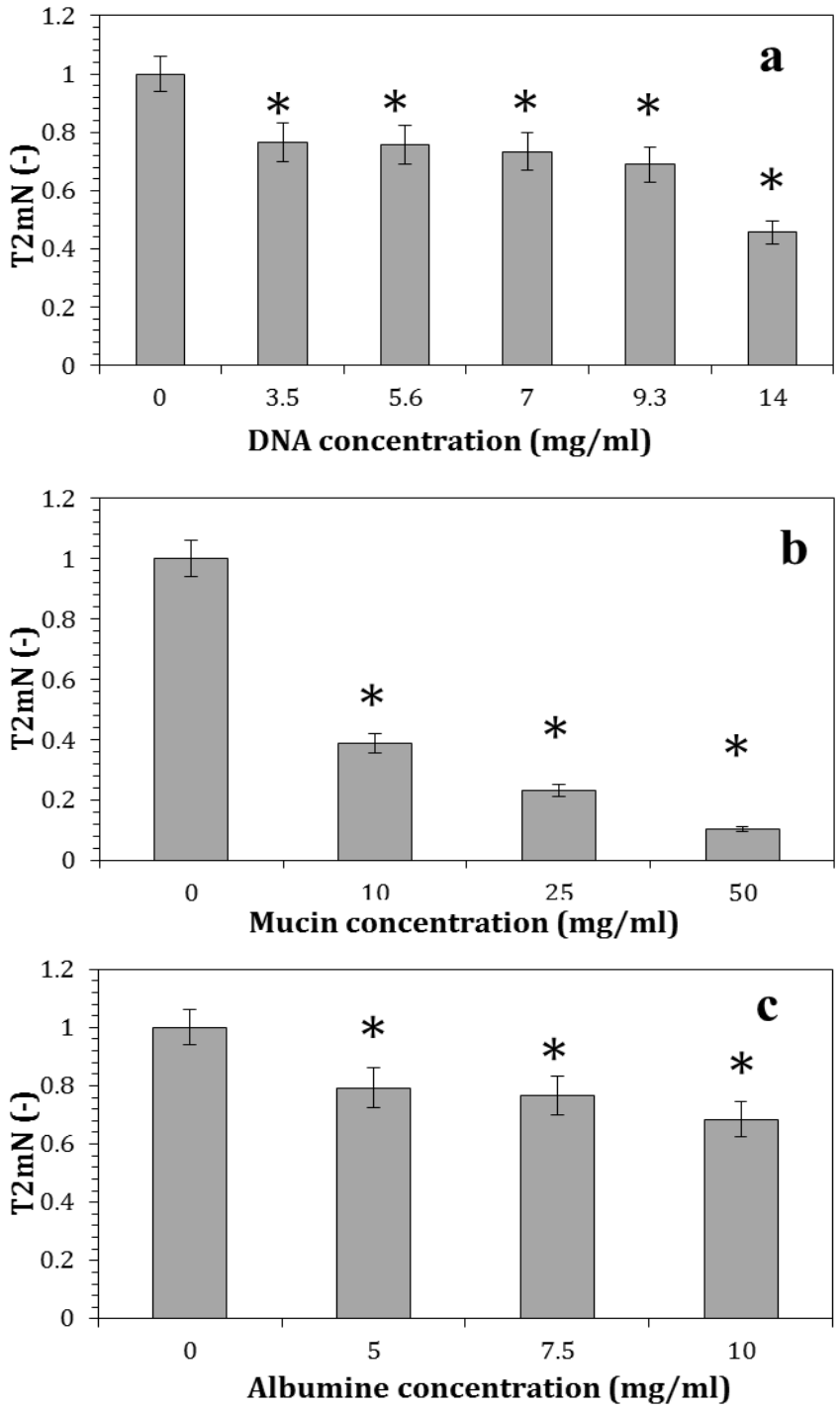

Figure 4.4 Normalized relaxation time T_{2mN} at 37°C relative to human saliva with different concentration of **A**) DNA and **B**) mucin, **C**) albumin The results are expressed as means ± S.D. of three independent quantifications. *P < 0.05 compared to relaxation time of human saliva.

Finally, Figure 4.5 shows the trend of the average relaxation time, T_{2m}, pertaining to human saliva containing mucin (25 mg/ml), mucin plus albumin (25, 10 mg/ml), mucin plus albumin plus alginate (25, 10, 2,5 mg/ml) and mucin plus

albumin plus alginate plus DNA (25, 10, 2,5, 14 mg/ml). It is clear that the progressive increase of the solid component induces the reduction of the average relaxation time. Interestingly, the conditional sputum containing all the components (mucin, albumin, alginate, DNA) resembles the sputum from CF affected patients (which often have persistent bronchopulmonary infections due to *P. aeruginosa*) in terms of T_{2m} (see sputum CF sample in Figure 4.5).

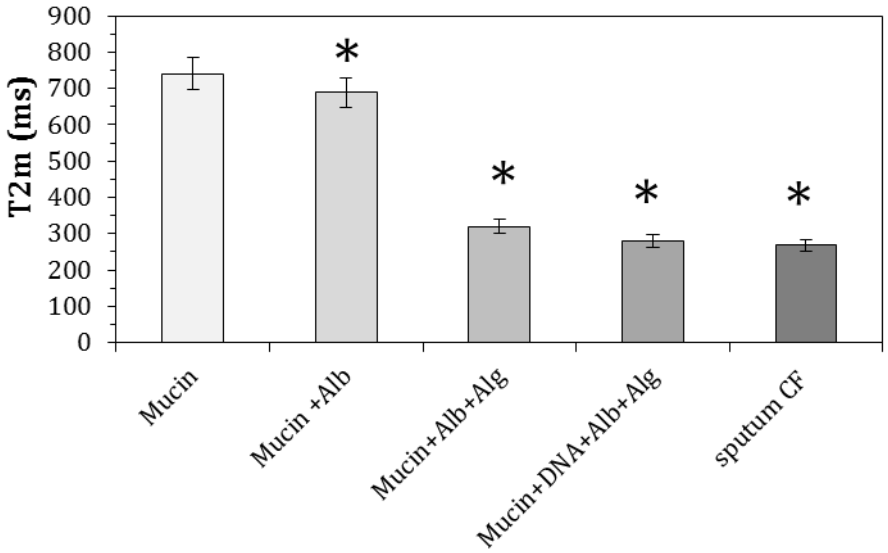

Figure 4.5 Relaxation time T_{2m} at 37°C referring to samples differing for the presence of albumin, alginate and DNA. Sputum CF indicates the T_{2m} of a patient affected by cystic fibrosis with a persistent bronchopulmonary infections due to *P. aeruginosa*. The results are expressed as means ± S.D. of three independent quantifications. *P < 0.05 compared to relaxation time of mucin alone.

However, despite similar T_{2m}, conditional and CF sputum differ for the distribution of the relaxation times. In particular, complete conditional sputum is characterised by:

$A_{1\%}$ = 83 ± 5, T_{21} = (309 ± 19) ms; $A_{2\%}$ = 17 ± 1 T_{22} = (143 ± 9) ms

while CF sputum is characterised by:

$A_{1\%}$ = 17 ± 1, T_{21} = (658 ± 40) ms; $A_{2\%}$ = 57 ± 3 T_{22} = (230 ± 14) ms; $A_{3\%}$ = 26 ± 2 T_{23} = (103 ± 6) ms.

This underlines the importance of the features of three-dimensional structure inside the sputum and the ability of LF-NMR in assessing it.

Interestingly, figure 4.6 shows the comparison among free water, healthy human saliva, condition sputum (mucin, albumin, alginate and DNA) and CF patient sputum. It is clear the similitude between CF sputum and conditional sputum and

the difference with free water and healthy saliva. Accordingly, this is a proof of the importance of the different components present in patients sputum.

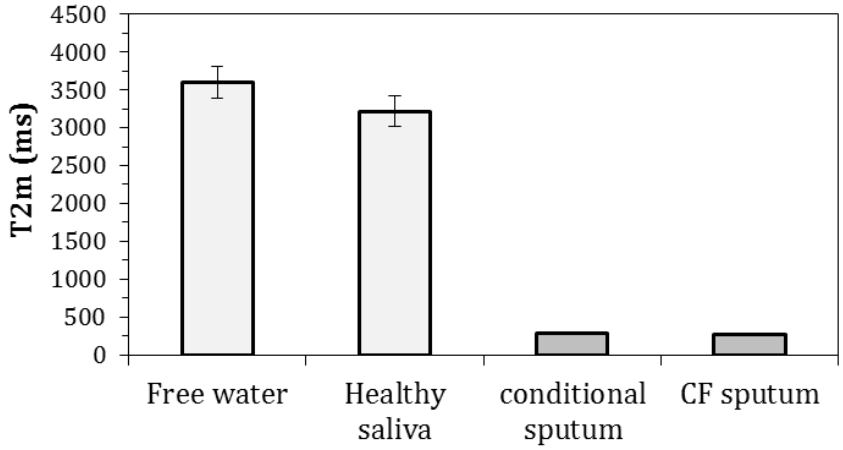

Figure 4.6 Relaxation time T_{2m} at 37°C referring to free water, healthy human saliva, condition sputum (mucin, albumin, alginate and DNA) and CF patient sputum. The results are expressed as means ± S.D. of three independent quantifications.

In order to further explore the behaviour of patient sputum, the attention was focussed on the study of the sputum obtained from patients affected by different pathological conditions (asthma, chronic obstructive pulmonary disease (COPD) and CF). The resulting T_{2m} are reported in Figure 4.7, where, for the sake of clarity, the average relaxation time measured in the saliva of healthy volunteer is reported. As expected, based on all the above reported results, T_{2m} of all the pathological conditions is clearly lower than the average of the saliva of healthy volunteers.

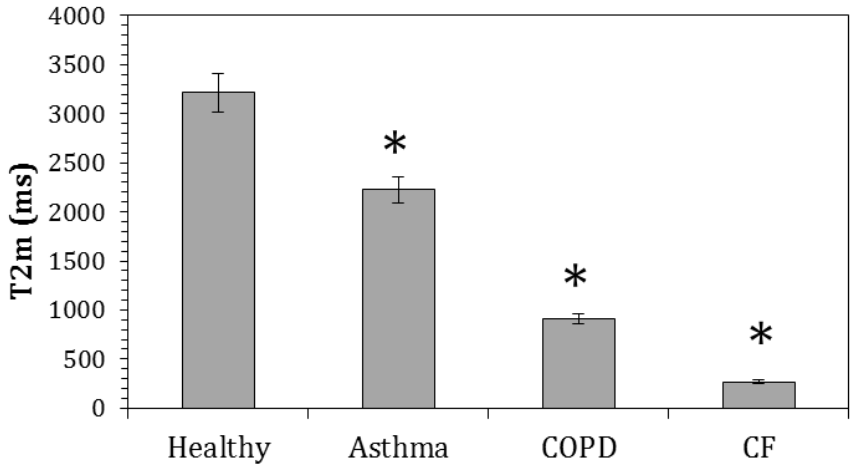

Figure 4.7 Average relaxation time (T_{2m}) referring to healthy volunteers and to patients affected by different pulmonary diseases, i.e. asthma (1 patient), COPD (1

patient) and CF (1 patient). The results are expressed as means ± S.D. of three independent quantifications. *P < 0.05 compared to relaxation time of human healthy saliva.

Table 4.1-2 Relaxation time distribution referring to healthy volunteers (8) and patients affect by asthma (1 patient), COPD (1 patient) and CF (1 patient). T_{2i} and $A_{i\%}$ indicate, respectively, the ith relaxation time and its % abundance.

	healthy	**asthma**	**COPD**	**CF**
$A_{1\%}$**(-)**	100	84 ± 5	32 ± 2	17 ± 1
T_{21}**(ms)**	3213 ± 200	2405 ± 144	1633 ± 98	658 ± 39
$A_{2\%}$**(-)**	-	16 ± 1	32 ± 2	57 ± 3
T_{22}**(ms)**	-	1257 ± 75	794 ± 48	230 ± 14
$A_{3\%}$**(-)**	-	-	36 ± 2	26 ± 2
T_{23}**(ms)**	-	-	370 ± 22	103 ± 6

Moreover, Table 4.1-2 reveals that the different clinical conditions (asthma, COPD and CF) are characterized by specific distributions of the relaxation time compared to healthy saliva. Indeed, while only one relaxation time characterizes the healthy condition, two relaxation times characterize the asthma patient and three COPD and CF patients. We believe that this is an interesting finding as COPD and CF are prone to bacterial respiratory infections, rather than asthma (Ducan and Barner 2006). As bacteria can produce polymers to protect themselves, I find reasonable the increased complexity of the three-dimensional architecture of the solid components pertaining to the sputum of COPD and CF patients. In addition, although characterized by the same number of relaxation times, COPD and CF patients differ for the values of T_{2i} and for their distribution ($A_{i\%}$), thus reflecting different three-dimensional organisation of the sputum solid part.

In order to explore the possibility to correlate T_{2m} with disease severity, I determined the average relaxation time relative to 30 patients affected by CF in relation to FEV_1 and *CRP*, two techniques commonly used to monitor the lung function. As some of the CF patients underwent monthly clinical analysis for the disease monitoring, in some cases, more than one sample was analyzed for each patient. Accordingly, I analyzed 58 samples, 58 of which of known FEV_1 and 37 of

which of known *CRP*. In addition, data referring to 10 healthy volunteers were considered. Relying on FEV_1, usually, patients can be subdivide in four classes: normal 80-120%; moderate 80-50%; severe 50-30%; very severe 30%. On the contrary, *CRP* blood level indicates presence of infections when it exceeds 0.5 mg/dl.

Figure 4.8, showing the trend of FEV_1 vs T_{2m}, evidences a clear linear correlation between these two quantities, being the correlation coefficient r = 0.738 (t(11,0.95) < 11.5).

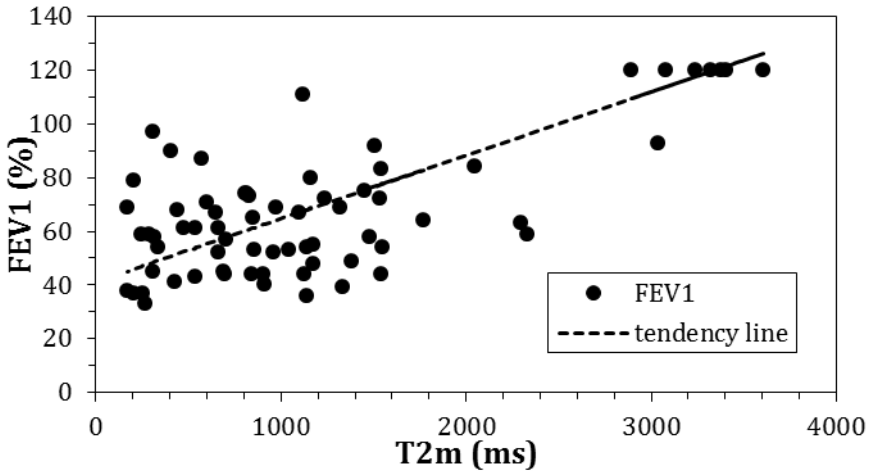

Figure 4.8 Experimental (black circles) dependence of FEV_1 vs T_{2m} relative to 57 data referring to 30 CF patients of different clinical severity and 10 data referring to healthy volunteers. The dotted line is the linear approximant (intercept = 41.15 ± 3.96; slope = (23.66 ± 2.66)*10-3 ms^{-1}).

Figure 4.9 shows that it is possible to establish a good correlation also between *CRP* and T_{2m}. Obviously in this case, the correlation slope is negative because *CRP* increases with disease severity while T_{2m} decreases with disease severity. These two parameters present a statistically significant negative correlation coefficient r= -0.382 (t(9,0.95) < 5.123).

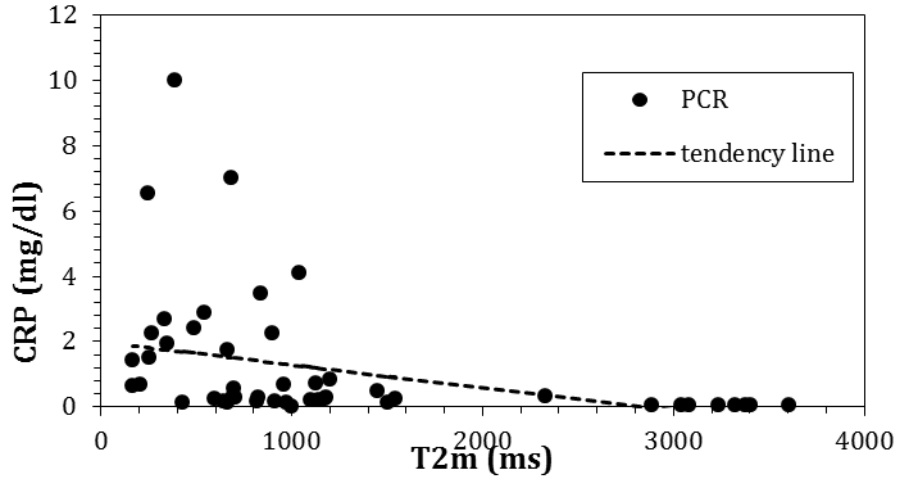

Figure 4.9 Experimental (black circles) dependence of *CRP* vs T_{2m} relative to 47 data referring to 30 CF patients of different clinical severity and 10 data referring to healthy volunteers. The dotted line is the linear approximant (intercept = 1.99 ± 0.41; slope = (-0.70 ± 0.25)*10^{-3} ms^{-1}).

Figure 4.8 and 4.9 suggest that LF-NMR analysis of sputum may become a monitoring tool for the lung condition of patient affected by cystic fibrosis. Figure 4.10 reports the T_{2m} temporal trend referring to a patient that was hospitalized three times in 462 days as indicated in the text-boxes. From Figure 4.10 clearly emerges the very good agreement between patient clinical conditions and the sputum relaxation time T_{2m}. Upon hospitalization, T_{2m} always showed very low values, while highest T_{2m} occurred upon discharge.

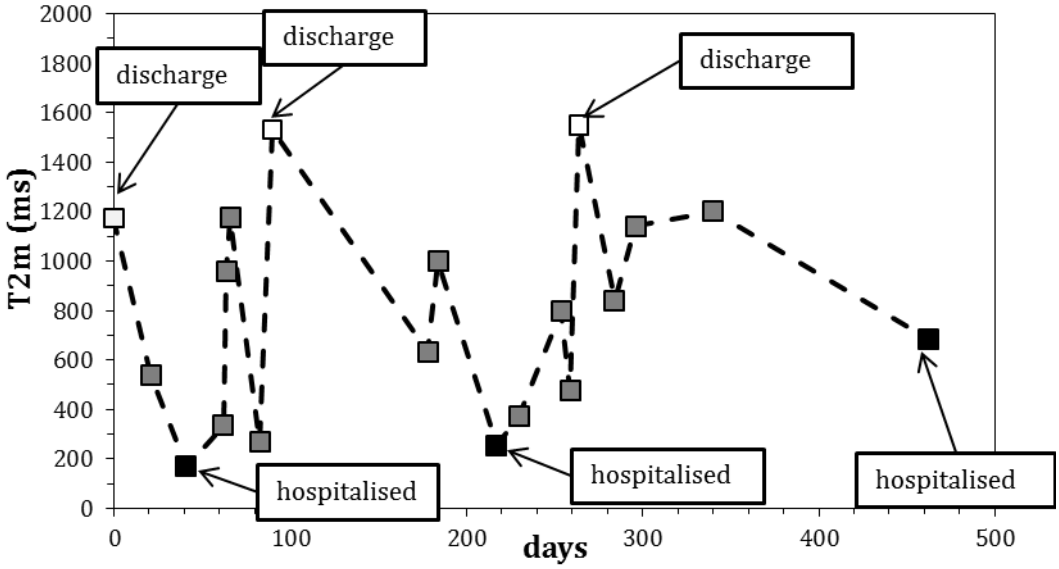

Figure 4.10 Experimental T_{2m} values relative to a single patient affected by cystic fibrosis followed for more than one year (462 days). This patient experienced different clinical conditions that required three hospitalizations and discharges.

Summarizing, my analysis indicates that using artificial samples (different mucin solutions) and conditional sputum (healthy volunteers' saliva added with typical "ingredients" found in patient sputum), the average relaxation time of the water hydrogens depends on the three-dimensional polymeric architecture present in the sputum. The reliability of my preliminary data is confirmed by the comparison between complete conditional sputum and a sample obtained from severe CF patients. In addition, the very good correlation between FEV_1 and T_{2m}, and the reasonable good correlation between CRP and T_{2m}, witnesses the reliability of T_{2m} to monitor lung conditions. These conclusions are also supported by T_{2m} data relative to a single patient followed for more than one year. Indeed, I found a continuous correspondence between T_{2m} increase/decrease and patient clinical conditions indicated by the hospitalization-discharge cycles.

Compared to other monitoring systems such as FEV_1 and CRP, this approach is less expensive, faster, does not require highly qualified personnel, it is easy to perform and it does not cause any discomfort to the patient. My data suggest that the proposed method not only has the potentiality to become a valuable monitoring tool for cystic fibrosis, but it seems also suitable for the monitoring of other obstructive pulmonary diseases like asthma and chronic obstructive pulmonary disease (COPD).

4.2 The use of LF-NMR for monitoring bone porosity increment in osteoporosis hip fracture

The strength and fracture resistance of the skeleton depend primarily on the mass, morphology/architecture, and material properties of bone tissue (Cole and Meulen, 2010). Consequently, ageing or skeletal diseases such as osteoporosis (OP) and osteoarthritis (OA) have direct influence on the mechanical properties of cortical and cancellous bone (Syahrom et al., 2015). Indeed, with the reduced physiological activity, the nutrients supply deteriorate, affecting the ability of cancellous bone to self-repair or remodel (Mulvihill and Prendergast, 2010). It is bone porosity that guarantees remodeling process and mechanical integrity of the bone (McCalden et al., 1993). In particular, the porosity of cancellous bone has two

main purposes i.e. to reduce the overall weight whilst maintaining the required strength locally, and to allow nutrients to pass through (Kameo et al., 2010). In pathological condition like OP, the disease progression is caused by a decline in bone formation activity, resulting in porosity increasing and weakening internal structure (Morita et al., 1994). Hence, the possibility to asses a bone porosity degree in OP patients could be very useful for the clinicians to understand future fracture risk and the speed of deterioration. Indeed, the quantification of micro-damages in bone has become an important tool in understanding bone behavior. The generally accepted micro-damage detection procedure is to bulk stain bone in vitro using a dye penetration technique (e.g. basic fuchsin hydrochloride) where the dye is allowed to diffuse into the bone material and binds non-specifically to open bone surfaces (Burr and Hooser, 1995). Thus, the well-defined micro-cracks are clearly detectable as regions of concentrated staining using both bright-field and epi-fluorescent optical microscopy techniques. However, these techniques are tedious and time consuming, requiring serial sectioning and microscopic examination of stained bone specimens. Furthermore, current technology does not allow the non-destructive and non-invasive detection of bone micro-damage or other measures of bone quality including micro-porosity. Most magnetic resonance imaging (MRI) techniques have been limited to the study of soft tissue or gross skeletal structure. Recently, MR images have been applied for characterization of bone marrow (Mulkern et al., 1994). On the other hand, relaxation time measurements with Low Field Nuclear Magnetic Resonance (LF NMR) have been used to determine the porosity and pore size distribution in various types of porous media. Much of the earlier work with LF-NMR was performed to measure total porosity on sandstones (Kleinberg and Vinegar, 1996). The transverse relaxation time, T_2, measurements made on water cores allowed measuring porosity and extracting T_2-distributions, which were shown to be closely related to pore size distributions (Straley et al., 1994). Despite significant differences between bone tissues and the porous media such as rocks, there are common features in the response of NMR relaxation measurements to the internal structures of the materials. Internal surface contribute to transverse relaxation of fluids in porous structure and, as repeatedly explained, the effects depend on,

among other things, local surface-to-volume ratio (S/V). Variations in local S/V can lead to distributions of relaxation times (Fantazzini et al., 2003).

Recently, this technique has been used to nondestructively determine the porosity and pore size distribution in cortical bone (Ni et al., 2007) and apparent changes in porosity and pore size distribution due to the presence of induced micro-damages (Ni and Nicolella, 2005). Hence, I would suggest LF NMR as a nondestructive and fast technique for evaluating cancellous bone porosity change when osteoporosis occurs.

This study, although far to be complete, relies on cylindrical bone samples obtained from the center of human femoral hip. For each sample, I evaluated the average water relaxation time, T_{2m}, the relaxation spectrum (A_i, T_{2i}) and the water self-diffusion coefficient, D_{H2O}. Osteoporotic and osteoarthritis bone were considered. As osteoarthritis (OA) is a degenerative disease damaging joints (typically, knees, hips, lower back and neck, small joints of the fingers and the bases of the thumb and big toe) without affecting bone porosity, OA samples were considered as control samples. On the contrary, osteoporotic bones were considered ill samples.

On the same samples, LF-NMR data were compared with μ-CT analysis, in order to enhance the bone architecture characterization.

4.2.1 Materials

Trabecular bone specimens were obtained from human hips harvested after the surgical procedure for hip replacement in Ospedale di Cattinara – Orthopedic division. Written informed consent was obtained by each patient. The removed femoral heads were washed and cylindrically shaped samples were extracted, left 48 h in bleach and sterilized in autoclave in order to remove cellular components. Totally, I received 3 samples from osteoarthritis bone (controls) and 15 from osteoporosis (cases).

4.2.2 Results and discussion

The comparison between the average OA ($T_{2avg}(OA)$ = 1076 ± 139 ms) and OP ($T_{2avg}(OP)$ = 1466 ± 263 ms) relaxation times reveals that they are statistically different as proved by the t test: t(0.95,16)<2.45. OP samples are characterized by a higher relaxation time with respect to OA samples and this could be correlated to increased porosity in OP specimens. Moreover, an inspection of the relaxation spectra (T_{2i}, A_i) referring to OP and OA samples (see Table 4.2-1) reveals that, in OP samples, the percentage of bigger pores (A_1, A_2), i.e. those connected to the highest relaxation times (T_{21}, T_{22}), represents about 74% of the whole pores volume while this percentage decreases to 52% in OA samples. In addition, it is interesting to notice that not only OP samples do not show the smallest pores (A_5) that, on the contrary, represent 10% of the whole pores volume in OA samples, but also the percentage of A_4 and A_3 pores are clearly decreased in OP samples. It seems that osteoporosis implies the disappearing of smaller pores in favour of bigger ones. This could be explained supposing that the loss of bone structure implies the destruction of the barriers delimitating the small pores so that they merge to form bigger pores.

Table 4.2-1 Average relaxation time (T_{2i}) and abundances (A_i) relative to 3 OA samples and 15 OP samples.

osteoarthritis (controls) n=3		***Osteoporosis (cases) n=15***	
T_{2i} ± SD (ms)	**Ai%(-) ± SD**	**T_{2i} ± SD (ms)**	**Ai%(-) ± SD**
T_{21} = 2535 ± 352	A_1 =26 ± 4	T_{21} = 2483 ± 372	A_1 = 42 ± 6
T_{22} =1206 ± 129	A_2 = 26 ± 2	T_{22} = 1219 ± 304	A_2 = 32 ± 8
T_{23} =376 ± 44	A_3 = 20 ± 2	T_{23} = 323 ± 113	A_3 = 16 ± 2
T_{24} =108 ± 6	A_4 = 18 ± 2	T_{24} = 72 ± 18	A_4 = 11 ± 3
T_{25} =23 ± 2	A_5 = 10 ± 2		

These evidences would induce to conclude that a weakening of bone architecture occurred in OP samples. Although this is not necessarily connected to the increase of bone porosity, it is a clear evidence of bone evolution towards a weaker structure due to pores enlargement.

These conclusions are also supported by LF-NMR measurements about the water apparent self-diffusion coefficient (D_{H2O}) inside the same samples. Test parameters for PGSE sequence were: $x_1 = x_2 = 1$ ms and $\delta = 0.5$ ms. Figure 4.11 reports the trends of averaged apparent water self-diffusion coefficient in osteoarthritis bones (D_{H2O}OA) and in osteoporosis ones (D_{H2O}OP) as a function of the square root of the time diffusion t_d. Eq.2.48 fitting (dotted lines) to the experimental data shown in Figure 4.11 reveal different values for the average pores dimension ξ: ξ(OA)=35±0.5 nm and ξ(OP)=75±1 nm. This is a further evidence of a clear difference between the microstructure of OA and OP bones. In particular, also the diffusion tests proves that the pores pervading OP bones are bigger than those appearing in OA bones.

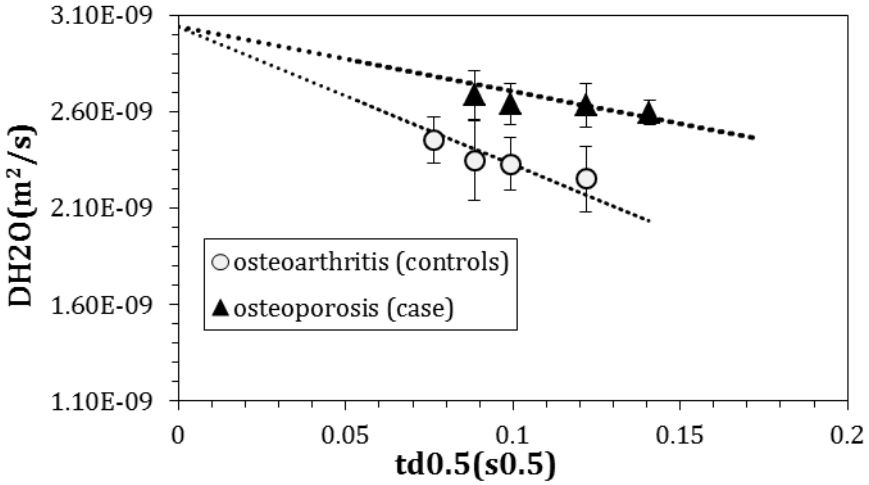

Figure 4.11 Self-diffusion coefficients of water molecules (D_{H2O}) in osteoarthritis (white circles) and osteoporosis bones (black triangles) versus the square root of the diffusion time, t_d. Dotted lines are eq.(2.42) best fitting. Bars indicate S.D. calculated from 3 and 15 independents experiments for, respectively, OA and OP samples.

The comparison between LF-NMR results and μCT ones are not perfectly in line as μCT does not evidence a clear difference between average pores size in OP and OA samples: ξ(OA)= 177 ± 38 nm and ξ(OP)= 183 ± 29 nm. This behaviour could be explained by the fact that while LF-NMR is more sensible to small pores (10-100 μm) and much less to big pores (> 300 μm), exactly the opposite takes place for μCT. In addition, the sample procedure required by μCT surely alters a little the bone structure causing, *de facto*, pores enlargement. This was proved by a simple test consisting in the LF-NMR analysis of some samples just before and just after

μCT measurements. As a matter of fact, the average relaxation time of the samples that underwent μCT was always increased whatever the sample considered (data not shown). Finally, while μCT accounts very carefully for the bone topology, LF-NMR assumes every hole as spherical, neglecting, for example, the existence of not spherical, connecting holes among pores. Accordingly, μCT can easily and precisely evaluate bone porosity, aspect that cannot be directly measured by means of LF-NMR.

In the light of these considerations, I argue that the more profitable way to use the information coming from LF-NMR and μCT is not the direct comparison, but a symbiotic merging. Indeed, μCT could be used to evaluate porosity (percentage of voids inside the bone) and LF-NMR could be used to split porosity in different classes, each one pertaining to a different relaxation time. In addition, it would be useful establishing a correlation between bone porosity and the ratio T_{2m}/T_{2H2O}. Indeed, in my feeling is that a positive correlation should exist as when porosity approaches 1, the same occurs for the T_{2m}/T_{2H2O} ratio. On the contrary, the smaller the porosity the smaller the T_{2m}/T_{2H2O} ratio. Ultimately, this is the same strategy adopted by Fantazzini (Fantazzini 2003) who evaluated bone porosity by means of volumetric and gravimetric measurements and, then, she split this information into different classes characterised by different pores diameters.

References

Black S., Kushner I., Salmos D. "C-reactive Protein" *J. Biol Chem.* 2004 (279): 48487–90

Boucher R.C. "Airway surface dehydration in cystic fibrosis: pathogenesis and therapy" *Annu. Rev. Med.* 2007 (58):157–70

Broughton-Head V.J., Smith J.R., Shur J., Shute J.K. Actin limits enhancement of nanoparticle diffusion through cystic fibrosis sputum by mucolytics. Pulm Pharmacol Ther 2007;20:708–717

Burr D.B., Hooser M. "Alterations to the en bloc basic fuchsin staining protocol for the demonstration of microdamage produced in vivo" *Bone* 1995 (17): 431–3

Cantin A., Hartl M., Konstan M.W., Chmiel J.F. "Inflammation in cystic fibrosis lung disease: Pathogenesis and therapy". *J. Cystic Fibrosis* 2015 (14):419–30

Chui M.M., Phillips R.J., McCarthy M.J. "Measurement of the porous microstructure of hydrogels by nuclear magnetic resonance" J. Colloid Interface Sci. 1995 (174):336–44

Cole J.H. and Meulen M.C.H. "Biomechanics of bone". In Adler RA, editor. *Osteoporosispathophysiology and clinical management.* Humana Press, c/o Springer Sci-ence+Business Media; 2010: 157–80

Cystic Fibrosis Foundation: Patient Registry, 2011 Annual Data Report to the Center Directors. Bethesda, Maryland, 2012 Cystic Fibrosis Foundation

Davies J.C., Alton E.W. "Monitoring respiratory disease severity in cystic fibrosis" *Respir. Care* 2009 (54):606-17

Dawson M., Wirtz D., Hanes J. "Enhanced viscoelasticity of human cystic fibrotic sputum correlates with increasing microheterogeneity in particle transport" *J. Biol. Chem.* 2003 (278):50393-401

Ducan F.R., Barner P.J. "Treatment of airway mucus hypersecretion" *Ann. Med.* 2006 (38):116-25

Dumas F.L., Marciano F.R., Oliveira L.V.F., Barja P.R., Acosta-Avalos D. "Photoacoustic monitoring of the absorption of isotonic saline solution by human mucus" *Med Eng Phys* 2007 (29):980-3

Fantazzini P., Brown R.J.S., Borgia G. C. "Bone tissue and porous media: common features and differences studied by NMR relaxation" *J. Magn. Reson. Imaging* 2003 (21):227-34

Fung C, Naughton S, Turnbull L, Tingpej P, Rose B, Arthur J. "Gene expression of Pseudomonas aeruginosa in a mucin-containing synthetic growth medium mimicking cystic fibrosis lung sputum" *J. Med. Macrobiol.* 2010 (59):1089–100

Frizzell R.A. "Role of absorptive and secretory processes in hydration of the airway surface" *Am. Rev. Respir. Dis.* 1988 (138):S3–S6

Ghosh A., Boucher R.C., Tarran R. "Airway hydration and COPD" *Cell. Mol. Life. Sci*.2015 (72):3637-52

Hill D.B, Vasquez P.A, Mellnik J., McKinley S.A., Vose A., Frank M., Henderson A.G., Donaldson S.H., Alexis N.E., Boucher R.C., Forest M.G. "A biophysical basis for mucus solids concentration as a candidate biomarker for airways disease" *PLoS ONE* 2014 (9):e87681

Hoppe JE, Towler E, Wagner BD, Accurso FJ, Sagel SD and Zemanick ET. "Sputum induction improves detection of pathogens in children with cystic fibrosis" *Pediatr. Pulmonol.* 2015 (50):638–46

Kameo Y., Adachi T., Sato N., Hojo M. "Estimation of bone permeability considering the morphology of lacuno-canalicular porosity" *J. Mech. Behav. Biomed. Mater.* 2010 (3):240–8

Kleinberg R. and Vinegar H. "NMR properties of reservoir fluids" *The Log Analyst*. 1996 (37):20-32

Marizza P., Abrami M., Keller S.S., Posocco P., Laurini E., Goswami K., Skov A.L., Boisen A., Larobina D., Grassi G., Grassi M. "Synthesis and characterization of UV photocrosslinkable hydrogels with poly(N-vinyl-2-pyrrolidone): determination of the network mesh size distribution" *Int. J. Polym. Mat. Polymer. Biomat.* 2016 (65):516–25

McCalden RW, McGeough JA, Barker MB, Court-Brown CM. "Age-related changes in the tensile properties of cortical bone. The relative importance of changes in porosity, mineralization, and microstructure" *J. Bone Joint. Surg. Am.* 1993 (8):1193-205

McCaslin C.A., Petrusca D., Poirier C., Serban K., Anderson G., Petrache I. "Impact of alginate-producing Pseudomonas aeruginosa on alveolar macrophage apoptotic cell clearance" *J. Cyst. Fibros*. 2014 (10):70-7

Morita M., Ebihara A., Itoman M. "Progression of osteoporosis in cancellous bone depending on trabecular structure" *Ann. Biomed. Eng,* (1994) (22): 532-9

Mulkern R.V., Meng J., Oshio K., Guttmann C.R., Jaramillo D. "Bone marrow characterization in the lumbar spine with inner volume spectroscopic CPMG imaging studies" *J. Magn. Res. Imag.* 1994 (4)585–9

Mulvihill B.M. and Prendergast P.J. "Mechanobiological regulation of the remodeling cycle in trabecular bone and possible biomechanical pathways for osteoporosis" *Clin. Biomech.* 2010 (25):491–8

Ni Q.W. and Nicolella D.P. "The characterization of human cortical bone microdamage by nuclear magnetic resonance" *Meas. Sci. Technol.* 2005 (16):659–68

Ni Q., Nyman J.S., Wang X., De Los Santos A., Nicolella D.P. "Assessment of water distribution changes in human cortical bone by nuclear magnetic resonance" *Meas. Sci. Technol.* 2007 (18):715–23

Rajapakse C.S., Bashoor-Zadeh M., Li C., Sun W., Wright C.A., Wehrli F.W. "Volumetric cortical bone porosity assessment with MR Imaging: validation and clinical feasibility" *Radiol.* 2015 (276):526-35

Riordan JR, Rommens JM, Kerem B, Alon N, Rozmahel R, Grzelczak Z, et al. Identification of the cystic fibrosis gene: cloning and characterization of complementary DNA [published erratum appears in Science 1989 Sep 29;245(4925):1437]. Science 1989;245:1066–73

Sanders N.K., Van Rompaey E., De Smedt S.C., Demeester J. "Structural alterations of gene complexes by cystic fibrosis sputum" *Am. J. Respir. Crit. Care Med.* 2001 (164):486–93

Sharma L. "Osteoarthritis Year in Review 2015: Clinical" *Osteoart. Cart.* 2016 (24):36–48

Scherer G.W. "Hydraulic radius and mesh size of gels" *J. SolGel Sci. Technol.*, 1994 (1):285-91

Straley C., Rossini D., Vinegar H., Tutunjian P., and Morriss C. "Core analysis by Low Field NMR" *SCA paper 9404*, International Symposium of the Society of Core Analysts, 1994, Stavanger, Norway

Syahrom A., Kadir M.R.A., Harun M.N., Öchsnerc A. “Permeability study of cancellous bone and its idealised structures” *Med. Eng. & Phys.* 2015 (37):77–86

Tildy B.E., Ducan F.R. “Therapeutic options for hydrating airway mucus in cystic fibrosis” *Pharmacology* 2015 (95):117-32

Tomaiuolo G., Rusciano G., Caserta S., Carciati A., Carnovale V., Abete P., Sasso A., Guido S. “A new method to improve the clinical evaluation of cystic fibrosis patients by mucus viscoelastic properties” *PLoS ONE* 2014 doi:10.1371/journal.pone.0082297

Vasconcellos C.A., Allen P.G., Wohl M.E., Drazen J.M., Janmey P.A., Stossel T.P. “Reduction in viscosity of cystic fibrosis sputum in vitro by gelsolin” *Science* 1994 (263):969-71

Yang S., Duan X. “Epigenetics, Bone Remodeling and Osteoporosis.” *Curr Stem Cell Res Ther* 2016 (ahead of print)

Zach MS. “The role of recombinant human DNase in the treatment of patients with cystic fibrosis: Many promises, more problems”. *Thorax* 1996 (51):750–5

5 Conclusions

Hydrogels are water-swollen polymeric materials that maintain a distinct three-dimensional structure despite the huge amount of water they can absorb. Due to their good biocompatibility, flexibility in fabrication, variable composition, and physical characteristics (similar to physiological conditions), hydrogels alone or combined with cells have many biomedical applications. They can serve as scaffolds that provide a 3D structure for tissue engineering, as carriers for cell encapsulation or drug/gene delivery, as adhesives or barriers between tissue and material surfaces. Whatever hydrogel final applications, biomaterials need a characterization of the internal structure and fiber organization. This point represents a significant challenge, because the structural characterization of high water content materials such as hydrogels is problematic due to the inherent properties of water that are dependent on conditions of temperature and pressure. This PhD thesis would propose a truly opportunity for a reliable, fast, non destructive and not expensive hydrogel characterization with the combined used of rheology and low field nuclear magnetic resonance (LF NMR). Even if rheology is already extensively used for hydrogel characterization, the integration of rheological analysis with LF NMR approach is rather innovative. I verified the reliability of this strategy on four hydrogels for biomedical applications, comparing our results with other more common characterization techniques.

Firstly, I characterized by rheology and LF-NMR a thermo-sensitive hydrogel based on chitosan/β-glycerolphosphate, focusing on the temperature effect on the kinetics of the sol-gel transition. Both techniques converged to very close results in terms of gelation temperature and mesh size estimation, this last finding being also confirmed by drug release test. Always in the field of sol-gel transition, the salt-concentration and sonication-time effects were investigated for highly-carboxilated cellulose suspensions. Rheology and NMR demonstrated to be complementary as they could point out different aspects of the hydrogel nano-

structures in reason of some formulation parameters such as salt concentration and sonication time.

More practically oriented the third and the fourth studied hydrogels were: degradable PEG functionalized hydrogel for antibodies controlled release and photocrosslinked poly(vynil pyrrolidone) (PVP) hydrogels for micro-drug delivery systems. Again, for PEG hydrogel, the two techniques led to similar mesh size, that were further confirmed by drug release test. For PVP systems, it was necessary establishing a semi-theoretical approach to perform both the rheology and LF-NMR characterization. In this case I could verify that the two approaches led to similar evaluation of the mesh size only when the shear modulus was high, this reflecting the absence of dangling chains that can be detected by LF-NMR but not by rheology as their contribute to the elastic hydrogel behavior is negligible if not absent. Interestingly, the addition of alginate to PVP solution led to hydrogels showing peculiar characteristics. Indeed, despite alginate crosslinking, the shear modulus did not increase even if the average relaxation time decreased a lot. This was due to a particular topological arrangement that was firstly theoretically supposed on the basis of the rheological and LF-NMR characterization and subsequently confirmed by TEM images.

As LF-NMR demonstrated a good skill in quickly and easily analyzing very different hydrogels, the second part of this thesis was devoted to very practical applications in medical field. At this purpose “human samples”, namely, sputum from cystic fibrosis (CF) patients and bones from osteoporotic (OP) ones, were studied. I got very promising results for CF samples as LF-NMR was able to find a correlation between experimental relaxation data and patients clinical conditions. The work on osteoporosis, although still in its infancy, allowed concluding that LF-NMR is very promising in studying bone microstructure especially in conjunction with μCT.

In conclusion, I can say that the combination of rheology and LF-NMR is a powerful tool for the structural characterization of hydrogel and biological samples. Used together, these two approaches allow obtaining structural information about systems micro- and nano- architecture that would be not otherwise determined. In addition, LF-NMR, due to its intrinsic speed and ease of use, promises to be a very

useful tool for monitoring clinical conditions in pathologies like cystic fibrosis and maybe also osteoporosis. In other words, it represents an aid to guide the everyday therapy.